جامعة سيدي محمد بن عبد الله بفاس
UNIVERSITÉ SIDI MOHAMED BEN ABDELLAH DE FES

كلية العلوم والتقنيات فاس
FACULTÉ DES SCIENCES ET TECHNIQUES DE FÈS

Centre d'Etudes Doctorales : Sciences et Techniques de l'Ingénieur

N° d'ordre 36/2021

THESE DE DOCTORAT

Présentée par

Mr: HUSSAM BOUAAMLAT

Discipline : Physique

Spécialité : Physique des Matériaux et Nanostructures

Sujet de la thèse : New Organic Materials Based on Ethylcarbazole For Optoelectronic Applications : Characterization and Computational studies.

Thèse présentée et soutenue le samedi 10 avril 2021 devant le jury composé de :

Nom Prénom	Titre	Etablissement	
Mohammed Naciri BENNANI	PES	Faculté des Sciences de Meknès	Président
Abdenbi BOUZID	PES	Faculté des Sciences de Meknès	Rapporteur
Abdelouahed ESSAHLAOUI	PES	Faculté Polydisciplinaire de Taza	Rapporteur
Abdelhai RAHMANI	PH	Faculté des Sciences de Meknès	Rapporteur
Taj-dine LAMCHARFI	PES	Faculté des Sciences et Techniques de Fès	Examinateur
Souad EL KHATTABI	PH	Ecole Nationale des Sciences Appliquées de Fès	Examinateur
Luca TORTORA	Pr	Institut National de Physique Nucléaire de Rome	Examinateur
Mohammed BOUACHRINE	PES	Ecole Supérieure de Technologie de Meknès	Co-directeur de thèse
Mustapha ABARKAN	PES	Faculté Polydisciplinaire de Taza	Directeur de thèse

Laboratoire d'accueil : Sciences de l'Ingénieure.

Etablissement : Faculté Polydisciplinaire de Taza.

To my Beloved Parents

Acknowledgements

This work was carried out within the Laboratory of Engineering Sciences, Polydisciplinary Faculty of Taza, Sidi Mohamed Ben Abdellah University of Fez, in collaboration with Department of Electrical Engineering, Faculty of Sciences and Technologies, Fes and Laboratory of Chemistry-Biology Applied to the Environment, Faculty of Sciences, Moulay-Ismail University, Meknes.

I owe my thanks to my supervisor Professor Mustapha ABARKAN for his supervision and invaluable support during my thesis. I am especially grateful to ABARKAN for encouraging me to be the best that I can and for his constant motivation with my research. My thanks also extend to my co-supervisor, Professor Mohammed BOUACHRINE, who offered me support, and advice on computational techniques.

I am very thankful to Mohammed Naciri Bennani from Moulay Ismail University, who provide us with necessary organic materials. A significant part of the work presented in my thesis was done in the Department of Electrical Engineering, Faculty of Sciences and Technologies, Fes. For that, I would like to thank Professor Farid Abdi and Professor Taj-dine Lamcharfi for welcoming me to their laboratory.

Additionally, I would like to thank Dr. Nasr Hadi from the Faculty of Sciences and Technologies, Fes, for exciting discussions and advice on Dielectric and Electric Properties. I am grateful to Professor Alex BROWN from Alberta University, Canada, for his valuable and considered information on some of my articles. I thank Ms Sabina PISTONE for her effort in proofreading my thesis.

I want to thank Professor Luca TORTORA for welcoming me to his Lab during my stay in Italy at the National Institute of Nuclear Physics, Rome, and for his help in the projects conducted there. Also, not forgetting Professor Paolo BRANCHINI and Antonio BUDANO for their help concerning the tools needed to accomplish the work.

I am grateful to Associate Professor Ouafae NINIS for her help during the early stages of my Ph.D. Many thanks to Dr. Tayeb ABRAHM for great scientific discussions and ideas.

Finally, I would like to express my great gratitude to my parents and brothers that this thesis would not have existed without their financial and moral support.

Abstract

Organic electronics is a rapidly expanding field that has recently developed around organic materials based on *pi*-conjugated molecules. In this context, the thesis covers theoretical and experimental approaches to deal with such materials for optoelectronic applications. This work represents an effort to understand the key parameters that can improve their performance. A study was applied on Polypyrrole based material to examine the effect of the elongation of the 3,3'-dioctylterpyrrole (DOTP) and 3,3'-dihexylquaterpyrrole (DH4P) on the geometric, electronic, and absorption properties, as well as the influence of alkyl chain in 3,3'- dihexylquaterpyrrole (DH4P) and 3-3,7– dimethyldienyloctyl-3'dodecylquaterpyrrole (ddoD4P). Next, seven dye sensitizers based on Selenophene as a p-spacer, besides multiple electron-donating groups, were used with 2-cyanoacrylic as an electron acceptor unit forming D-*pi*-A structure. We discussed structural and electronic properties alongside the dependency of the photovoltaic parameters (open-circuit voltage (V_{oc}), oxidation potential energy, and electron injection force), in order to find the potential sensitizers for DSSCs applications. Thus, Density Functional Theory (DFT) and Time-Dependent DFT (TDDFT) were carried out with many functionals and basis sets. This was a practical confirmation of the use of DFT for our proposed new materials. For the new Ethylcarbazole-based materials, the same theoretical procedures mentioned above were adopted. Regarding the experimental part, characterization measurements involved different techniques such as X-ray diffraction, scanning electron microscopy, and UV-Vis was used to gain insight into the structure of the materials. Then, the dielectric and electrical properties have been studied over the frequency range from 1 kHz to 2 MHz and the temperature range from 30 °C to 120 °C to explore the effect of changing the polymer blocks in our material.

Table of contents

List of figures **xiii**

List of tables **xvii**

Acronyms **xix**

General Introduction **1**

1 Background Literature **5**

1.1 Semi-conductor 5

1.1.1 Inorganic Semi-conductor 6

1.1.2 Organic Semi-conductor 8

1.1.3 The Different Types of Organic Semiconductor materials 8

1.1.4 Conjugated Polymers 9

1.1.5 History and Progress of π-conjugated Polymers 10

1.1.5.1 Historical Context 10

1.1.5.2 Progress of π-conjugated Polymers 11

1.1.6 Structure of Conjugated Polymers 12

1.1.7 Energy Levels of Conjugated Polymers 13

1.1.8 Charge Transport in Conjugated Polymers 14

1.2 Application of π-conjugated polymers 15

1.2.1 Light Emitting Diodes (OLEDs) 15

1.2.2 Organic Field Effect Transistors 16

1.2.3 Sensors 19

1.2.4 Storage Applications 21

1.2.5 Organic Photovoltaic Cells 22

1.3 Conclusion 27

2 Materials and Methods **29**
2.1 Materials . . . 29
2.1.1 Structure of The Studied Materials . . . 29
2.1.2 Synthesis of Conjugated Polymers . . . 31
2.2 Methods . . . 32
2.2.1 Theoretical Principles of Modeling . . . 32
2.2.1.1 Hartree-Fock Approximation . . . 33
2.2.1.2 Density Function Theory (DFT) . . . 35
2.2.1.3 Thomas and Fermi Model . . . 36
2.2.1.4 Hohenberg-Kohn Theorem . . . 36
2.2.1.5 The Kohn-Sham Equations . . . 38
2.2.1.6 Exchange-Correlation Functionals . . . 40
2.2.1.7 Basis Sets . . . 42
2.2.2 Experimental Methods . . . 43
2.2.2.1 X-Ray Diffraction . . . 43
2.2.2.2 Absorption Spectroscopy . . . 46
2.2.2.3 Scanning Electron Microscopy . . . 49
2.2.2.4 Complex Impedance Spectroscopy . . . 51
2.3 Conclusion . . . 60

3 Theoretical Study of Organic Materials **61**
3.1 Alkyl-Substituted Oligopyrroles . . . 61
3.1.1 Computational Details . . . 61
3.1.2 Geometric Parameters . . . 62
3.1.3 Electronic Proprieties . . . 63
3.1.4 Absorption Parameters . . . 65
3.2 Organic Dyes Based On Selenophene For Efficient Dye-sensitized Solar Cell . . . 66
3.2.1 Parameter Estimation Equations . . . 66
3.2.2 Computational Details . . . 68
3.2.3 The Choice of The XC Functional . . . 69
3.2.4 Geometry Structures . . . 70
3.2.5 Molecular Orbitals . . . 72
3.2.6 Photovoltaic Properties . . . 75
3.2.7 Ionization Potential and Electron Affinity . . . 76
3.2.8 Reorganization Energies . . . 77
3.2.9 Absorption . . . 78

3.3 Electronic and Optical Properties of Ethylcarbazole Based Materials . . 80
3.3.1 Computational Details 80
3.3.2 Optimized Geometries 80
3.3.3 Frontier Molecular Orbital 82
3.3.4 Reorganization Energies and Stability 84
3.3.5 Absorption Properties 85
3.3.6 Summary 86
3.4 Conclusion 87

4 Experimental Study of Ethylcarbazole Based Materials 89
4.1 Synthesis of The Studied Materials 89
4.2 X-ray Diffraction Analysis 90
4.2.1 Poly(Ethylcarbazole-Terphenyl) 90
4.2.2 Poly(Ethylcarbazole-Anthracene) 91
4.2.3 Poly(Ethylcarbazole-Furan) 92
4.3 UV-VIS Analysis 93
4.3.1 Poly(Ethylcarbazole-Terphenyl) 93
4.3.2 Poly(Ethylcarbazole-Anthracene) 94
4.3.3 Poly(Ethylcarbazole-Furan) 95
4.4 Scanning Electron Microscopy Analysis 96
4.5 Dielectric Properties and Conduction Mechanism 97
4.5.1 Preparation of The Materials 97
4.5.2 Dielectric Constant 98
4.5.3 Dielectric Loss 101
4.5.4 AC Conductivity 104
4.5.5 Exponent "s" 107
4.5.6 Activation Energy 108
4.6 Conclusion 109

Summary and Future Work 111

References 115

List of figures

1.1 Band gap diagram of metals, semiconductors and insulators. 6
1.2 Structure band of a) Intrinsic semiconductor b) Extrinsic semiconductor. 7
1.3 Structure of Polyacetylene. 8
1.4 Chemical structure of different type of organic semiconductors. 9
1.5 Hybridization of HOMO-LUMO energy levels in a donor-acceptor copolymer. 12
1.6 sp^2 hybridization of the carbon atom. 13
1.7 Molecule hybridization. 13
1.8 Molecular structure of pentacene. 13
1.9 Energy band diagram of the inorganic semiconductor vs organic semiconductore. 14
1.10 General illustration of an OLED. 16
1.11 a) Characteristics of organic field-effect transistors b) Schematic of an OFET device structure. 17
1.12 Schematic of a sensor based on conducting polymer. 20
1.13 Approaches adopted for optimizing the sensing properties of conjugated polymers-based material. 20
1.14 Schematic representation of organic battery. 21
1.15 Principle of solar cells. 23
1.16 Organic cells Efficiency by year. 24
1.17 Structure of a Schottky type cell. 25
1.18 Structure of a typical heterojunction device. 26
1.19 DSSC structure and operational mechanism. 26

2.1 Structures of the studied compounds. R1 = C_8H_{17}R2 = C_6H_{13}R3 = $C_{12}H_{25}$R4 = $C_{10}H_{17}$. 30
2.2 Structures of MK-49. 30
2.3 Structures of PEcbz-Ter), (PEcbz-Ant) and (PEcbz-Fur). 30

2.4 X-ray diffraction principle. 44
2.5 Shimadzu LabX XRD-6100 Diffractometer (Analysis Center, Faculty of Sciences Meknes (F.S.M)) b) Geometric arrangement of X-ray diffractometer 46
2.6 Transitions between molecular orbitals. 47
2.7 a) JASCO V-570 spectrometer (LASMAR Laboratory, Faculty of Sciences Meknes (F.S.M)) b) Basic construction layout of a spectrophotometer 49
2.8 Transitions between molecular orbitals. 51
2.9 Polarization levels. 53
2.10 Distribution of charges in a plane capacitor having (a) vacuum and (b) a dielectric material. 55
2.11 Capacitor containing a material subjected to a sinusoidal electric field. 57
2.12 Diagram of the potentials experienced by carriers which are separated by a distance R in CBH model. 58
2.13 (a) Equivalent diagram of the material studied reproducing a parallel ohmic conductor with a perfect capacitor, (b) Experimental device used for the dielectric study. 60

3.1 Structures of the studied compounds and their optimization R1 = C_8H_{17}R2 = C_6H_{13}R3 = $C_{12}H_{25}$R4 = $C_{10}H_{17}$. 63
3.2 Simulated UV-visible absorption spectra of studied compounds at theTD-DFT/CAM-B3LYP/6-31G (d) level. 66
3.3 Optimized structures of the studied compounds. 71
3.4 Schematic energy diagram, TiO_2 and electrolyte $\left(I^-/I_3^-\right)$. 73
3.5 Contour plots of the frontier orbitals of all dyes. 74
3.6 Critical parameters influenced J_{sc} along of investigated sensitizers: (a) the light-harvesting efficiency, (b) the electronic injection free energy . 76
3.7 The reorganization energy λ_{tot}. 78
3.8 Absorption spectrum of the studied dyes in THF solution. 79
3.9 Optimized geometry of a) PEcbz-Ter, b) PEcbz-Ant, and c) PEcbz-Fur 82
3.10 HOMO and LUMO of a) PEcbz-Ter, b) PEcbz-Ant, and c) PEcbz-Fur. 83

4.1 XRD pattern spectra of PEcbz-Ter, PEcbz-Ter(H) and the starting materials (ECz and Ter) 91
4.2 XRD pattern spectra of PEcbz-Ant, PEcbz-Ant(H) and the starting materials (ECz and Ant) 92
4.3 XRD pattern spectra of PEcbz-Fur and PEcbz-Fur(H) 92

4.4 UV-VIS spectrum of (a) PEcbz-Ter, (b) PEcbz-Ter(H) 94
4.5 UV-VIS spectrum of (a) PEcbz-Ant, (b) PEcbz-Ant(H) 95
4.6 UV-VIS spectra of PEcbz-Fur 96
4.7 SEM images of the studied co-polymers pellets: (a) PEcbz-Ter, (b) PEcbz-Ant and (c) PEcbz-Fur 97
4.8 Dielectric constant of a) PEcbz-Ter, b) PEcbz-Ant and c) PEcbz-Fur as a function of frequency at different temperatures 99
4.9 Dielectric loss vs. frequency of a) PEcbz-Ter, b) PEcbz-Ant and c) PEcbz-Fur at different temperatures. 102
4.10 $\ln(\varepsilon_r'')$ vs. frequency of a) PEcbz-Ter, b) PEcbz-Ant and c) PEcbz-Fur at different temperatures. 103
4.11 AC conductivity vs. frequency of a) PEcbz-Ter, b) PEcbz-Ant and c) PEcbz-Fur at different temperatures. 105
4.12 Ac conductivity as a function of temperature for: a) PEcbz-Ter at different frequencies and b) the PEcbz-Ter, PEcbz-Ant and PEcbz-Fur at 10 kHz. 107
4.13 Exponent "s" as a function of temperature of a) PEcbz-Ter, b) PEcbz-Ant and c) PEcbz-Fur. 108
4.14 Activation energy vs. frequency of a) PEcbz-Ter, b) PEcbz-Ant and c) PEcbz-Fur. 109

List of tables

1.1 Solar Cell Efficiency (data of 2020). 24

3.1 Inter-ring distances d_i(Å) and dihedral angles θ_i(deg) of DOTP, DH4P and ddoD4P obtained at B3LYP/6-31G(d) level of theory 62
3.2 HOMO (eV), LUMO (eV) and E_{gap}(eV) values of the studied compounds. 64
3.3 Absorption data λ_{max}(nm), oscillator strength (f), Excitation energy (eV) obtained by TD-DFT method for the studied compounds. 65
3.4 Absorption parameters λ_{max}(nm), Excitation energy (eV) and oscillator strength (f) of $MK-49$. 70
3.5 Bond lengths (Å) Dihedral angles (Φ) Parameters of all dyes in the ground states. 72
3.6 Calculated Electrochemical Parameters for all dyes. 76
3.7 Ionization potential (IP), electron affinity (EA) and chemical reactivity (in eV) of investigated dyes. 77
3.8 Absorption data λ_{max}(nm), oscillator strength (f), Excitation energy (eV) obtained by TD-DFT methods for the studied compounds. 79
3.9 Inter-ring distances di Å and dihedral angles θ (deg) of PEcbz-Ter, PEcbz-Ant, and PEcbz-Fur. 81
3.10 HOMO (eV), LUMO (eV) and Egap (eV) values of the studied compounds. 84
3.11 Calculated molecular λ_e, λ_h, η, Ionization potential (IP) and Electron affinity (EA) (all in eV) of the copolymers 85
3.12 Calculated maximum absorption wavelengths λ_{max} (nm), the oscillator strength (f), and excitation energies E (eV). 86
3.13 All the properties calculated by DFT. 86

4.1 Dielectric Constant ε'_r and Dielectric Loss $\tan\delta$ at selected frequency. . 100
4.2 Dielectric constant ε'_r, and conductivity σ_{ac}, $\left(\Omega^{-1}\cdot cm^{-1}\right)$ for PEcbz -Ter, $Ph-PHQ$, and P -terphenyl.. 106

4.3 The ratio F at R.T and 120°C for PEcbz-Ter, Ph-PHQ, and P-terphenyl.107

Acronyms

Acronyms / Abbreviations

B3LYP Becke, 3-parameter, Lee–Yang–Parr

BSE Backscattered Electron

CBH Orrelated Barrier Hopping

CP Conjugated Polymer

DFT Density Functional Theory

EA Electron Affinity

EL Electroluminescence

ESS Elechtrochemical Energy Storage System

GGA Generalized Gradient Approximations

HF Hartree–Fock

HOMO Highest Occupied Molecular Orbital

IP Ionization Potential

LDA Local-Density Approximations

LED Light-Emitting Diode

LHE Light Harvesting Efficiency

LUMO Lowest Unoccupied Molecular Orbital

MOSFET Metal–Oxide–Semiconductor Field-Effect Transistor

OFET Organic Field Effect Transistor

OSC Organic Solar Cell

PEcbz-Ant Poly(Ethylcarbazole-Anthracene)

PEcbz-Fur Poly(Ethylcarbazole-Furan)

PEcbz-Ter Poly(Ethylcarbazole-Terphenyl)

SC Semiconductor

SEM Scanning Electron Microscopy

SPT Small Polaron Tunneling

THF Tetrahydrofuran

XC Exchange-Correlation

XRD X-Ray Diffraction

General Introduction

Organic conductive and semiconductor materials are emerging as the key materials for future electronics. Organic electronics offer two major advantages over classical inorganic semiconductors. On the one hand, they allow the design of devices on flexible substrates, thus offering a wide range of new applications requiring the flexibility of the supports [1]. On the other hand, the costs are lower than those of inorganic semiconductors. these materials, polymers, for example, can be used in broad assortment applications such as photovoltaic devices [2, 3], field-effect transistors [4–6], light-emitting diodes [7–9], and capacitive energy storage [10–12]. The conductivity properties of these assemblies depend on two primary parameters: the efficiency of the transport of charges in the polymer and the efficiency of the interchain transport. The latter often represents the performance-limiting parameter and, consequently, the use of polymers designed for various applications. The emerging of π-conjugated materials increased when Shirakawa, MacDiarmid, and Heeger discovered that oxidation with chlorine, bromine, or iodine vapor made polyacetylene films 10^9 times more conductive than they were originally. The three researchers received the Nobel Prize in Chemistry in 2000 for their discovery of polyacetylene, and since then, a new era begins for the π-conjugated materials. Recently, different examples of polymers based on π-conjugated backbones have been developed [13–15]. The π-conjugates represent the delocalization or, in other words, the mobility of electrons along the polymer backbone. In conjugated systems, which have alternating double bonds, the electron density is delocalized and usually leads to the stabilization of the molecule. The mobility of π-electrons contributes to important physical properties, and the chemical properties of aromatic compounds [16].

Indeed, they have the advantage of possessing optical and electronic properties that can be modulated by molecular and supramolecular engineering [17]. These depend on the nature of the monomer units involved as well as the effective lengths of the molecules. Moreover, the theoretical calculations proved their importance in chemistry and conducting organic materials in particular, ascribable to the various limitations

of the experiment. Due to the high level of disorder associated with most of these materials, structural information is not always easy to determine experimentally [18]. There may also be several uncertainties in the determination of the electronic properties linked to the effect of the solvent, the presence of impurities, etc. Therefore, theoretical studies can help determine the structural and electronic properties of these materials and subsequently contribute to a better understanding of the relationship between structure and properties. Thus we apply the density functional theory (DFT) method [19] of the models derived from these materials to determine the structural, electronic, and vibrational proprieties.

One of the suitable polymers used in optoelectronic applications is Polyopyrroles. Pyrrole is an organic compound with a planar heterocyclic structure found frequently in natural complexes and bioactive pigments; research has shown that Polypyrrole has high chemical stability and mechanical resistance to environmental conditions [20]. Besides, the substitution of the pyrrolic rings can enhance the length of conjugation and enable to increase the solubility of the corresponding polymers to promote the polymerization, thus to give a positive impact on the electronic states of the polymer and subsequently lead to an increase in conductivity [21, 22]. Various computational studies used alkyl chain as a substituent to investigate their effect, in most cases, side alkyl-chain, affect light absorption, HOMO-LUMO energies, and considerable potential for the development of the performance of the conjugated polymer.

Further, several Selenophene-containing copolymers have been synthesized and applied in organic field-effect transistors (OFET) [23, 24] and organic solar cells (OSC) [25, 26]. Selenophene is the heavy homolog of the series of chalcogenophenes and mostly shows chemical and physical properties [27], but Polyselenophene has been little studied. The main reasons for the implementation of Selenophenes into these polymers were the expected lower bandgap due to a lower LUMO and higher hole mobility due to the better polarizability of Selenophene, and resulting in strong interchain Se-Se interactions [28]. In a paper reported by Shunsuke Tamba et al. [29], they synthesized and investigated the properties of a Selenophene-analog MK-49 containing organic dye molecules for dye-sensitized photovoltaic cells and obtained promising results. Therefore, we examined them theoretically due to the lack of further studies on this material.

Following the previous material, the conducting polymer Poly(Ethylcarbazole) exhibits advantageous properties with a π-conjugated structure, a right candidate for photovoltaic and electroluminescent devices due to its excellent thermal stability and electronic properties [30, 31]. Carbazole is a wholly aromatic system, very stable to

environmental and chemical degradation. Furthermore, its nitrogen group can be easily substituted to provide solubility to the polymer [32]. Polymers have been widely used as dielectric materials due to their ease of processing, permitting them to be formed into flexible films. On the other hand, high dielectric constant and low dielectric loss polymers are highly desired for advanced electrical applications, such as film capacitors [33], artificial muscle [34], and electrocaloric cooling [35].

However, this polymer exhibits a low dielectric constant over a wide range of temperatures and frequencies. These low properties can be improved to expand its application fields. Other polymers with excellent chemical stability and high dielectric constant can be used as a building block, such as P-terphenyl, which can convert poly(Ethylcarbazole) into a high K material, [36, 37]. These materials can be made as an appropriate choice for the study of electrical properties. Theoretical and experimental approaches based on dielectric studies can provide valuable information that can be used to understand dielectric polarization, dielectric losses, and the behavior of charge carriers in polymers [38]. The dielectric properties are sources of valuable information on the electrical properties of ions, atoms, molecules, and, most importantly, their behavior within materials. Selvakumar et al. [39] reported that the electronic relaxation process is the only process in P-terphenyl. Moreover, through the dielectric analysis, they were able to show that the material is continuous and unbroken, meaning that there are no grain boundaries within the polymer, with only a slight amount of impurity and defect concentrations. Also, the dielectric constant values of P-terphenyl are very high compared to other organic polymers [40]. These high values affect the response time of devices such as solar cells. In this regard, we have combined poly (ethyl carbazole) with P-terphenyl as a building block and two other polymers (anthracene and furan) to improve its dielectric properties. There are no detailed studies on the dielectric properties of carbazole-based copolymers such as Ethylcarbazole Poly (Ethylcarbazole-Terphenyl) (PEcbz-Ter), Poly (Ethylcarbazole-Anthracene) (PEcbz-Ant), and Poly (Ethylcarbazole-Furan) (PEcbz-Fur) which used in this thesis.

This thesis was carried out in the Engineering Sciences Laboratory at the Faculty of Taza, Sidi Mohamed Ben Abdallah University, Fes. This thesis is mainly concerned with the experimental and theoretical study of different organic materials for optoelectronic applications, and it is divided into four chapters :

Chapter one devoted to discussing the fundamentals of organic materials and their application in the industrial field.

Chapter two deals with the basic concepts and experimental tools used to characterize the studied organic materials and the theory behind the computational calculations using Density Functional Theory (DFT).

Chapter three is dedicated to a fully computational study of our materials. In this chapter, we examined the effect of the elongation of the 3,3'-dioctylterpyrrole (DOTP) and 3,3'- dihexylquaterpyrrole (DH4P) on the geometric, electronic, and absorption properties, as well as the effects of alkyl chain in 3,3'- dihexylquaterpyrrole (DH4P) and 3-3,7– dimethyldienyloctyl-3'dodecylquaterpyrrole (ddoD4P), followed by a study of dye sensitizers based on Selenophene as a p-spacer, to examine the geometric, electronic, optical and photovoltaic properties. Finally, the same study was applied to the three copolymers (PEcbz-Ter), (PEcbz-Ant), and (PEcbz-Fur).

Chapter four deals with the characterization measurement based on X-ray diffraction, UV-vis absorption, and scanning electron microscopy to obtain an insight into the structure of PEcbz-Ter, PEcbz-Ant, and PEcbz-Fur. Then, The dielectric constant, dielectric loss, and the AC conductivity mechanism of these copolymers as a function of frequency and a temperature range from 1 kHz to 2 MHz and room temperature to 120°C, respectively, are measured and compared.

Chapter 1

Background Literature

In this chapter, we will present a general overview of conjugated organic materials, which constitute an interesting alternative for electronic devices instead of inorganic materials. Their structural diversity, Physico-chemical properties, as well as their practical use, will be discussed.

1.1 Semi-conductor

A semiconductor is a material located between the conductor and the insulator. A pure (intrinsic) semiconductor is not a good conductor nor an excellent insulator. The most widely used single elements for semiconductors are Silicon, Germanium, and Carbon[41–43]. Elements such as Gallium arsenide are also commonly used for semiconductors[44]. Atoms with four valence electrons characterize as single element semiconductors. The typical semiconductor has a resistivity in the range of 10^{-5} to $10^{-7}\Omega \cdot \mathrm{m}$. Remember that the valence shell of an atom represents a band of a particular energy level, and valence electrons are confined to this band. When an electron acquires enough additional energy from an external source, it can leave the valence shell, become a free electron, and exist in what is referred to as the conduction band. In terms of energy, the difference between the valence band and the conduction band is called an energy gap. It is the amount of energy an electron must have to jump from the valence band to the conduction band. Once in the conduction band, the electron is free to move through the material and is no longer bonded to any particular atom. Fig.1.1 shows the energy diagrams for an insulator, semiconductor, and conductor. This band structure explains the different types of materials. In Fig. 1.1, we notice three distinct cases. Note, in the first part, the overlapping energy bands in a conductor, allowing electrons to move almost freely. In a conductive material,

there is always a large number of free electrons. In the second part, we notice that a semiconductor has a narrower energy gap, allowing a few electrons to jump towards the conduction band and become free electrons.

In contrast, in insulators, a large energy gap between the bands can be of the order of 10 eV or more. This region is called the "forbidden band." Valence electrons are not able to jump to the conduction band except when sufficient energy is supplied by heating or by optical excitation [45].

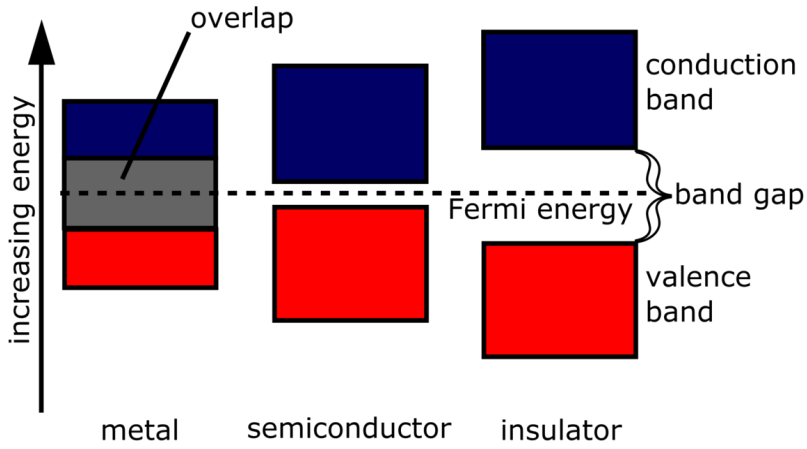


Fig. 1.1 Band gap diagram of metals, semiconductors and insulators.

1.1.1 Inorganic Semi-conductor

The best-known Semiconductor is the Si element, as mentioned above. Together with germanium (Ge), this is the prototype of a large class of semiconductors with similar crystal structures. Si and Ge's crystal structure is similar to that of a diamond. In this arrangement, each atom is surrounded by four nearest neighboring atoms (it is said that each atom is coordinated fourfold), forming a tetrahedron. Such tetrahedrally bonded semiconductors form the backbone of modern technology and the keystone of the electronic industry. Some elements from the groups V and VI of the periodical table, such as sulfur (S), selenium (Se), tellurium (Te), phosphorus (P), and Gallium arsenide (GaAs) are also semiconductors [46–48]. The atoms in these crystals may be three-fold (P), two-fold (S, Se, Te), or four-fold in coordination. As a result, these elements can be found in many different crystal structures [49]. For example, GaAs is of great technical importance for optoelectronic devices. It essentially has the same crystal structure and the same total number of valence electrons as the element silicon. Gallium arsenide is of great technical interest, partially because of its large bandgap,

which essentially prevents intrinsic contributions in impurity semiconductors even at elevated temperatures, partially because of its larger electron mobility, which aids in high-speed applications, and particularly because of its optical properties [50].

The Semiconductor in electronics is classified into intrinsic and extrinsic semiconductors. The pure form of the Semiconductor is known as the intrinsic Semiconductor, which has no foreign atoms in its crystal lattice. On the other hand, an extrinsic semiconductor is to which we add impurities at a controlled rate to make it conductive. For example, in Silicon, all electrons participate in Si-Si covalent bonds when it is pure. A significant amount of energy will have to be supplied to ionize these electrons and make them pass through the conduction band. It is possible to deliberately introduce foreign atoms into the crystal lattice, which will play the role of impurities. In the case of Silicon, it is possible to introduce pentavalent elements such as phosphorus or arsenic, which produces a disturbance in the conduction electron distribution by providing additional electrons. These electrons are much more easily ionizable and correspond to the electrons from a new energy level (donor level), located in the gap and close to the conduction band, making it an n-doped semiconductor. The same reasoning can be applied by replacing the pentavalent elements with trivalent atoms, such as boron or aluminum, that creates a void in the lattice, which we call a hole. Since the electron is deficient (acceptor level), the hole readily accepts an electron, making it a P-type semiconductor.

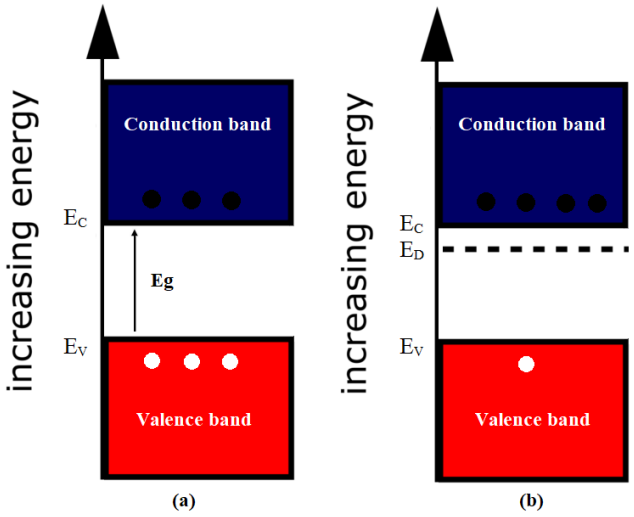


Fig. 1.2 Structure band of a) Intrinsic semiconductor b) Extrinsic semiconductor.

Fig. 1.2 shows the band structure of an intrinsic and extrinsic semiconductor. for the intrinsic case, the number of electrons in the conduction band is equal to the number

of holes in the valence band, as seen in Fig. 1.2 (a), Whereas the number of electrons in the conduction band is greater than that of holes in the extrinsic semiconductor valence band, Fig. 1.2 (b). The introduction of doping atoms allows the appearance of a new energy level E_D in the semiconductor gap close to the conduction band. This additional energy level reduces the gap, especially as it is close to the conduction band.

1.1.2 Organic Semi-conductor

By analogy with inorganic semiconductors, organic semiconductors include carbon-based molecules with semiconductor properties. These molecules are arousing the interest of scientific and industrial communities in the development of modular and low-cost electronics [51]. An organic semiconductor is an organic compound in the form of a crystal or a polymer. It exhibits properties similar to inorganic semiconductors that are more familiar than organic ones due to their relatively mature role in computer-integrated circuits, telecommunications, and other consumer electronic devices. The properties are manifested in conduction by electrons and holes, as well as the presence of a bandgap. These materials gave rise to organic electronics [52].

Many organic compounds, such as polyacetylene $[(CH_2)_n]$ (Fig. 1.3), are semiconductors [53]. The advantage of organic over inorganic semiconductors is that they can be easily tailored to the applications. For example, compounds containing conjugate bonds such as $-C=C-C=$ have large optical nonlinearities and may have essential optoelectronics applications. The bandgaps of these compounds can be changed more easily than inorganic semiconductors to suit the application by changing their chemical formulas [54].

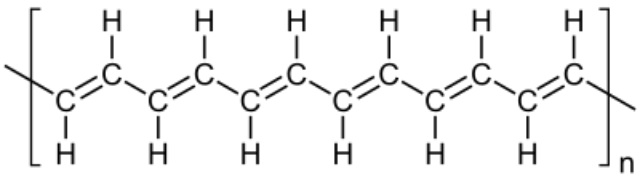


Fig. 1.3 Structure of Polyacetylene.

1.1.3 The Different Types of Organic Semiconductor materials

Organic semiconductors can be classified into several classes, such as small molecules based on (hetero) aromatic rings, conjugated polymers, and hybrid organic-inorganic

structures [55]. All these structures exhibit the characteristic feature of having conjugated bonds, in which the presence of mobile (highly polarizable) pi-electrons has a dramatic impact on the potential electrical performance. This situation is reversed compared to non-conjugated or all-σ compounds, such as polyethylene and Teflon, which are excellent insulators. Fig. 1.4 shows the different types of organic semiconductors used in electronics.

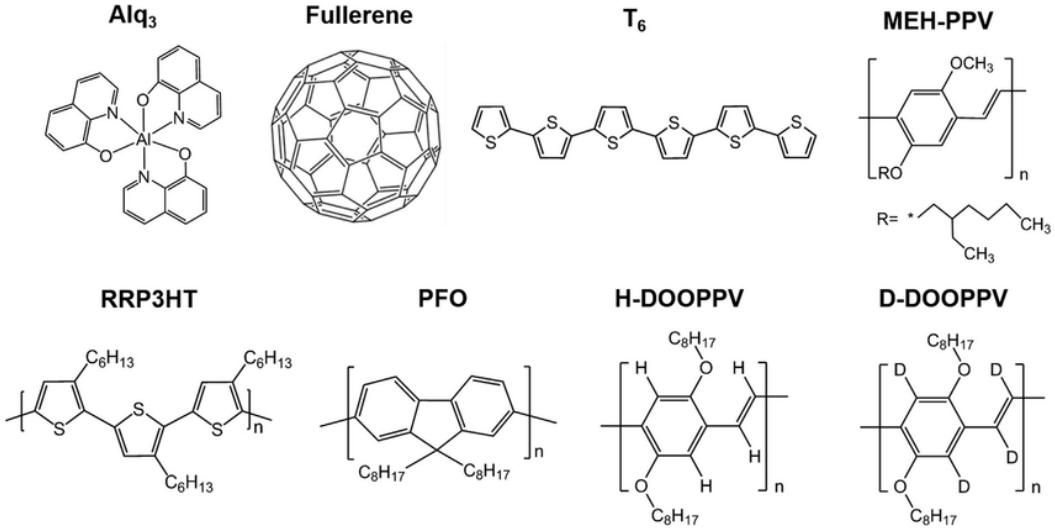


Fig. 1.4 Chemical structure of different type of organic semiconductors.

1.1.4 Conjugated Polymers

The defining feature of a conjugated polymer is the presence of alternating single and double bonds along the polymer backbone. They are intrinsically part of the organic semiconductor family. As a reminder, according to band theory (Fig. 1.1), a semiconductor is a material that has a valence band and a conduction band separated by a bandgap that is small enough to allow the transport of mobile charge carriers at room temperature, unlike an insulator where the band gap is too high to have charge carriers in the conduction band. In the neutral state, a π-conjugated polymer is a semiconductor, while it becomes a conductor like metal when doped by oxidation or partial reduction. However, unlike metals, π-conjugated polymers possess the mechanical characteristics of plastics. Indeed, the π-conjugated polymers are light, flexible, and inexpensive to implement [56–58]. The semiconductor properties of these polymers, such as bandgap, conduction band energy (LUMO), and valence band energy (HOMO), can be easily modulated to obtain a wide range of different properties that can thus satisfy the requirements of various applications in organic electronics.

1.1.5 History and Progress of π-conjugated Polymers

1.1.5.1 Historical Context

Nowadays, polymer materials are involved in every aspect of our lives. In the more specialized fields of optics and electronics, synthetic polymers have traditionally been used as packaging materials like electrical insulators or photosensitive resins. However, the world of polymers has been turned upside down with the discovery of both electroactive and photoactive π-conjugated polymers, leading to a multitude of possible new applications [59].

The development of the organic electronics sector based on π-conjugated polymers have been somewhat accidental. A student of Professor Hideki Shirakawa at the Tokyo Institute of Technology was working on the manufacture of polyacetylene (Fig. 1.3), section 1.1.6 using the Ziegler-Natta polymerization reaction. By mistake, the student prepared a multi-polar concentration of the catalyst rather than the usual millimolar concentration.

This error led to the formation of a thin layer of polyacetylene, which had a metal sheet's appearance, unlike the usual black powder that was usually obtained. During a visit to Japan, Professor A. G. MacDiarmid Department of Chemistry, University of Pennsylvania, met with Professor Shirakawa and was fascinated by this thin polymer layer sparkling. Professor MacDiarmid then invited Professor Shirakawa to Philadelphia to further study this new form of polyacetylene.

In 1977, the trio formed by Professors Shirakawa, MacDiarmid and a fellow physicist, Professor A.J. Heeger, reported that following partial oxidation of the material with bromine or iodine, the electrical conductivity of polyacetylene (an inherently semiconductive polymer) increases by a factor of more than one million to 100 S/cm[1].

Electrical conductivities of the order of 105 S/cm are obtained with highly crystalline forms of polyacetylene [60]. The three professors explained that the delocalized electronic structure stemming from the alternation of single and double bonds of polyacetylene was responsible for the excellent intrachain and interchain mobility of charge carriers created by doping. This delocalized structure, called the conjugate structure, is also responsible for the high absorption of polyacetylene in the UV-visible region. The three researchers (Shirakawa, MacDiarmid, Heeger) finally received the Nobel Prize in Chemistry in 2000 for their discovery on polyacetylene. This discovery paved the way for developing an entirely new field of research in which polymers are no longer used for their insulating properties, but rather for their optical and electronic properties: organic electronics.

1.1.5.2 Progress of π-conjugated Polymers

Although the discovery of the doped polyacetylene had created an enormous enthusiasm, the same polymer had little future. Indeed, being insoluble, infusible, and photo-unstable, polyacetylene did not meet the requirements of this new organic electronic field. However, this discovery motivated the scientific community to embark on the development of new, more stable, and more soluble conjugated polymers. In the early 1980s, several studies were conducted on Polythiophene [61], Polypyrrole [62], and Polyaniline [63] synthesized by electropolymerization.

Even though these polymers are much more stable than polyacetylene due to the use of aromatic rings in the main chain, they were still not soluble materials. On the other hand, according to the electrochemical potential, it was possible to switch from the non-doped semiconductor state to the oxidized or reduced conductor state. Despite these attractive properties, the ultimate aim was to develop polymer materials incorporating both the electrical and optical properties of semiconductors and the mechanical properties of conventional polymers.

In the meantime, the scientific community's attention has shifted to the study and design of stable semiconductor polymers rather than continuing research on highly conductive π-conjugated polymers. This new orientation was carried out to initiate the era of plastic electronics, where microelectronic devices could be printed on different substrates using conventional means of implementation. Thus, the optical and electronic properties of existing polymers had to be modified to obtain semiconductors with a small bandgap. There are several known ways to modulate the bandgap, among which the stiffening of the conjugated main chain [64], the introduction of electro-attractant or electron donor side functional groups [65], and the increase of the quinoid [66] in the main chain concerning the aromatic character. These methods have been widely used in recent years to modulate the bandgap of the π-conjugated polymers.

On the other hand, the most efficient approach for modulating the bandgap is to synthesize an alternating copolymer from an electron-rich monomer and an electron-poor monomer, thereby creating an architecture commonly known as acceptor [67]. As shown in Fig. 1.5, when these two types of monomers are combined in an alternating copolymer, hybridization of the molecular orbitals occurs between the electron-poor monomer and the electron-rich monomer leading to significant modulation of the bandgap of the resulting polymer.

Generally, the energy level of the highest occupied energy molecular orbital (HOMO) of the resulting copolymer is determined by the electron-rich unit, while the electron-

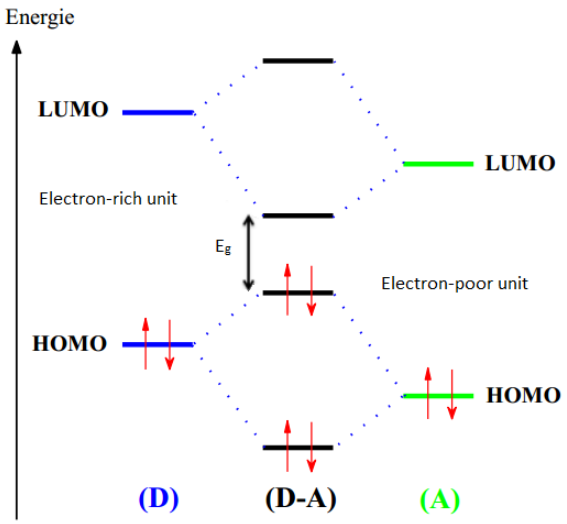


Fig. 1.5 Hybridization of HOMO-LUMO energy levels in a donor-acceptor copolymer.

poor unit determines the energy level of the lowest unoccupied energy molecular orbital (LUMO).

To this day, the scientific community is attempting to modulate the energy levels of new π-conjugated polymers, primarily using the alternating donor-acceptor copolymer method. The methods of synthesizing have made great strides leading to evolved polymers.

1.1.6 Structure of Conjugated Polymers

The semiconductor character of conjugated polymers comes from the nature of the bonds between the carbon atoms. Each carbon atom along the polymer chain has valence electrons in one 2s and three 2p (p_x, p_y, and p_z) atomic orbitals. When a carbon atom is bonded to three other atoms, the 2s atomic orbital combines with two of the 2p atomic orbitals, resulting in the formation of three equivalent sp^2 hybridized orbitals (Fig. 1.6). These three hybrid orbitals lie at approximately 120° angles in a plane that can be influenced by neighboring atoms. The remaining 2p orbital, which is nominally taken as the p_z orbital, is perpendicular to this plane. This type of hybridization leads to the formation of σ bonds between carbon atoms, which ensures the coherence of the carbon backbone of the molecule [68].

After forming the double bond, the carbon atom is thus surrounded by three sp^2 hybrid orbitals and a $2p_z$ orbital oriented perpendicular to the plane formed by the sp^2 orbitals Fig. 1.6. The remaining Pz orbitals between consecutive atoms overlap

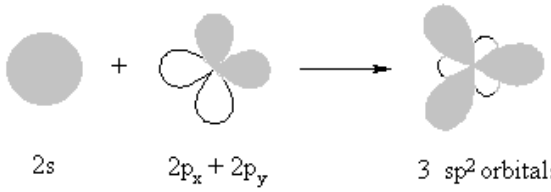


Fig. 1.6 sp^2 hybridization of the carbon atom.

to a lesser degree, resulting in the formation of weaker bonding orbitals (π^*) and antibonding orbitals (π). Electrons filling these bonding orbitals are responsible for the formation of pi-bonds along the chain and weak $\pi - \pi$ interactions between chains Fig.1.7.

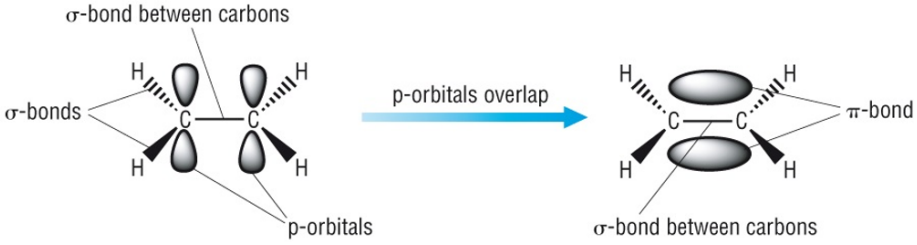


Fig. 1.7 Molecule hybridization.

Given the substantial axial overlap, the transition energies of the orbitals sigma and σ and σ^* (bonding and antibonding) are vital compared with those of the π and π^* orbitals for which the lateral overlap is less efficient [69]. Therefore, in materials where these bonds are predominant, electrons can hardly move and participate in the conduction. On the other hand, if the neighboring atoms have a p_z orbital, a π orbitals system is created, allowing the electrons to move along the backbone chain, as in the case of pentacene Fig. 1.8.

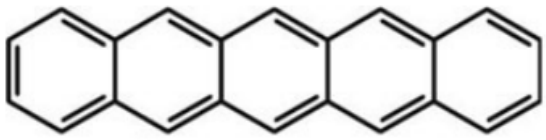


Fig. 1.8 Molecular structure of pentacene.

1.1.7 Energy Levels of Conjugated Polymers

The isolated molecules have discrete energy levels; these energy levels depend on the molecule's electronic orbitals. The molecular orbitals of two molecules can bond or

influence by the presence of each other when their proximity is sufficient. As the number of molecules increases, each interaction will create a hybridization with which a vibrational sub-level is associated and correspond to a new energy level. If the number of molecules is large, it is no longer possible to perceive the discrete of the number of energy levels, and we observe the creation of a continuum energy levels [70].

As mentioned in the previous section, two types of hybridization are possible. First, the electrons of molecular orbitals are strongly localized on a bond or a group of molecules. Second, the electrons of the orbitals are delocalized and free to move between atomic sites. These two different hybridizations can be seen in molecules like methane and ethylene. The overlap of s orbitals gives a single strong bond of type σ, while the overlap of p orbitals can form a bond of type π double. It should be kept in mind that a σ bond is localized while a π bond can be delocalized [70].

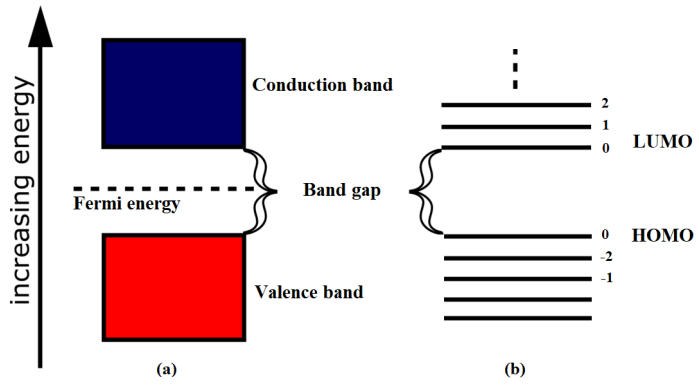


Fig. 1.9 Energy band diagram of the inorganic semiconductor vs organic semiconductore.

To be more specific, a correct representation of the energy level diagram is depicted in Fig. 1.9, showing the difference between the energy band diagram of the inorganic and organic semiconductors. In charge transfers in organic semiconductors, hole transport occurs in the highest occupied molecular orbit (HOMO), which is formed by overlapping molecular pi-orbitals. Similarly, electron transport results from the overlap between anti-bonding π-orbitals (π^*) and occurs in the lowest occupied molecular orbit (LUMO). The energy needed for pumping an electron from the HOMO to the LUMO is referred to as the HOMO-LUMO, E_g, and is analogous to the valence-conduction bandgap in inorganic semiconductor.

1.1.8 Charge Transport in Conjugated Polymers

The conductivity of organic semiconductors increases with temperature, but the models we use for inorganic semiconductors are challenging to apply, mainly because the

degree of crystallinity of organics is low. Thus it is necessary to invoke other models to illustrate the charge transport in organic semiconductors [71]. In the case of organic molecules deposited on the surface of a sample, the orbital overlap of intermolecular is very low, which favors by the hopping conduction or, in other words, the molecule hopping. This mode of transport is most favored as the crystal order within the film is weak. In this case, the conductivity σ is described by Mott's law given below [72]:

$$\sigma = \sigma_0 e^{-(T_0/T)^{1/d+1}} \tag{1.1}$$

where σ_0 represents a constant, T_0 the Mott temperature and d the system dimension. For a space of dimension 3, the expression of the Mott temperature is described by (1.2):

$$T_0 = \frac{18}{k_{\mathrm{B}}\xi^3 N\left(E_{\mathrm{F}}\right)} \tag{1.2}$$

where ξ is the localization length and $N\left(E_{\mathrm{F}}\right)$ the density of localized states at Fermi level. In the next chapters we will discuss this mechanism in details.

1.2 Application of π-conjugated polymers

Since the discovery of the doped polyacetylene by Heeger, MacDiarmid, and Shirakawa, π-conjugated polymers have been intensively studied for microelectronic applications. All the synthetic tools developed subsequently enabled chemists and engineers to synthesize a vast number of semiconductor polymers that could be used in various electronic devices such as light-emitting diodes (LEDs) [73], field-effect transistors [74], solar cells [75] and a growing list of new applications. For example, water-soluble and luminescent π-conjugated polymers can be used for the rapid, specific, and highly sensitive detection of DNA [76], RNA [77] and unlabeled proteins (Detection of poison gases). This new field of chemical and biological sensors based on π-conjugated polymers is continuously expanding, but will not be explored further in this thesis. The work of this study focuses on new π-conjugated polymers for optoelectronic applications.

1.2.1 Light Emitting Diodes (OLEDs)

Electroluminescence (EL) in organic polymers was first discovered in single anthracene crystals by Helfrich and Schneider (1965) [78]. The origin of light electro generation in organic semiconductors is under discussion. Nevertheless, the most accepted mechanism

remains the one developed at that time. The working principle of organic electroluminescence is simple: it consists of a voltage V applied to the organic semiconductor. Here, holes and electrons are injected from the valence band and the conduction band, respectively, where their recombination in the center of the layers ultimately generates photons that give rise to electroluminescence (EL) Fig. 1.10. The emitted light's wavelength depends on the difference in the energy level between the valence band, the conduction band, and the Coulomb force connecting the electron and the hole at the time of recombination [70]..

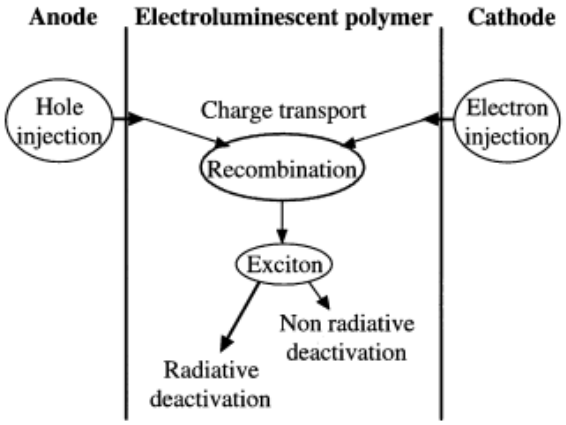


Fig. 1.10 General illustration of an OLED.

1.2.2 Organic Field Effect Transistors

Basic Principles of Field-effect Transistors

Organic transistors are devices with three connection terminals like their silicon counterparts Fig. 1.11 b), make it possible to control the electric current flowing between two electrodes (the source and the drain), thanks to a control of the potential at the third electrode (the gate). Organic field-effect transistors operate similarly to conventional MOSFETs ("metal-oxide-semiconductor FET") or TFT ("thin-film transistors) employing an electric field established through an insulator (or dielectric) separating the semiconductor gate. This electric field can modulate the current flowing through the semiconductor material, thus creating a link between the gate voltage V_{GS} and the current drain I_{D}.

Fig. 1.11 a) shows the typical output characteristics of an organic P-type field effect transistor. Three regions govern the working mechanism of the OFET. First, is the off-state, when a negative gate bias is applied, the current between the drain and source

electrodes is very low or even nonexistent. Therefore additional potential is necessary for the holes to accumulate. Indeed, there are many traps in the semiconductor layer, which can be quite deep, thus trapping the charges, and it can occur at the semiconductor/dielectric interface. Accordingly, the switchover between the off-state and the on-state will not take place at $V_G = 0$ but at a certain potential called the threshold voltage, V_{th} . By applying simultaneously, a drain-source bias with a gate voltage such that ($V_{GS} > V_{DS} > 0$) the holes are accumulated in a non-homogeneous manner since the distribution of the potential is variable throughout the channel and a current I_{DS} appears, this is what it called the linear regime. As the gate voltage increases reaching the condition ($V_{DS} > V_{GS} > 0$), a saturation zone appears at the level of the source electrode (saturation regime)[79, 80].

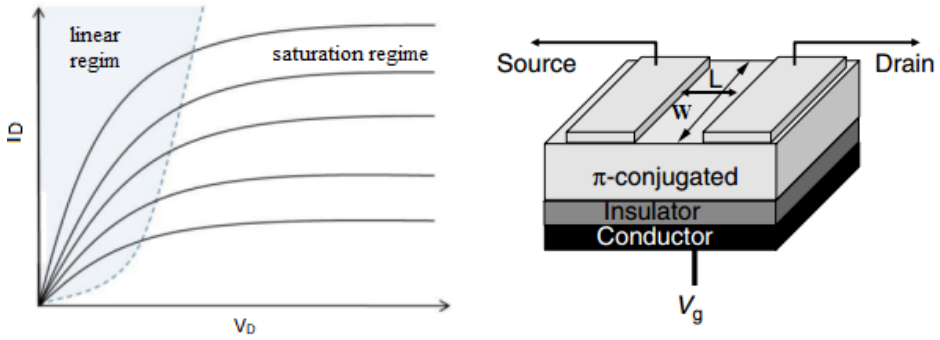


Fig. 1.11 a) Characteristics of organic field-effect transistors b) Schematic of an OFET device structure.

Parameters of OFET

Mobility

The mobility of charge carriers is undoubtedly one of the most critical parameters for a transistor. It is most often used to compare the performance between several transistors. This is the coefficient of proportionality between charge carriers velocity in the active layer and the applied electric field. Therefore, this mobility depends on the materials used not only for the active layer but also for the other layers, since the charges cross the organic semiconductor/metal interface and then the organic semiconductor. The dielectric's roughness, the dipoles at the surface of the dielectric, and the contact resistance are also parameters that strongly influence the mobility [80]. The latter is therefore specific to the device and not intrinsic to the semiconductor, as is often reported in the literature.

Under biases where $V_G < V_T$, we are in cutoff and no current flows because of in an OFET no available mobile carriers.

$$I_D = 0A \tag{1.3}$$

At small V_D and larger V_G , where $V_G - V_D > V_T$, the transistor is said to be in the linear region, the drain current is directly proportional to V_G, and the field-effect mobility (μ_{lin}) in the linear regime can be extracted from the gradient of I_D versus V_G at constant V_D.

$$I_D = \frac{W}{L} C_i \mu \left(V_G - V_T - \frac{V_D}{2} \right) V_D \tag{1.4}$$

As V_{DS} increased, when $V_G - V_D < V_T$, the current reduces its rate of increase because of the onset of pinch-off. The current cannot increase anymore and saturates. We can determine the current at the saturation point by substituting $V_{DS} = V_{GS} - V_T$ in the linear region equation and simplifying to determine:

$$I_D = \frac{W}{2L} C_i \mu (V_G - V_T)^2 \tag{1.5}$$

It is noted that the mobilities extracted in linear or saturation regimes do not necessarily reflect the intrinsic mobility of the semiconductor. The extracted value depends on the dielectric roughness, the presence of dipole on the surface of the dielectric, and the resistance of the contacts at the semiconductor/electrode interface. Consequently, it is always more reasonable to obtain mobility in a linear system where the charge density is most uniform [80]. This is generally achieved via the transconductance gm, which follows from the first derivative of $\mu = \frac{v}{F} = \frac{d^2}{V} t$, with respect to gate voltage.

$$\mu = \frac{L}{W C_i V_D} \frac{\partial I_D}{\partial V_G} \tag{1.6}$$

The ratio of the on/off-state Current

Another important OFET parameter derived from the transfer characteristics is the current on-off ratio. It is the ratio of the drain currents when the transistor is in the saturation regime (maximum current) and cutoff mode (minimum current). In practice, I_{off} determined as the minimum current of the transfer curve and I_{on} as the maximum current. From an application point of view, this relationship is critical, as it determines the efficiency of the transistor as an electrical switch. In logic circuits, it defines the

levels 0 and 1. That value should be as significant as possible for the transistor's best performing behavior. The current I_{on} depends directly on the mobility and dimensions (L and W) of the channel. The I_{off} current is particularly indicative of the residual dopants present in the organic semiconductor and the leakage currents of the insulator [81].

Threshold Voltage

Threshold voltage comes from many factors and is heavily dependent on the organic semiconductor and dielectric used. The threshold voltage V_{th} is the voltage from which charges start to build up in the channel. This voltage should be zero since the transistor only switches to the ON state in the accumulation mode. However, many parameters can influence this voltage, such as the impurities, which have intrinsic doping in the organic semiconductor, and also the presence of charge traps at the semiconductor/gate insulator interface. Moreover, it can be reduced by increasing the gate capacitance, which at lower applied voltages, produces further charges. For certain situations, the threshold voltage for a particular system is not always constant. The V_{th} tends to increase when organic transistors are operated under an extended time scale. This is called bias stress activity and has a major impact on organic transistor applicability in electrical circuits and actual applications[82].

1.2.3 Sensors

Conjugated polymers are also used as sensory materials due to their high sensing properties, thermal stability, and excellent processability. In general, there are different types of sensors based on conducting polymers, classified following changes in the properties of conducting polymers. These changes involve changes in doping level, optical properties, and changes due to weak interactions. Furthermore, organic sensors can be based on various conducting polymers such as polyaniline, polythiophene, and polypyrrole for a wide variety of sensor applications. As an example, The humidity sensor using chemically synthesized poly (1,5-diaminonaphthalene) doped with carbon has been reported by Shim et al [83]. A polypyrrole based potassium micro sensor containing polypyrrole in plasticized polyvinyl chloride membranes, has also been reported by Zachara et al [84]. In this section, we explain the working mechanism of the polymer-based sensors.

A typical sensor device requires two principal components (i) sensing material (i.e., conjugated polymer) and (ii) transducer Fig. 1.12 [85]. To fabricate a sensor, a good

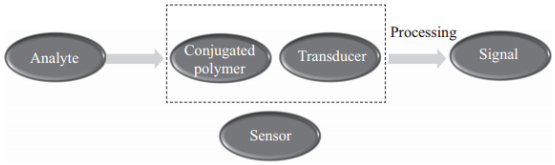


Fig. 1.12 Schematic of a sensor based on conducting polymer.

quality thick or thin film that is uniform and free of pin-holes is needed. For this purpose, several techniques are used, such as dip coating, drop-casting, spin coating, inkjet printing, slot-die coating, and screen printing. In the sensor device, the CP interacts with the analyte. The transducer detects the resultant changes in the physical properties of the CP and converts to a measurable parameter, which is then processed using a suitable electronic system to generate the final signal.

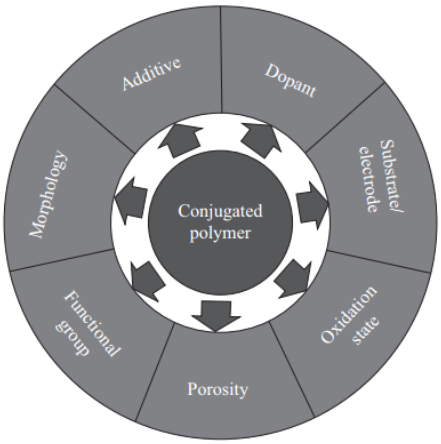


Fig. 1.13 Approaches adopted for optimizing the sensing properties of conjugated polymers-based material.

Several parameters are involved in the interaction of the analyte with the CP, such as film morphology, structure, work function, ionization potential, and electron affinity (IP, EA). Therefore, the choice of CP as sensing material must be based on many factors that need to be optimized. Fig. 1.13 shows the factor optimization approaches for CP, include high surface-to-volume ratio for enhanced response, chemical functionality to improve selectivity, crystallinity, or structural ordering to having efficient charge transfer and fast adsorption/desorption kinetics for quick response/recovery.

1.2.4 Storage Applications

Electrochemical energy storage systems (ESSs) have a tremendous role in technical applications. They are essential and useful to store energy produced by traditional nuclear and thermal power generation or from renewable power sources. They are even used in personal electronics such as computers, communication devices, industrial controls, electric vehicles, spaceships, and laboratory equipment [86]. Current ESSs have been made with traditional metal-based inorganic compounds. These materials sometimes have problems with toxicity and environmental issues relating to wastes and synthesis using extraction methods that release toxic materials [87]. Thus, CP become attractive candidate materials for storage applications due to their combined high electrical conductivity, high environmental stability, low cost, easy fabrication, flexibility, and most importantly, they have high excellent electrochemical storage performance compared with metal-based inorganic active materials. The ability of CP to store charges arises from a doping process. After doping, the CP becomes electronically conductive.

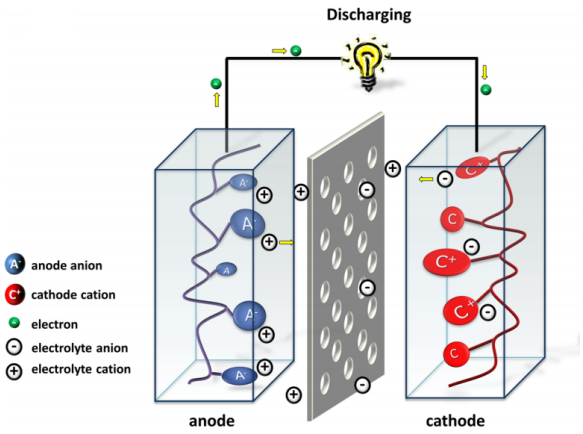


Fig. 1.14 Schematic representation of organic battery.

In electrochemical power sources, chemical energy is converted into electrical energy. During this conversion, the essential requirement for a cathode or active anode material (either inorganic or organic) is to undergo a redox reaction, a one-component is oxidized and transfers its electrons over an external circuit to another redox-active species, which is reduced. For organics, the redox reaction is based on the charge state change of the electroactive organic group or moiety. The best-known and simplest electrochemical cell is the galvanic element [88], generally consists of two electrode materials with different redox potentials, placed in electrolyte solutions connected by a salt bridge or a porous membrane Fig. 1.14. The general structure and principle mode of operation remains

the same for all electrochemical cells. The three crucial components of electrochemical cells are the anode, cathode, and electrolyte. In contrast to inorganic materials with performance based on complex intercalation mechanisms in redox reactions, organic polymers' electrochemical storage mechanism is based on simple redox reactions, leading to high rate performance and long life cycle [89].

1.2.5 Organic Photovoltaic Cells

Solar energy is a very attractive solution to meet society's needs for green and renewable energy while preserving the environment. For example, it is well known that the sun provides in one hour over the entire surface of the planet what humanity consumes in energy for a whole year [90]. On the other hand, the large-scale development of solar technology is limited by the relatively high costs of producing and installing solar panels compared to their current efficiency. Several studies suggest that solar panel costs should be reduced by a factor of 5 to 10 in order to be competitive with other well-known energy sources such as hydroelectricity, nuclear, wind and fossil fuels [91]. To this end, electroactive and photoactive π-conjugated polymers are considered to be very promising candidates for reducing the cost of producing solar energy. These polymers can be solubilized with common organic solvents and then implemented using techniques already widely used with thermoplastic materials and the manufacture of various devices, such as inkjet printing, spin coating or large-scale continuous printing. Types and operation modes of different Organic photovoltaic cells will be discussed in the next section.

Types of Organic Cells

Inorganic Solar cells

In the thesis, we will not dwell on the inorganic solar cell; thus, this paragraph is just a concise description of these systems for comparison purposes only. The photovoltaic effect, i.e. light induced voltage, was discovered in 1839 by the French physicist E. Becquerel when he shed light onto an AgCl electrode in an electrolyte solution [92]. In 1883, Fritts demonstrated the first solid-state solar cell by depositing a thin film of Au on Se semiconductor [93]. The semiconductor acted as the light absorber to convert photons into electron-hole pairs, and the internal electric field separated the photo-excited charge carriers at the Au/S Schottky junction. In all the inorganic solar cells today, the two fundamental processes, namely light absorption and charge separation, are still the basis. Efficient photovoltaic cells for the conversion of solar

energy into electric energy were firstly demonstrated at Bell laboratory in 1954. Their cell employed a single-crystal Si (Si-Si) wafer for light absorption and a p-n junction for charge separation, with an efficiency of 5%.

The operation principle of all photovoltaics cells in general based on the sun which is the unlimited source of energy for this systems. Solar energy arrives in the form of light radiation with wavelengths ranging from ultraviolet to infrared with a peak in the field of the visible located at 550 nm that is in yellow-green. The Sun radiates most of its energy in the short wavelengths. A great amount of the sunlight absorbed, scattered, and reflected by (air molecules, water vapor, clouds, dust and etc.), the energy that used by solar panel is a distribution between the direct energy that affects the earth's surface (31%), and a diffuse energy that also affects the earth's surface (16%). Solar irradiation arrives outside the Earth's atmosphere with a strength of around 1,367 watts per square meter. The thickness of the atmosphere, which passes through the spectrum of solar radiation, has a great effect on the received power. International standards define various spectrum types: AM1 (in Ecuador for air mass 1 as radiation passesed through the thickness of the atmosphere), AM0 (spectrum on the outer surface of the atmosphere), AM15 (spectrum used for standardized testing of solar panels corresponding to the passage of an atmosphere and a half). The overall solar power on Earth's surface is around 1 000 W/m^2 perpendicular to the surface of the rays; it is called power 1.5, which is the reference in the measurement of efficiency [94].

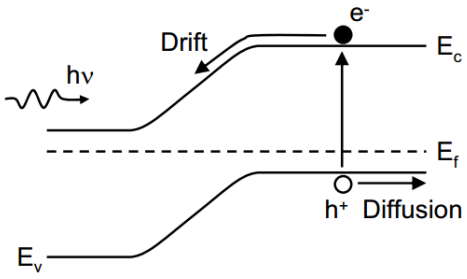


Fig. 1.15 Principle of solar cells.

Fig. 1.15 illustrates the principle of this cell. The solar cell is none other than a photodiode (pn junction) which operates without external polarization and delivers a photocurrent. In general, when an inorganic semiconductor receives solar radiation, photons generate bonded electron-hole pairs (excitons) that separate to generate charge carriers from the valence band to the conduction band. This makes the quality of the entire photodiode critical in terms of minority carrier lifetime and carrier mobility for high efficiency [94].

The majority of solar panels use crystalline semiconductors and exhibit an efficient energy conversion efficiency of up to 40% with solar concentrators. The most used materials are: silicon and compounds of group III-V.

In comparison with inorganic solar cells, the benefits of using organic solar cells are manifold: they are lightweight, easy to produce, and can be used as flexible devices. Organic solar cells are easy to integrate, and above all, they are 1000 times thinner than silicon solar cells. Hence, it results in huge savings on materials, and consequently, they are cheaper. Regarding the drawbacks, their efficiency is lower than that of a silicon solar cell for about 10% (see Table 1.1) [95]. In addition, in OSC, the charges cannot flow easily, this is due to bad generation as well as the extraction of electric charges in the OSC.

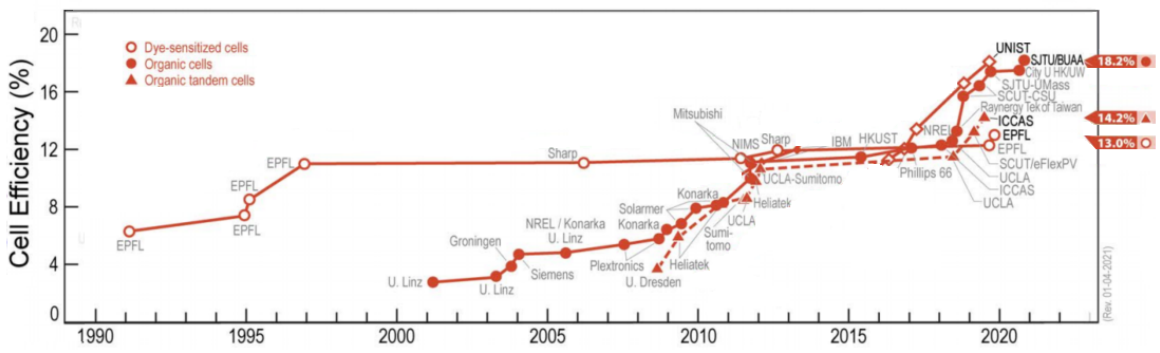


Fig. 1.16 Organic cells Efficiency by year.

Table 1.1 Solar Cell Efficiency (data of 2020).

Cell type	Efficiency (%)
Organic cells	17.5
Crystalline Si cells	27.6
single junction GaAs	30.5
Thin-film Technologies	23.4

Monolayer structure (Schottky type)

Also called Schottky structure, the mono-layer architecture is based on the principle of intercalation of an organic layer between two metal electrodes having different output works [96]. This organic layer is basically based on a conjugated polymer or a molecule (Fig. 1.17). It represents the first generation of organic photovoltaic devices [97]. In general, for the description of organic solar cells, metals are represented by their Fermi

levels. In contrast, semiconductors are represented by their valence and conduction bands, corresponding to the highest occupied molecular orbitals (HOMO) and the lowest unoccupied molecular orbitals (LUMO).

This structure has significant weaknesses for the intended application. The exciton created must be able to reach the metal / organic interface, which means that the thickness of the layer must not exceed the exciton diffusion length. This diffusion is between 5 and 20 nm in semiconductor polymers. Therefore these cells generally exhibit very limited absorption. The carriers' mobilities are generally low in such materials, which tends to increase the value of the Series resistance. Finally, the heterogeneity of the distribution of charge carriers and their accumulation at the interface is detrimental to the cells' overall performance [98, 99].

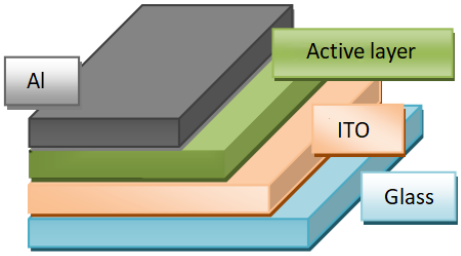


Fig. 1.17 Structure of a Schottky type cell.

Bilayer Structure (PN junction type)

Also called the P / N junction (Fig. 1.18), the bilayer system is made up of two different organic layers (donor and acceptor), which are deposited between two electrodes. The idea of replacing the Schottky structure with a bilayer structure came to extract the free charges efficiently. In most organic semiconductors, the photo-generated excitons are firmly bound (bond energy 0.2-1.0 eV) and, therefore, difficult to dissociate. The addition of the second layer generates an investment of all the materials, one with its ionization potential HOMO (donor) and the other with its electronic affinity LUMO (acceptor), thus promoting the dissociation of the excitons at their interface.

The D-A junction presents a system of π-conjugated electrons, contributing to the creation and transport of charges. Since the dissociation of the bonded electron-hole pairs occurs only at the D-A interface, the formed exciton must migrate to this interface in order to be able to dissociate and generate free charges. So the photoconversion is limited to a thin volume around the D-A interface. Layers with a thickness in the order of the diffusion length of the excitons (few tens of nm) are provided to improve the efficiency of the system.

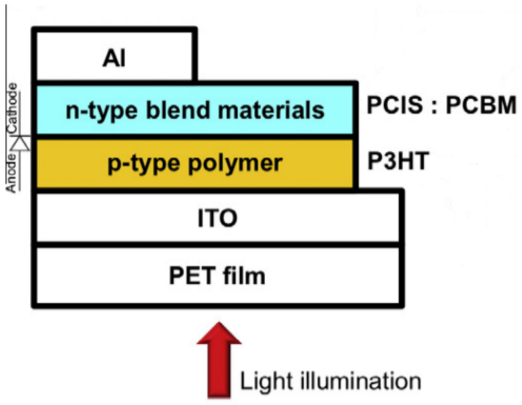


Fig. 1.18 Structure of a typical heterojunction device.

Hybrid Dye Sensitized Solar Cell

The dye-sensitized solar cell is named after its designer, Grätzel [100]. The absorption of photons and charge transfer within such a cell is different from those described above. The part that absorbs light is a dye called sensitizer S located at the interface between an n-type semiconductor (SC), mostly titanium dioxide TiO_2 and an electrolyte (redox system, usually I^{3-}/I^{-}). During photon absorption, the sensitizer changes from its ground state to the excited state ($S0 \rightarrow S^*$), which can inject an electron into the conduction band of the n-type SC. The injected electron passes through the SC layer to join the external circuit and generate a current. The sensitizer in the S^* form returns to its ground state through the hole/electron exchange with the redox system. The redox system then gives its charge to the counter-electrode, which makes it return to its ground state.

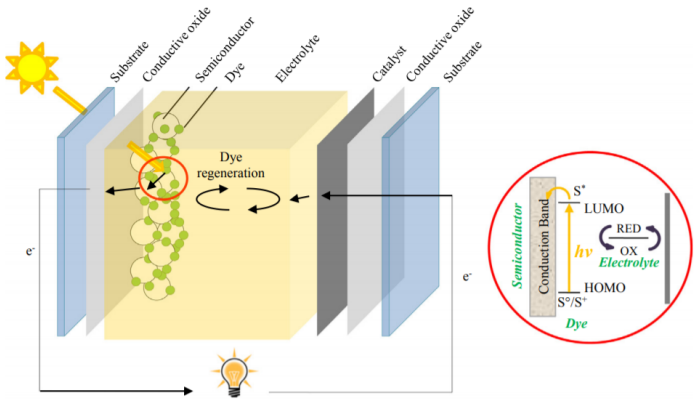


Fig. 1.19 DSSC structure and operational mechanism.

1.3 Conclusion

We have presented an overview of organic materials, in particular their types, their structure, and the evaluation of their performance. The specific optoelectronic properties of organic semiconductors (conjugated organic systems) make them the basis of new electronic devices. Electronic properties can be modulated by different approaches of molecular engineering. The steady and significant progress that has been recorded in recent years in this field is closely linked to the research and synthesis of new conjugate structures as semiconductor materials. Various examples of these structures have been reported in this chapter.

Chapter 2

Materials and Methods

The objective of this chapter is to present the theoretical and experimental methods used for the characterization that we have implemented in this work. We will thus describe the computational quantum mechanical modeling method illustrated in Density Functional Theory (DFT) to investigate the geometric and optoelectronic properties of the materials. Then a detailed description of the structural characterization methods (DRX, UV-Vis, SEM, and Impedance Spectroscopy), as well as their associated devices. These different techniques have allowed us to analyze the morphology and identify the crystallinity of the synthesized materials, optical, dielectric, and electric properties.

2.1 Materials

2.1.1 Structure of The Studied Materials

Several organic polymers have been studied regarding the materials used in this thesis, adopting computational and experimental approaches. One of the first organic material in question in this work is Polyppyrol, presented in Fig. 2.1. For the Polyppyrol systems, a computational study was applied to extract the geometric, electronic, and absorption properties, without any comparison with the experimental results.

The second one in Fig. 2.2 is selenophene as a pi-spacer material in which we have applied a computational study for comparison with the experimental results provided in a paper by [101]. In their paper, the approach focuses only on the donor. Nonetheless, it is possible to further improve the optoelectronic properties by changing the carbazol site with various types of electron donor sites; this was the main target in section 3.2.

While the previous two materials were only examined theoretically, the polymers PEcbz-Ter), (PEcbz-Ant), and (PEcbz-Fur) presented in Fig.2.3 were synthesized

and characterized by different techniques, alongside a theoretical approach to better understand their properties. An overview of the synthetic routes is given below.

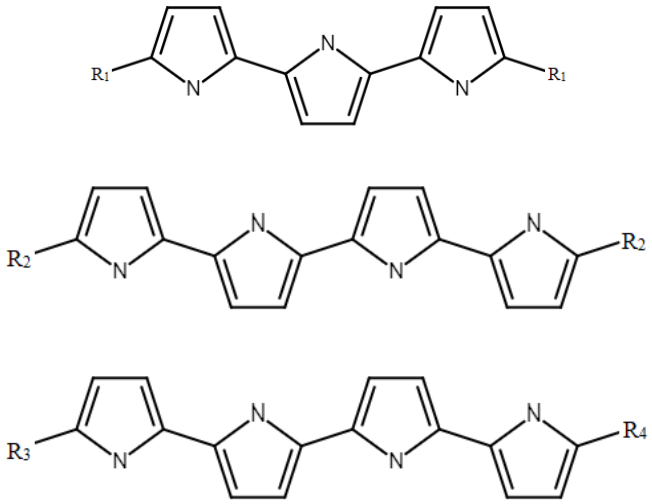


Fig. 2.1 Structures of the studied compounds. R1 = C_8H_{17}R2 = C_6H_{13}R3 = $C_{12}H_{25}$R4 = $C_{10}H_{17}$.

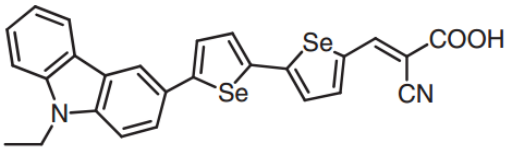
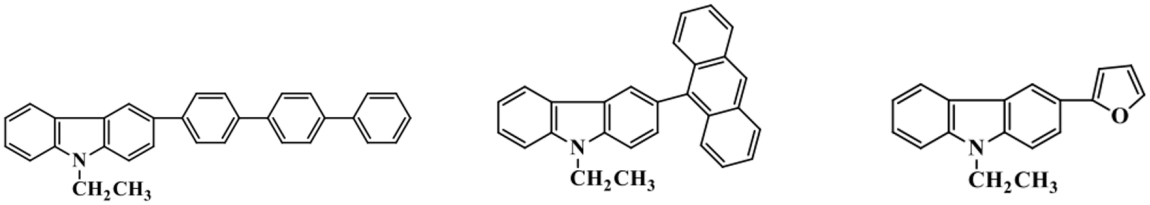


Fig. 2.2 Structures of MK-49.



(c) PEcbz-Ter (b) PEcbz-Ant (c) PEcbz-Fur

Fig. 2.3 Structures of PEcbz-Ter), (PEcbz-Ant) and (PEcbz-Fur).

2.1.2 Synthesis of Conjugated Polymers

We are more interested in the optoelectronic, dielectric, and electrical properties of organic polymers rather than the way they are made. However, in this section, a concise description of polymers' synthesis routes is presented to give a brief overview of how our materials were synthesized. Synthetic polymeric materials are obtained chemically or electrochemically [102, 103]. Synthesis methods are numerous, but they are generally based on two procedures: polycondensation and chain or radical polymerization.

Polycondensation Polycondensation is a simultaneous set of condensation reactions. The chain is formed during polycondensation by successive condensation, with the elimination of water. The reaction ends when there is no more monomer left. Polyamides, polyesters, and some polyurethanes are typical examples of polymers obtained by polycondensation. The polycondensation of Wittig obtained the first synthesis of poly (p-phenyl vinylene) (PPV) [104].

Radical Polymerization This type of polymerization is quite different from polycondensation: the polymer forms by the successive addition of free-radical building blocks without a simultaneous elimination reaction of water. Polymerization takes place in three phases [105–107]

(i) The initiation stage: this is the phase during which free radicals are obtained from the action of initiators, for example, FeCl3, followed by the addition of one of these free radicals to a monomer molecule to form an active center, the site on the chain carrier at which reaction occurs.

(ii) The propagation stage: this is an essential phase because it determines the macromolecule configuration and its molecular mass, during which the polymer chain grows by rapid sequential addition of monomer units to the active center.

(iii) The termination stage: this is the stage when the growth of the polymer is terminated.

Polymers' synthesis always leads to a mixture of macromolecules of different lengths, therefore different molar masses. The synthesis of polythiophenes by the Sugimoto method or by the $FeCl_3$ method [61] is a typical example of radical synthesis.

2.2 Methods

2.2.1 Theoretical Principles of Modeling

In materials science, quantum computing methods or electronic structure computations rely primarily on the resolution of the Schrödinger equation for the given system with the determination of the system's energy and wave functions. There are several methods of resolution, but they all go through various approximations and methods. These different methods are sufficiently developed in the literature; we will present the essential points of the density functional theory (DFT). The DFT methods allow calculations of electronic energy, optimized structures, frequencies of vibration modes, physical and chemical properties on relatively large molecules.

The quantum description of a molecular system is realized through the resolution of the Schrödinger equation [108]

$$\widehat{\mathrm{H}}\Psi(\vec{r},\mathrm{t}) = i\frac{\boldsymbol{\partial}\Psi(\vec{r},\mathrm{t})}{\boldsymbol{\partial t}} \tag{2.1}$$

Where H is the Hamiltonian operator of the system defined by

$$\widehat{\mathrm{H}} = -\mathrm{i}\frac{2m}{\nabla}^2 + V(\vec{r},\mathrm{t}) \tag{2.2}$$

The first term corresponds to the kinetic energy and the second to the potential $V(\vec{r},t)$ grouping the various interactions, m is the mass of the particle. The ultimate goal of most approaches in solid-state physics and quantum chemistry is the solution of the Schrodinger equation. The stationary Schrödinger equation for a molecular system consisting of N electrons and M nuclei is written.

$$\widehat{\mathrm{H}}\Psi_i\left(\vec{r}_1,\vec{r}_2,\ldots,\vec{r}_N,\vec{R}_1,\vec{R}_2,\ldots,\vec{R}_M\right) = \mathrm{E}_i\left(\vec{r}_1,\vec{r}_2,\ldots,\vec{r}_N,\vec{R}_1,\vec{R}_2,\ldots,\vec{R}_M\right) \tag{2.3}$$

H is the Hamiltonian operator for a system consisting of M nuclei and N electrons. The coordinates $\vec{r}_i$ regroup the space and spin variables of the electron i and the coordinates $\vec{R}_i$ of the nucleus k. As the energy E represented by the Hamiltonian $\widehat{\mathrm{H}}$, the superposition of the different energies put in place, we have:

$$\widehat{\mathrm{H}} = -\frac{1}{2}\sum_{i=1}^{N}\nabla_i^2 - \frac{1}{2}\sum_{K=1}^{M}\nabla^2\kappa - \sum_{i=1}^{N}\sum_{j=1}^{M}\frac{Z_K}{\mathrm{r}_{ik}} + \sum_{i=1}^{N}\sum_{j>1}^{N}\frac{1}{\mathrm{r}_{ij}} + \sum_{k=1}^{M}\sum_{l>k}^{M}\frac{Z_K Z_l}{\mathrm{r}_{kl}}$$

$$\widehat{\mathrm{H}} = \widehat{T}_e + \hat{T}_n + \hat{V}_{ne} + \hat{V}_{ee} + \hat{V}_{nn} \tag{2.4}$$

The first two T terms correspond to the kinetic energy operator of the electrons and nuclei, respectively. The following three terms represent the potential energy part of the Hamiltonian and represent the attractive electrostatic interaction between nuclei and electrons $\hat{V}_{ne}$ successively, then the repulsive potentials due to electron-electron interactions $\hat{V}_{ee}$ and nucleus-nucleus $\hat{V}_{nn}$.

According to Born-Oppenheimer approximation [109], the nuclei move much slower than the electrons due to their masses. We can consider the electrons moving in the field of fixed nuclei, so the nuclear kinetic energy is zero, and their potential energy is merely a constant. Thus, the electronic Hamiltonian reduces to

$$\widehat{\mathrm{H}}_e = -\frac{1}{2}\sum_{i=1}^{N}\nabla_i^2 - \sum_{i=1}^{N}\sum_{j=1}^{M}\frac{Z_K}{\mathrm{r}_{ik}} + \sum_{i=1}^{N}\sum_{j>1}^{N}\frac{1}{\mathrm{r}_{ij}} = \hat{T} + \hat{V}_{ne} + \hat{V}_{ee} \tag{2.5}$$

The solutions of the Schrödinger equation with $\widehat{\mathrm{H}}_e$ is electronic wave functions Ψ_e and the electronic energy E_e. Therefore, the total energy of the system will be the sum of this electronic energy with a constant nuclear repulsion term:

$$\widehat{\mathrm{H}}_e\Psi_e = \mathrm{E}_e\Psi_e \tag{2.6}$$

$$\mathrm{E}_{\mathrm{tot}} = \mathrm{E}_e + \mathrm{E}_n \tag{2.7}$$

2.2.1.1 Hartree-Fock Approximation

We have seen in the previous section; the central hypothesis used to describe a molecular system, which led to the Schrödinger equation. In this section, we will see how we can simplify this equation, which is way too hard to be solved in practice. A variety of approaches have been developed to obtain approximate solutions of Eq. 2.5. The oldest and most straightforward is the Hartree-Fock (HF) (or Self-Consistent Introduction Field) [110, 110] approximation, in which the ground state wavefunction $\Psi_e k = 0$ is assumed to be a determinant of single-particle states, a so-called Slater determinant [111, 112]

$$\Psi^{HF}(\{x_i\}) = \frac{1}{\sqrt{N!}} \begin{vmatrix} \Phi_i(x_i) & \Phi_j(x_i) & \cdots & \Phi_N(x_i) \\ \phi_i(x_j) & \phi_j(x_j) & \cdots & \Phi_N(x_j) \\ \vdots & \vdots & \ddots & \vdots \\ \phi_i(x_N) & \Phi_j(x_N) & \cdots & \Phi_N(x_N) \end{vmatrix}$$
$$= \frac{1}{\sqrt{N!}} \det[\Phi_i, \Phi_j, ., \Phi_N] \tag{2.8}$$

The N single-particle states Φ_i in the approximate ground state wavefunction Φ_{1_N} are determined variationally. For this purpose, the expectation value of the Hamiltonian is evaluated with respect to the wavefunction Φ_{1_N}. Assuming the single-particle states to be orthonormal, the result is

$$\begin{aligned} \mathrm{E}^{HF} &= \left\langle \Psi^{HF} \middle| \widehat{\mathrm{H}}_e \middle| \Psi^{HF} \right\rangle \\ &= \sum_{i=1}^{N} \int \Phi_i^*(x_i) \left[-\frac{\nabla_i^2}{2} + V^{ext}(x_i) \right] \Phi_i(x_i) \, \mathrm{d}x_i \\ &+ \frac{1}{2} \sum_{i=1}^{N} \sum_{j=1}^{M} \iint \Phi_i^*(x_i) \Phi_j^*(x_j) \frac{1}{|\mathrm{r}_i - \mathrm{r}_j|} \Phi_j(x_j) \Phi_i(x_i) \, \mathrm{d}x_i \mathrm{d}x_j \\ &+ \frac{1}{2} \sum_{i=1}^{N} \sum_{j=1}^{M} \iint \Phi_i^*(x_i) \Phi_j^*(x_j) \frac{1}{|\mathrm{r}_i - \mathrm{r}_j|} \Phi_j(x_j) \Phi_i(x_i) \, \mathrm{d}x_i \mathrm{d}x_j \end{aligned} \tag{2.9}$$

The above equation can be treated as an energy functional, $\mathrm{E}^{HF}[\{\Phi_i^*(x_i)\}, \{\Phi_i(x_i)\}]$, and this approximate ground state energy can be minimized with respect to the orbitals $\Phi_i(x_i)$, including the constraint of orthonormality. The constraint is implemented by the introduction of a suitable set of Lagrange multipliers in the functional to be minimized [113]. This leads to a mapping from a complex N-electron Schrödinger equation into effective one-electron Schrödinger-like equations:

$$\hat{F}_i \Phi_i(x_i) = \epsilon_i \Phi_i(x_i) \tag{2.10}$$

$$\hat{F}_i = -\frac{\nabla^2 i}{2} + V^{ext}(x_i) + V^{\mathrm{Hartree}}(x_i) + V_i^{\mathrm{Exchange}}(x_i) \tag{2.11}$$

$\hat{F}_i$ represents a one-electron Hamiltonian, known as the Fock operator [114]. ϵ_i and $\Phi_i(x_i)$ are the corresponding eigenvalues and eigenvectors, respectively. The first two terms are the kinetic energy and the total potential generated by the nuclei. The third and fourth terms approximately denote the electron-electron interaction. The contribution of the two-body interaction consists of a direct and an exchange term, as a consequence of the determinantal structure of the state. The HF equations have the structure of the ordinary single-particle Schrodinger equation. However, the total single-particle potential in the HF equations is nonlocal and contains two terms, the Hartree (direct Coulomb) potential.

$$V^{\text{Hartree}}(x_i) = \int \frac{n(x_j)}{|r_i - r_j|} \mathrm{d}x_j \quad n(x_j) = \sum_{j=1}^{N} |\Phi_j(x_j)|^2 \tag{2.12}$$

and the exchange potential

$$V_i^{Exchange}(x_i)\Phi_i(x_i) = \left[\sum_{j=1}^{N} \int \Phi_j^*(x_j) \frac{1}{|\mathrm{r}_i - \mathrm{r}_j|} \Phi_j(x_i) \mathrm{d}x_j\right] \Phi_i(x_j) \tag{2.13}$$

$V_i^{\text{Exchange}}(x_i)$ leads to an exchange of a variable in the two spin orbitals, as is evident from the above equation. In addition, the $V_i^{\text{Exchange}}(x_i)$ exchange operator is said to be a non-local operator because the results of $V_i^{\text{Exchange}}(x_i)$ operating on the $\Phi_i(x_i)$ spin orbital will depend on the value of $\Phi_i(x_i)$ throughout the entire space. Also worth mentioning is that the last two terms in Eq. 2.9 cancel each other when i= j, and thus the HF method is self-interaction-free by construction. Eq. 2.11 is the usual form of the HF equation, which is a problem of linear eigenvalue and must be solved self consistently. The HF method treats precisely the exchange interaction between electrons with the same spin and is often described as an exact exchange approach in the literature. The Hartree—Fock approach is a method that has been applied successfully to many areas of quantum mechanics, including atomic, molecular, and solid-state systems. The method is based on both the central field approximation and the variational principle.

2.2.1.2 Density Function Theory (DFT)

Density function theory (DFT) is a powerful tool to predict the optical and electronic properties of both inorganic and organic materials [115]. However, at the end of the

line, it is still necessary to synthesize the polymer to confirm the hypotheses. In terms of DFT, it is possible to simulate the characteristics of a considerable amount of polymers to provide reasonably reliable predictions. Thus, the properties of multiple polymers can be quickly understood without synthesis [116].

2.2.1.3 Thomas and Fermi Model

Thomas and Fermi considered a uniform gas of noninteracting electrons to derive a representation of the kinetic energy in terms of the density [117], using this functional with the actual inhomogeneous densities of systems like atoms or molecules (rather than just the uniform gas density). The conventional approaches use the wave function Ψ as the central quantity since Ψ contains the full information of a system. However, Ψ is a very complicated quantity that cannot be probed experimentally, and that depends on 4N variables, N being the number of electrons. Based on the uniform electron gas, Thomas and Fermi proposed the following functional for the kinetic energy.

$$T[n] = C_F \int n^{\frac{5}{3}}(r)dr, C_F = \frac{3}{10}\left(2pi^2\right)^{\frac{2}{3}} = 2.871 \tag{2.14}$$

The energy of atom is obtained using the classical expression for the nuclear-nuclear potential and electron-electron potential

$$E[n] = C_F \int n^{\frac{5}{3}}(r)dr - Z\int \frac{n(r)}{r}dr + \frac{1}{2}\iint \frac{n(r_1)\,n(r_2)}{|r_1 - r_2|} \tag{2.15}$$

The energy is entirely given in terms of electron density. In order to determine the correct density to be included in Eq. 2.15 above, they employed a variational principle. They assumed that the ground state of the system is connected to $n(x_j)$ for which the energy is minimized under the constraint of $\int n(x_j)\,dr = N$.

2.2.1.4 Hohenberg-Kohn Theorem

Even though nuclei and electrons can be decoupled, it is necessary to solve the Schrödinger equation applied to hundreds or even thousands of atoms. The first step towards this resolution was described with Thomas and Fermi, as we discussed in the previous section when they showed that the energy of a homogeneous gas of electrons is a function of its electron density. The idea of Hohenberg and Kohn in 1964 [118], was formulated in their paper as an exact theory for all many-body systems interact in

an external time-independent potential v(r). This theory is based on the two theorems of Hohenberg and Kohn, which were later generalities by Levy and Lieb.

(i) In a system of particles interact in an external potential v(r). This potential is determined, with a constant, only by n(r), the electronic density of fundamental state.

(ii) The ground state electron density can be found by using a variational principle.

The bijective relationship, established by the first theorem, between the electron density of the ground state and the external potential implies that all observables of the system are determined by $n(r)$, that is, each observable can be described by a $n(r)$ functional. Indeed, $n(r)$ can determine $v(r)$ to a constant, which means that the position of nuclei in a condensed system can be established from $n(r)$. The Hamiltonian is then completely known, and the resolution of the Schroedinger equation allows the evaluation of the total wave functions of the ground state and the excited states of the system, thus evaluating all observables. However, this theorem does not establish any direct relationship between the electron density and the properties of the system, so the initial problem of N-electrons interacting in a potential remains present.

$$\begin{aligned} E_0 < \left\langle \Psi' \middle| \widehat{\mathrm{H}} \middle| \Psi' \right\rangle &= \left\langle \Psi' \middle| \widehat{\mathrm{H}}' \middle| \Psi' \right\rangle + \left\langle \Psi' \middle| \widehat{\mathrm{H}} - \widehat{\mathrm{H}}' \middle| \Psi' \right\rangle \\ &= E_0' + \int n(r) \left[v(r) - v'(r) \right] dr \end{aligned} \tag{2.16}$$

where E_0 and E_0' are the ground-state energies for $\widehat{\mathrm{H}}$ and $\widehat{\mathrm{H}}'$, respectively. Similarly, we can get

$$\begin{aligned} E_0' < \left\langle \Psi \middle| \widehat{\mathrm{H}}' \middle| \Psi \right\rangle &= \left\langle \Psi \middle| \widehat{\mathrm{H}}' \middle| \Psi \right\rangle + \left\langle \Psi \middle| \widehat{\mathrm{H}}' - \widehat{\mathrm{H}} \middle| \Psi \right\rangle \\ &= E_0 - \int n(r) \left[v(r) - v'(r) \right] dr \end{aligned} \tag{2.17}$$

Adding Eq. 2.16 and Eq. 2.17 we would obtain, $E_0 + E_0' < E_0' + E_0$, which is a contradiction. So there cannot be two different external potentials that can give the same $n(r)$. Thus, $n(r)$ uniquely determines N and $v(r)$ and hence all ground-state properties. Now for a given $v(r)$ we can write the energy E_v explicitly as a function of the electron density $n(r)$:

$$\begin{aligned} E_v[n] &= \mathrm{T}[n] + V_{ne}[n] + V_{ee}[n] \\ &= \int n(r)v(r)dr + F_{HK}[n] \end{aligned} \tag{2.18}$$

where

$$F_{HK}[n] = \mathrm{T}[n] + V_{ee}[n]$$

Here note that $F_{HK}[n]$ is only dependent on $n(r)$ and independent from any external potential $v(r)$. Thus $F_{HK}[n]$ is a universal functional of $n(r)$. The Hohenberg-Kohn variational theorem states that for a trial density $n(r)$, the energy functional $E_0[n_0]$ cannot be less than the true ground-state energy of the molecule. This is expressed as:

$$E_0[n_0] \leq E_v[n] \tag{2.19}$$

Following the first part of the theorem, suppose the ground state wave function is Ψ, and its related electron density is $n(r)$. Thus the $n(r)$ uniquely determines the external potential $v(r)$. If there is another wave function Ψ' with an arbitrary variation from Ψ and its electron density is $n(r)$, then we can obtain

$$\left\langle \Psi' | \widehat{\mathrm{H}} | \Psi' \right\rangle = \int n'(r)v(r)dr + F_{HK}\left[n'\right] = E\left[n'\right] \geq E[n] \tag{2.20}$$

So the energy will reach the minimum only when the electron density is the ground-state electron density.

2.2.1.5 The Kohn-Sham Equations

The theorems of Hohenberg and Kohn do not, on their own, solve the correlated many-Body Problem. It was then necessary to use the approach proposed by Kohn and Sham in 1965 [119] in order to exploit the theorems of Hohenberg and Kohn. This formulation of the DFT replaces the original n-electron interacting problem with an auxiliary problem of independent electrons that is simpler to solve. The energy functional in the Kohn and Sham approaches is expressed as:

$$E[n] = \int n(r)v(r)dr + T_s[n(r)] + E^{\mathrm{Hartree}}\left[n(r)\right] + E_{xc}[n(r)] \tag{2.21}$$

The sum of the three terms $T_s[n(r)], E^{\text{Hartree}}\,[n(r)]$ and $E_{xc}[n(r)]$ represents the functional $F_{HK}[n]$. The $T_s[n(r)]$ is the kinetic energy of non-interacting electrons, which can be defined in terms of Kohn-Sham (KS) orbitals Φ_i for each electron:

$$T_s[n(r)] = -\frac{1}{2}\sum_{i=1}^{N}\left\langle \Psi_i \left| \nabla^2 \right| \Psi_i \right\rangle \tag{2.22}$$

the electronic density for such system is:

$$n(r) = \textstyle\sum_{i=1}^{N} |\Phi_i|^2$$

$E^{\text{Hartree}}\,[n(r)]$ represent the Hartree energy:

$$E^{\text{Hartree}}\,[n(r)] = \frac{1}{2}\iint \frac{n(r)n\,(r')}{|r-r'|}drdr' \tag{2.23}$$

$E_{xc}[n(r)]$ is the exchange and correlation energy; it includes all the many-body quantum effects. A variation of the total energy with respect to $n(r)$ leads to the following expression for the effective potential:

$$\begin{aligned} V^{\text{eff}} &= \frac{\delta\left\{\int n(r)v(r)dr + E^{\text{Hartree}}\,[n(r)] + E_{xc}[n(r)]\right\}}{\delta n(r)} \\ &= v(r) + \int \frac{n\,(r')}{|r-r'|}dr' + v_{xc}(r) \end{aligned} \tag{2.24}$$

where v_{xc} is the exchange-correlation potential defined as:

$$v_{xc}(r) = \frac{\delta E_{xc}[n(r)]}{\delta n(r)} \tag{2.25}$$

The effective potential V^{eff} transforms the many-particle problem to a single particle formulation, expressed as:

$$\left[-\frac{1}{2}\nabla^2 + V^{\text{eff}}\right]\Phi_i = \epsilon_i\Phi_i \tag{2.26}$$

The $\epsilon_i s$ are the energies of the Kohn-Sham one-electron orbitals. This is a Hartree-Fock-like single-particle equation that needs to be solved iteratively. Finally, we obtain the following expression for the total energy:

$$E = \sum_{i=1}^{N} \epsilon_i - \frac{1}{2} \iint \frac{n(r)n(r')}{|r-r'|} dr dr' + E_{xc}[n] - \int v_{xc}(r) n(r) dr \tag{2.27}$$

2.2.1.6 Exchange-Correlation Functionals

As mentioned in the previous sections, the goal is to find the Schrodinger equation's ground-state energy, but this is extremely difficult because this is a many-body problem. The interesting results of Kohn, Hohenberg, and Sham discussed above, exhibit that the required ground state can be found by minimizing the energy of an energy functional and that this can be achieved by finding a self-consistent solution to a set of single-particle equations. The critical complication in this interesting formulation is that the exchange-correlation function remaining unknown within the Kohn–Sham equations and need to be specified.

The local-density Approximation (LDA) In this approximation, the exchange-correlation functional is considered to be totally local, and the exchange-correlation energy density at a point r is taken to be that of a uniform electron gas having the same electron density, i.e., ϵ_{xc}^{uni}. In uniform electronic gases, the exchange energy density has a simple exact analytical form while the correlation energy density is more complicated and generally obtained from analytical curves fitted to numerical data, which are calculated by quantum Monte-Carlo methods [120]. The exchange-correlation functional in the LDA approximation is given in equation:

$$E_{xc}^{LDA}[n] = \int n(r) \epsilon_{xc}^{uni}(n(r)) dr \tag{2.28}$$

The analytical expression for the exchange energy expressed as:

$$E_{xc}^{LDA}[n] = -\frac{3}{4} \left(\frac{3}{pi}\right)^{1/3} \int n^{4/3}(r) dr$$

The first approach to improve the LDA approximation is to add a gradient dependence of the electron density to the exchange-correlation energy density using the first-order expansions of the exchange-correlation energy [121]. However, this method generally leads to worse results than the LDA approximation, because the gradients of

electronic densities present in the materials are too large, limiting the validity of the expansions used. The exchange-correlation energy treatment from LDA approximation works relatively well for metals with highly uniform density and more unexpected cases such as materials with ion-covalent bonds or transition metals. On the other hand, it fails in systems characterized by electron densities strongly varying with r. When applied to the study of suitable molecules or materials, the LDA functional can generally provide a satisfactory agreement with experiment concerning structural and vibrational properties, dipole moments, elastic moduli, and phase stability.

The Generalized Gradient Approximation (GGA) The generalized gradient approximation (GGA) is a set of methods, such as the Becke [122], Perdew and Wang [123], Burke and Enzerhof functionals [124, 125], suggested to modify the exchange-correlation energy density behavior for large gradient values. The general form of the exchange-correlation functional in the GGA approximation is given in Eq. 2.29.

$$E_{xc}^{GGA}[n] = \int n(r)\epsilon_{xc}(n(r), \nabla n(r))dr \tag{2.29}$$

where $\epsilon_{xc}(n(r), \nabla n(r))$ represents the electron exchange-correlation energy in a mutual interaction electron system of a non-uniform density.

The advent of these GGA type functionals led to the extensive use of DFT within the community of chemists in the 1990s. The use of a GGA type functional significantly increases the precision of the calculations compared with the LDA description, particularly for the binding energy of the molecules. For example, the magnitude of the relative error in the atomization energy calculation is lowered to $3-7\%$ when a GGA type functional is used. In comparison, an LDA functional leads to overestimates of the order of $20-30\%$. GGA functionals tend to improve total energies, energy barriers, and the energy differences between two different structures, and to lengthen and relax the bonds. This last effect strongly corrects the result obtained at the LDA level. The GGA type functionals also provide a better description of equilibrium volumes, elastic moduli, and magnetic properties of the compounds compared with local density approximation calculations. On the other hand, due to its local character, the GGA fails to deal appropriately with systems characterized by Van der Waals interactions linked to long-range correlations [126].

The Hybrid Functionals A reformulation of the exchange-correlation functional has also made it possible to develop hybrid exchange-correlation functionals leading to

outstanding results compared to the energy of the systems. These functionals are based on the fact that the density of exchange-correlation energy can be formulated using the average of the exchange-correlation hole $\bar{n}_{xc}(\boldsymbol{r},\boldsymbol{r'})$. The new exchange-correlation functional is then given by (Eq. 2.30). The $\bar{n}_{xc}(\boldsymbol{r},\boldsymbol{r'})$ corresponds to the average value taken by the exchange-correlation hole, which is the lack in the electron density around an electron when the system changes from a regime of independent electrons to a regime of correlated n-electrons. This hole is caused by Pauli's exclusion [127] and by the electron-correlation-induced screening.

$$E_{xc}[n] = \frac{1}{2}\int d^3r n(\boldsymbol{r}) \int d^3r' \frac{\bar{n}_{xc}(\boldsymbol{r},\boldsymbol{r'})}{|\boldsymbol{r}-\boldsymbol{r'}|} \tag{2.30}$$

In the independent electron regime, the exchange-correlation hole is simply the exchange hole defined by the Hartree-Fock method from the wave functions. The different hybrid functionals seek to establish an approximate value for the exchange-correlation functional of equation Eq. 2.30, knowing that it must take a value between the Hartree-Fock exchange energy E_x^{HF}, and the energy of exchange-correlation of a correlated system, given for example by E_{xC}^{LDA} or E_{xc}^{GGA}. One of the most widely used hybrid functional is B3LYP defined in (Eq. 2.31), in this equation E_x^{B88} is the exchange functional formulated by Becke [158], and E_{xc}^{GGA} is the correlation functional formulated by Perdew and Wang. The coefficients a_0, a_x and a_c are empirically adjusted to reproduce the properties of reference molecular systems [128].

$$E_{xc}^{LDA} = E_{xc}^{LDA} + a_0\left(E_x^{HF} - E_x^{LDA}\right) + a_x E_{xc}^{B88} + a_c E_c^{PW91} \tag{2.31}$$

2.2.1.7 Basis Sets

Basis sets can be classified according to the type and number of atomic orbitals included in the calculation and by the way in which they are represented [129, 130]. The choice of a particular basis set for a certain problem reflects a trade-off between accuracy and computational cost. In general, minimum basis sets, including the minimum number of atomic orbitals necessary to accommodate the electrons of each atom and representing such orbitals through a single function (SO, GTO, or a fixed combination of GTOs), are computationally cheap but lead to poor quality results. Whenever possible, the results are improved by expanding the basis set through the inclusion of :

(i) more than one functional in the expansion of each atomic orbital

(ii) and some extra functional that improve the description of the bond directionality (polarization functions) and the lack of compactness of the charge distribution in anions (diffuse functions).

Although one could reduce the calculation time by describing different atoms with different basis sets depending on their chemical relevance for the process under study, this practice is rarely used for small- and medium-size molecules, as it tends to create artifacts.

2.2.2 Experimental Methods

2.2.2.1 X-Ray Diffraction

Principles

X-ray powder diffraction plays a critical role in material research and development. Among its applications are the identification of the morphological and structural information, like atomic crystal structure (positions and symmetry of the atoms in the unit cell), size and shape of the domain, identification of the crystalline phases, and quantitative determination of their weight fractions [131].

X-rays are electromagnetic waves, as are visible light, but with high energy, its wavelength is shorter than visible light, solely in the order of 0.1 nm. X-ray diffraction methods are based on the phenomenon of wave interferences Fig. 2.4. Two light waves with the same wavelength and traveling in the same direction interact with each other, their signal can be amplified if the waves are in alignment (constructive interference) or conversely, the waves are out of aliment the signal is canceled (destructive interference), depending on their phase difference. For constructive interference, the diffraction peaks are measured, recorded, and analyzed to calculate the desired set of crystal properties [132].

Several types of interactions can occur, leading to different absorption and scattering effects, which will not be treated here. The X-ray beams incident on a crystalline solid will be diffracted by the crystallographic planes. Incident waves, beam one and beam two, are deflected by two crystal planes (A and B). The diffracted intensities are recorded as a function of the scattering vector (or momentum transfer) q, associated with the scattering angle 2θ by the relation $q = (4\pi \sin\theta)/\lambda$ [132]. When coherently scattered X-rays from atoms in neighboring planes interfere with each other, Bragg's law holds:

$$n\lambda = 2d\sin\theta \text{ or } d = 2pi/q \tag{2.32}$$

Where θ is the complement of the angle of incidence and n is known as the order of the diffraction, d is the distance between the atomic planes (d-spacing) and λ is the wavelength. Important to mention that this is the key relation in relating the structure to the observed peaks in the diffraction pattern. Bragg's law applies to materials with repeating discrete reflections that occur from the crystallographic planes. In our study, we used semi-crystalline copolymers, however, the inverse relationship between the real space (d) and the reciprocal space (q) is often used to interpret the positions of diffuse halos present in amorphous materials in terms on interchain distances even if there are no clear crystallographic planes are present.

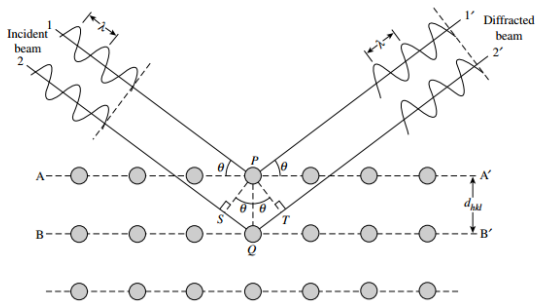


Fig. 2.4 X-ray diffraction principle.

Two in-phase incident waves, beam one and beam two, are deflected by two crystal planes (A' and B'). Then Bragg's Law can be calculated from the path differences between beam 1 and 2. The path difference depends on the incident angle (θ) and the spacing between the parallel crystal planes (d). The path difference ($SQ+QT = 2d\sin\theta$) of the beams has to equal one or multiple X-ray wavelengths ($n\lambda$) to keep them in phase.

In the X-ray diffraction analysis, two methods of XRD are common in practice the Laue method, in which θ is kept constant, and λ is varied; the second is the powder diffraction method, in which λ remains constant, and θ is varied. For both cases, the intensity of the diffracted X-ray beam is measured against the diffraction angle of 2θ, which gives the diffraction pattern of the material. For crystalline materials, the XRD pattern shows sharp maxima, called peaks, at their respective diffraction angle, whereas, for amorphous solids, the orderly structure is absent, such peaks are missing, and a broad maximum called a hump appears.

Within a crystal, the different crystallographic planes are defined by Miller indices (hkl). These are the three integers associated with the reciprocal values of the intersection between a given plane and the axes of the crystallographic unit cells. The diffraction pattern generates a sequence of spots if the irradiated substance is a single crystal. These diffraction spots turn into circles when the material is in the polycrystalline state.

Since polymers are neither fully crystalline nor entirely amorphous, the crystallinity is expressed in terms of a degree of crystallinity, which is a measure of the extent to which the material is crystalline. The total intensity is divided into two parts, the intensity of the diffracted beam from the crystalline part (I_c) and intensity of the diffracted beam from the amorphous part (I_a). The degree of crystallinity (Q) is determined by using the following expression :

$$Q = \frac{I_c}{(I_c + I_a)}$$

The knowledge and understanding of the degree of crystallinity in polymers are vital for predicting the properties and determining the application potential in various fields.

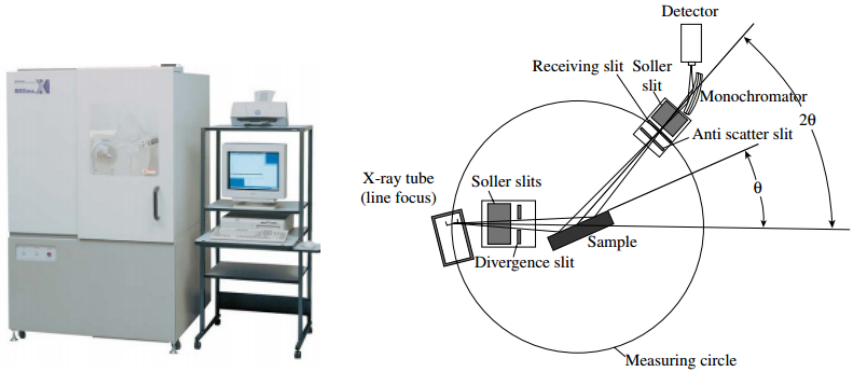
Instrumentation

The XRD instrument is called an X-ray diffractometer. There are a wide variety of types, configurations, and shapes of X-ray diffractometers, depending on the type of experiment being performed. The basic design of the diffractometer is illustrated in Fig. 2.5 a) demonstrates the geometrical arrangement of the three major components X-ray source, specimen, and detector [133].

X-ray tube, also known as the source, is what produces the X-ray radiation. This radiation passes through special slits that collimate the X-ray beam. These Soller slits, which consist of closely spaced, thin metal plates parallel to the plane of the diffractometer circle, are commonly used in the diffractometer. The purpose of Soller slits is to limit the axial (vertical / out-of-plane) divergence of the incident and diffracted X-ray beams. This improves peak shape and the resolution in 2θtype scans, especially at low scattering angles.

When the position of the X-ray source is fixed, and the detector is attached to the 2θ-axis, a divergent X-ray beam passing through the slits strikes the specimen. The specimen is usually in the flat-plate form that is supported by a specimen table. The convergent X-ray beam diffracted by the specimen reaches the receiving slits to the monochromator before being received by a detector. The monochromatic filter

removes every wavelength except Kα radiation and also decrease background radiation originating within the specimen. By synchronizing movements of diffractometer components, for which the X-ray source is at a fixed position while the sample and the detector are moving, we ensure the recording of diffraction intensity in a range of 2θ. Note that the θ-angle is the angle between the incident beam and the crystallographic plane that produces diffraction. Diffractometers can have numerous types of geometric arrangements depending on the scope of action targeted [134]. The microanalysis measurements were carried out with n Philips PW1800 diffractometer equipped with a curved detector (Kα ray of copper θ=1,5418 Å). In Fig. 2.5 a) an image of the XRD system that we have access to.



(a) (b)

Fig. 2.5 Shimadzu LabX XRD-6100 Diffractometer (Analysis Center, Faculty of Sciences Meknes (F.S.M)) b) Geometric arrangement of X-ray diffractometer

2.2.2.2 Absorption Spectroscopy

Basic Principles

Absorption spectroscopy uses electromagnetic radiation between 190 and 800 nm and is divided into the ultraviolet (190-400 nm) and visible (400-800 nm) regions. This technique is based on the interaction between light and matter when radiation from an external light source passes through a cell containing a dilute solution of the substance to be investigated. Other optical processes do or can occur, such as absorption, emission, or scattering of incident electromagnetic radiation [135].

The absorption of radiation in the ultraviolet-visible region leads to a transition among the molecule's electronic energy levels, and they are promoted to orbitals of higher energy levels. The difference between the energy levels of the two orbitals (excited state and ground state) corresponds to the energy of the absorbed light. Light source

creating a variety of wavelengths passes through the first slit of the monochromator, ensuring that all light photons travel along parallel pathways. Therefore, when they strike the prism, they are refracted into a rainbow of colors, so each wavelength of light moves to a different place in space. Only one wavelength of light in this situation is going to make it through the second slit in the monochromator, striking the beam splitter and becoming two beams of equal intensity [136]. These two beams will traverse two different cells, one being the reference (not containing a substance) and one being the sample cell. The purpose of using a reference cell is to eliminate the source of error that comes from the light loss through reflection at the cuvette surface as the beam exits these cells that strike the detectors, which are firing away, creating an electrical current and obtaining the spectral data.

The part of the molecule involved in the absorption processes is known as the chromophore. Different chromophores generate spectra called 'fingerprints,' enable us to identify and quantify specific molecules. These chromophores are the fundamental blocks of spectra associated with molecular structures and the transition types between molecular orbitals. Sigma (σ) bonding, pi (π) bonding and nonbonding (n) are the three types of ground-state molecular orbitals while (σ^*) and (π^*) antibonding state are two types of excited state from which transitions are observed in the UV region (Fig. 2.6).

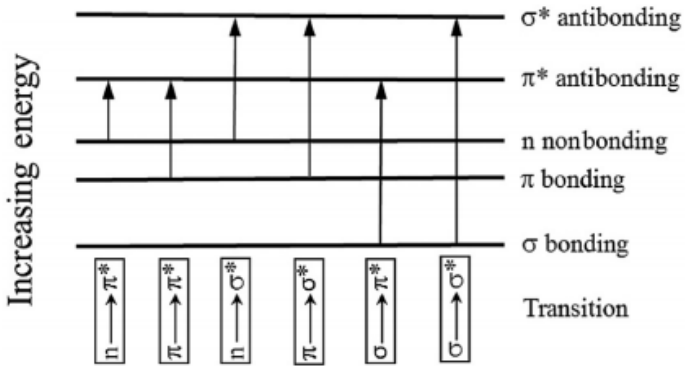


Fig. 2.6 Transitions between molecular orbitals.

Quantitative analysis based on UV-Vis spectroscopy is ultimately described by the Beer-Lambert law and is the correlation between the quantity of the incident light absorbed by the molecule, the sample, the light path length, and the concentration of the absorbing compound or molecule in the matrix [136].

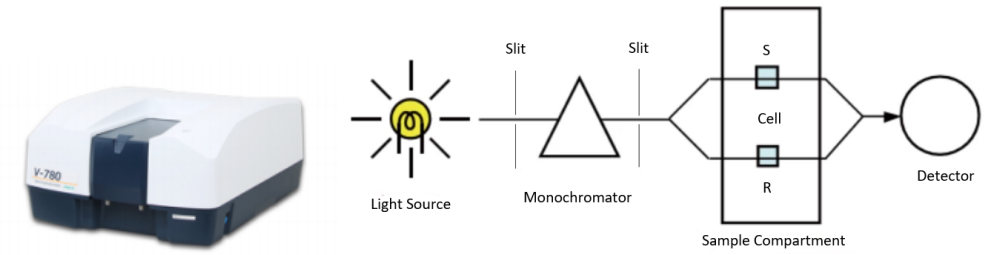
$$A = \log_{10} I_0/I = KbM/2.303 = \varepsilon\lambda bM \tag{2.33}$$

Where K/2.303 is the molar absorption coefficient or molar absorptivity, A the absorbance, hence, for a given wavelength and a single component, absorbance is a linear function of the concentration of that component. However, this equation is based on some assumptions, including radiation should be perfectly monochromatic, no uncompensated losses due to scattering or reflection, radiation beam strikes the cuvette at normal incidence, no molecular interactions between the absorber and other molecules in solution and temperature remains constant. Such assumptions are not always met in laboratories and might cause deviations from ideal Beer-Lambert law behavior.

Instrumentation

The Fig. 2.7 b) depicting a fairly, typical setup for a UV-VIS spectrophotometry. There are many different ways to build a spectrophotometer, but this is one of the simpler designs.

UV visible spectrophotometer consists of a stable source of radiant energy that generates a beam of radiation with sufficient power for easy detection and measurement. The next device in line is known as a monochromator, which is two slits separated by a prism or a diffraction grating, it splits lights into the various wavelengths of the incoming light in different directions. The next element of the spectrophotometer is the beam splitter, which divides a beam of light into two equal parallel beams of light. Next is the sample compartment that contains cells for both the reference and a sample, small rectangular plastic containers made of glass, or quartz. They are usually designed so that the light beam travels a distance of 1 cm through the contents. The sample cell includes a solution of the substance, while the reference cell contains the pure solvent. The last element in the spectrophotometer is the detectors, which convert photons' impact into electrical currents that can be monitored by a computer. Photomultipliers and silicon photodiodes are typical detectors used with spectrophotometers for the ultraviolet and visible regions [137]. Fig. 2.7 a) show the UV-VIS spectrophotometry we used for our copolymers.



(a) (b)

Fig. 2.7 a) JASCO V-570 spectrometer (LASMAR Laboratory, Faculty of Sciences Meknes (F.S.M)) b) Basic construction layout of a spectrophotometer

2.2.2.3 Scanning Electron Microscopy

Basic Principles

SEM is an advanced and versatile tool that is mainly used to observe the surface phenomena of materials. The sample is shot with a high energy electron in an SEM, and the resulting electrons / x-rays are analyzed. These outcoming electrons / x-rays provide information on the shape and size (topography), the surface features of an object (morphology), elements and compounds that constitute the material (composition), grain orientation, and the arrangement of atoms in the materials (crystallographic information) of a material.

The SEM instrument produces and emits primary electrons which are accelerated in the range of 1-40 keV [138] by heating or applying high energy. The electrons released from the source supply energy to the specimen's atomic electrons, which can then be released as secondary electrons, and an image can be formed from each point of the specimen by collecting these secondary electrons. Once the primary electron beam hits the sample surface, it will interact in many different ways with the near-surface area of the sample to a certain depth. There are substantial amounts of kinetic energy in the impinging electrons accelerated toward the specimens, which lose their energy inside the sample by generating several signals from electron-specimen interactions. Several factors influence the scattering process and the interaction volume, including the atomic number, concentration of atoms of the analyzed sample, the incoming electron energy and, the angle of incidence of the electron beam.

When the incident electrons are decelerated in the solid sample, Interactions of electron-sample will emit a variety of signals such as secondary electrons, backscattered electrons, photons (X-rays used for elemental analysis), and visible light (cathodoluminescence) [138, 139]. The signals are gathered by electron collectors (detectors), which

are then manipulated by the computer to form the required image. The backscattered and secondary electrons are commonly used for imaging sample creation. The secondary electrons are valuable for showing morphology and topography, and backscattered electrons are used to illustrate contrasts in the composition in multiphase samples. X-rays are generated by the inelastic collisions of the incident electrons with the electrons available in the orbitals of atoms in the sample. The electrons are then excited to higher energy levels; it emits x-rays when it returns to lower energy levels, having a fixed wavelength, based on the difference in the energy level of electrons in different elements. Thus, after the impinging of electron beams, each element produces a characteristic X-ray. SEM is a non-destructive technique, as the generation of X-rays does not result in any loss of specimen volume; the same material can therefore be analyzed repeatedly.

Instrumentation

SEM is an electronic and optical system which consists of the following components [140]:

(i) Electron gun

(ii) Vacuum

(iii) Column: condenser lens, scanning coil, objective lens, stigmator, sample holder and detector

In general, the electron gun fires an electron beam that follows a vertical path through electromagnetic fields and lenses in a vacuum. An objective lens focuses the electron beam down onto the specimen. Then the focussed beam scans over a specific area of the specimen surface. The scan pattern across the surface of the sample can be controlled with the help of deflector coils, which is controlled by the scan generator. The size of the raster pattern is controlled by magnification. The changes in magnification change the size of the rastered area on the sample. When the electron beam strike the sample target, this (electron-sample interaction) produces a huge number of signals, i.e. electrons and X-rays are emitted from the specimen. These signals are detected by the detector which is used to create magnified images, and collect other data produced from the signals Fig.2.8[140].

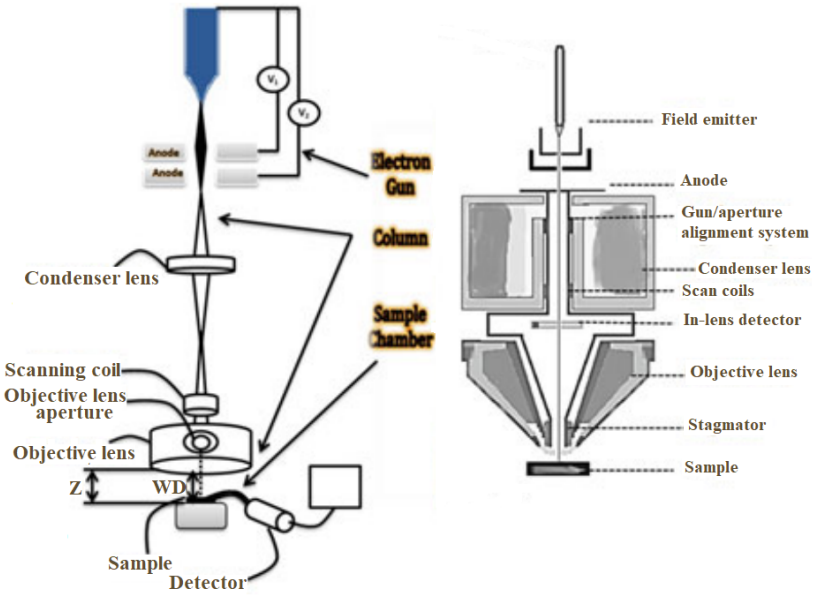


Fig. 2.8 Transitions between molecular orbitals.

2.2.2.4 Complex Impedance Spectroscopy

Basic Principles

Different techniques can be used to measure the dielectric constant of materials. One of them is the cavity perturbation technique [141], where electromagnetic waves frequencies (microwaves) were used; another technique is the ellipsometry [142], which depends on Maxwell's equations. One of the most convenient methods is the parallel plate capacitor [143] that has been used in this work. In general, the sample should be placed in an oven with controlled temperature (between ambient and 120° C) with a low level of excitation (1V) applied. The studied system is a plane capacitor, with the capacitance C and the dielectric constant ε_σ, in parallel with an ohmic conductor. The dielectric characterization of the sample involves two main steps:

(i) Variation of dielectric constant as a function of the frequency for different temperature ($\varepsilon_r = \mathrm{F(f)}$).

(ii) Variation of dielectric loss as a function of temperature for different frequencies ($\varepsilon_\mathrm{r} = \mathrm{F(T)}$).

The complex impedance measurements consist in applying a disturbance of low amplitude and frequency to a sample shaped in the form of a pellet. The corresponding current flowing in the sample is then recorded. Therefore the real $Z0$ and imaginary Z

components of the impedance can be deduced from it as a function of the frequency of the imposed alternating current.

The response to this perturbation is presented graphically. The impedance is most often represented in the form of a diagram: $Z" = f(Z0)$,, which shows loops and arcs of circles from the coordinates Cartesians. Other diagrams such as Bode diagrams show the polar coordinates of the impedance, modulus $|Z|$, and the phase, as a function of the frequency. Each point in the diagram corresponds to a given frequency of the input signal.

Polarization Polarization is the result of the distribution mechanisms of charges under the influence of an electric field. In the case of an object exposed to an electric field E, the relationship between P and E can be considered as linear:

$$P = \chi \varepsilon_0 E \tag{2.34}$$

Where χ is the dielectric susceptibility of the material and $\varepsilon_0 = 8.85 \times 10^{-12}$F/m the permittivity of free space. The dielectric susceptibility is related to the relative permittivity by the relation:

$$\chi - 1 = \varepsilon_{\mathrm{r}} \tag{2.35}$$

Where ε_{r} is the relative permittivity. there are different types of polarization depending on the polar or apolar nature of the material and the frequency of the field in which it is applied.

Mechanism of Polarization Generally, there are four types of polarization; electronic, atomic, orientation, and interfacial [144]. Electronic polarization: it corresponds to the deformation of the electronic cloud under an electric field. It can be observed up to frequencies of the order of 10^{15}Hz.

Atomic polarization: In the case where a covalent bond links two different atoms, the bonding electrons will be slightly displaced towards the most electronegative atom. A binding induced dipole moment was thus created. When an electric field applied to the induced dipole moment, the atoms move relative to each other, giving rise to an atomic polarization. Since atoms are much heavier than electrons, atomic polarization

stops at lower frequencies than electron polarization. The frequency limit of the atomic excitation is about 10^{12}Hz.

Orientation polarization: it operates for molecules having a permanent dipole moment. This type of molecule will orient itself in the direction of the applied field. Since orientation polarization requires a permanent dipole moment, it only concerns polar polymers. The orientation polarization gives the polymer relatively high relative permittivity values: $\varepsilon' = 4$ to 10 (poly (vinylidene fluoride)). It also causes a strong variation of the dielectric constant as a function of temperature, since the orientation capacity is related to viscosity. Finally, orientation polarization is often accompanied by a significant loss angle $\left(10^{-3} \text{ to } 10^{-2}\right)$ and vanishes at frequencies above 10^5Hz.

Interfacial polarization or space charge polarization: This type of polarization occurs when the polymer has several phases of different permittivities and conductivities. This heterogeneous material will have electric charges at its interfaces when subjected to an electric field. This type of polarization exists at low frequencies $\left(10^{-1} \text{ to } 10^2\text{Hz}\right)$. Eournié and Coelho add the ionic polarization to these principal polarizations, which results from the vibration under the effect of the field of resident ions within the polymer.

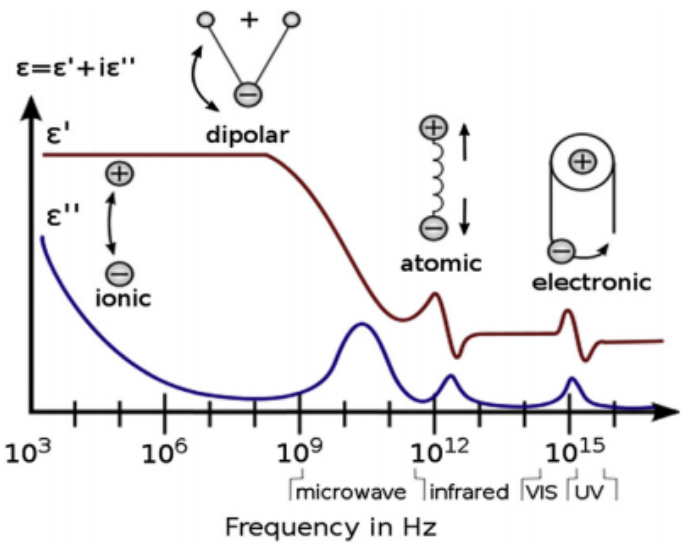


Fig. 2.9 Polarization levels.

Debye polarization has an important influence on the dielectric character of polymers. Their polarity is related to their permittivity and chemical structure. Therefore, a distinction is made between polar and apolar polymers.

- Apolar polymers are perfect insulators and have a low loss index of the order of 10^{-3} to 10^{-4} and almost constant permittivity (2.5 to 3). From a chemical point of view, they contain mainly carbons and hydrogens. If they have electronegative atoms, they are placed symmetrically along the carbon chain.
- Polar polymers have larger permittivities (3.5 to 10) and a high loss index $\left(10^{-2}\right.$ to 10). These polymers consist of electronegative groups (oxygen, chlorine, fluorine) placed asymmetrically along the carbon chain.

Dielectric Constant

The dielectric study is a physical model focusing on the interaction between the electric field and the atoms/molecules of the material. This model can be illustrated by the example of a planar capacitor (Fig. 2.10). The capacitor is made of 2 close metallic plates of a surface A, separated by the distance d. The plates accumulate electric charges when connected to a power source. One plate accumulates positive charge +Q, and the other plate accumulates negative charge -Q. The capacitance (C) of the capacitor is equal to the electric charge (Q) divided by the voltage (V):

$$C_0 = Q/V \tag{2.36}$$

A uniform electric flux density D_0 resulting from the charge density is directly proportional to the applied electric field E:

$$D_0 = \varepsilon_0 E \tag{2.37}$$

since $E = V/d$ the formula 2.36 can be described as:

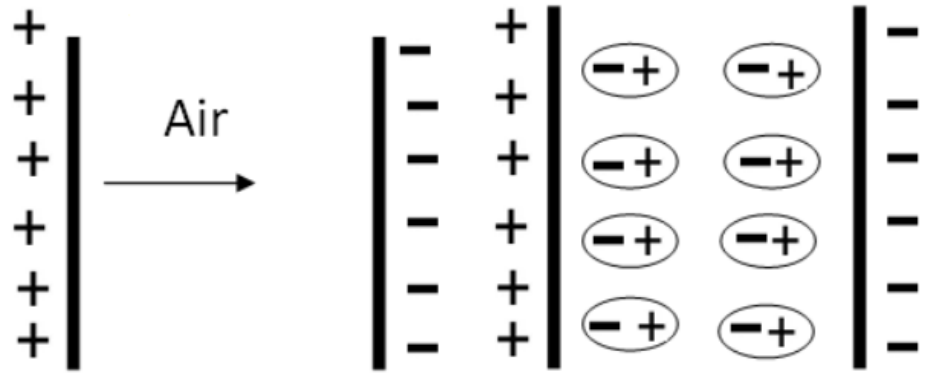
$$C_0 = \varepsilon_0 A/d \tag{2.38}$$

By replacing the empty space between the two electrodes with a dielectric material (Fig. 2.10 (b)), the total charge density at each electrode becomes $(Q + \mathrm{P})$, due to the dipoles polarization of the material. The capacity of the new system can be deduced from:

$$C = \frac{A(Q+P)}{V} = \frac{\varepsilon A}{d} \tag{2.39}$$

The increase in the total charge density will lead to an increase in the D flux density (or electrical displacement vector):

$$D = \varepsilon_0 E + P = \varepsilon E \tag{2.40}$$



(a) (b)

Fig. 2.10 Distribution of charges in a plane capacitor having (a) vacuum and (b) a dielectric material.

In a parallel plate capacitor with the presence of a sinusoidal electric field the current density passing through the dielectric material is [145]:

$$J(t) = \sigma E(t) + \partial D(t)/\partial t \tag{2.41}$$

using the Fourier transform, we will get:

$$\begin{aligned} J(\omega) &= \sigma E(\omega) + j\omega D(\omega) \\ J(\omega) &= \left[\sigma + j\omega\varepsilon_0 \left(1 + \chi'(\omega) - j\chi''(\omega)\right)\right] E(\omega)) \end{aligned} \tag{2.42}$$

or

$$\varepsilon_0 \left(1 + \chi'(\omega) - j\chi''(\omega)\right) = \varepsilon'(\omega) - j\varepsilon''(\omega) = \varepsilon^*(\omega)$$

ω is the angular frequency. χ' and χ'' are the real and imaginary components of the electrical susceptibility of the medium. ε' and ε'' are the real and imaginary components of the complex electrical permittivity of the medium.

The complex relative permittivity is a frequency-dependent property; it reflects the interaction between the elementary electric dipoles of a material subjected to an electric field and may be expressed by:

$$\varepsilon^*(\omega) = \varepsilon'(\omega) - j\varepsilon''(\omega) \tag{2.43}$$

- $\varepsilon'(\omega)$ The real part of the complex permittivity, it represents the behaviour of the ideal capacitor.
- $\varepsilon''(\omega)$ the imaginary part of the complex permittivity, it reflects the losses in the dielectric due to all types of defects.

In general, in a material subjected to an alternating electric field, the polarization does not follow the field instantaneously, causing a delay during the dielectric relaxation, which induces a loss of energy. These losses are due to several factors such as absorption, diffusion, or both and due to the residual Ohmic conduction of the dielectric. The amount of energy loss compared to that stored in the material is expressed by the dissipation factor, which is related to the phase component that represents the current density J with the electric field E (Fig. 2.11). The complementary angle δ of the phase shift between the voltage applied to the dielectric and the resulting current is called the loss angle. The tangent of the loss angle (tans) is equal to the dissipation factor that is usually expressed as the quotient:

$$\tan\delta = \varepsilon''/\varepsilon' \tag{2.44}$$

This dissipation factor (or dielectric losses) presents the energy absorption by the material and shows the difference between this material and a perfect insulator.

Only a few articles deal with the dielectric properties of the conducting polymers, although the dielectric function $\varepsilon^*(\omega)$ can provide information about transport mechanism in the system [146–148]. The dielectric response is generally described by the complex permittivity, where real $\varepsilon'(\omega)$ and imaginary ε " (ω) components are the storage and loss of energy in each cycle of the applied electric field [149].

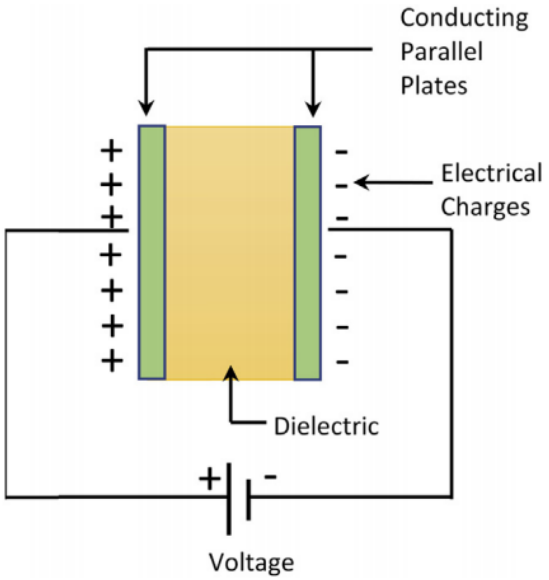


Fig. 2.11 Capacitor containing a material subjected to a sinusoidal electric field.

Mechanism of Electrical AC Conductivity

Several models have been proposed to describe the conduction mechanisms in conducting polymers. One of the models that describe the transportation of charge quantitatively within the conducting polymers is correlated barrier hopping (CBH); other models are not subject to discussion in this thesis.

In disorder or amorphous solids, the presence of a random structure causes localized states or clusters of disorders within the optical bandgap or mobility gap. The disordered solids usually have quite similar conductivity behavior, 'universality'.

In general, the dispersive nature of AC conductivity may be analyzed using the simplest description as proposed by Jonscher [150], the power-law frequency dependence.

$$\sigma(\omega) = \mathrm{A}'\omega^{\mathrm{s}} \tag{2.45}$$

Here A' is temperature-dependent or independent constant, and s is the power-law exponent, which describes the strength of the interaction between electrons within the material. Investigational outcomes reveal that power-law exponent (s) may depend upon temperature, which helps decide the types of AC conduction mechanisms.

The correlated barrier hopping model was developed by Pike (1972) [151] and later Long in 1982 [152], and Elliott in 1987 [153], to explain the AC conductivity in disordered or amorphous materials. The model is actually based on many assumptions.

In this model, the exponent (s) of the power-law decreases with increasing temperature, and the height of the potential barrier is correlated to the intersite separation. To that, it is known as the correlated barrier hopping (CBH) model.

In the CBH process, both single and pair of electrons can hop between neighboring sites over a potential barrier separating them. The jump probabilities per unit time are assumed symmetric, i.e., forward or backward jumps may take place between two localized sites. The hopping process of charge carriers occurs owing to thermal activation over the barrier separating the two different localized sites. The CBH model recognizes hopping of charge carriers between two sites over a barrier separating them instead of tunneling through the barrier, as described in many other models.

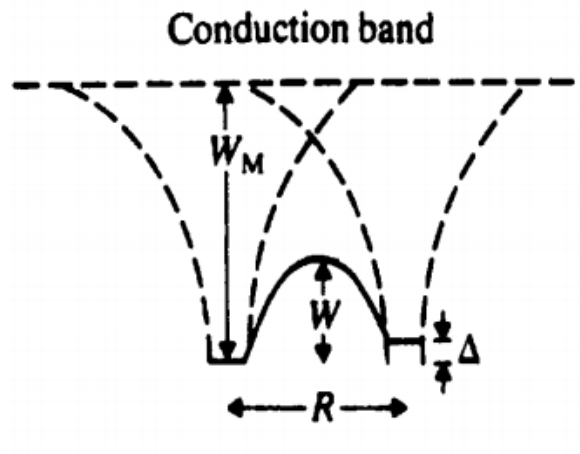


Fig. 2.12 Diagram of the potentials experienced by carriers which are separated by a distance R in CBH model.

Fig. 2.12 shows the nature of hopping, in which W_M represents the maximum barrier, experienced by a carrier, which is the difference in energy between E_c and the site energy. The dotted lines indicate the manner of variation of the potentials when the carrier is present in the two states, located at a distance R, and delta is the disorder energy. The full line indicates the variation of the effective barrier, W, and given by:

$$W = W_M - \frac{ne^2}{\pi\varepsilon\varepsilon_0 R_\omega} \tag{2.46}$$

where W_m is the maximum barrier height, e is the electron charge, n is the number of electrons involved in a hop, $n = 1$ for single-electron hopping, $n = 2$ for hopping of

two electrons and R_ω is the distance between two hopping sites (hopping length). In the CBH model, both R and w are treated as frequency-dependent. R_ω is given by:

$$R_\omega = \left(\frac{ne^2}{\pi\varepsilon\varepsilon_0 R}\right)\left[\frac{1}{\mathrm{W}_M - \mathrm{W}_\omega}\right] \tag{2.47}$$

The conductivity in the CBH model is proportional to $R_\omega^6.R_\omega^6$ is then expanded in terms of $\left(1/\mathrm{w}_\omega^6\right)(1/\omega\tau_0)\beta$ in order to arrive at a frequency exponent of ω. The exponent β is $(1-\mathrm{s})$ as

$$\beta = 6\mathrm{KT}/\mathrm{W}_M \tag{2.48}$$

Additionally, the power-law exponent (s) is $1-6\mathrm{KT}/\mathrm{W}_M$, temperature dependency, and it is perceptible that s decreases with a rise in temperature, which is the most commonly observed behavior of s. The localized states are responsible for the AC conduction process in consequence of their close interaction, thereby giving escalation to distribution of barrier heights separating them. Moreover, consistent with the CBH model, the AC conductivity can be represented as:

$$\sigma_{ac} = \eta\frac{\pi^3}{24}\mathrm{N}\varepsilon_r'.\varepsilon_0\omega R_w^6 \tag{2.49}$$

Here η is the number of polarons involved in the hopping process, N is the concentration of pair states, R_w^6 is the hopping distance at a frequency ω.

Instrumetation

The dielectric constant measurement system of the sweep frequency shown in Fig. 2.13 (b). The set of devices consisting mainly of an oven with controlled temperature and an LCR meter (Agilent E4980A) and a computer to monitor the data. The LCR meter is used to evaluate the impedance of components or materials under a wide frequency range (20Hz to 20MHz). The set is equipped with a temperature sensor linked to a computer to ensure automatic control of the system via a GPIB interface. The parallel-disk sample holder is usually shielded with metallic housing to prevent the leakage of electromagnetic fields Fig. 2.13 (a). These measurements are performed on materials that were grounded and pressed to form a disk-shaped pellet, both sides

are well polished to dryness and metalized by a thin layer of silver lacquer to form an ohmic contact.

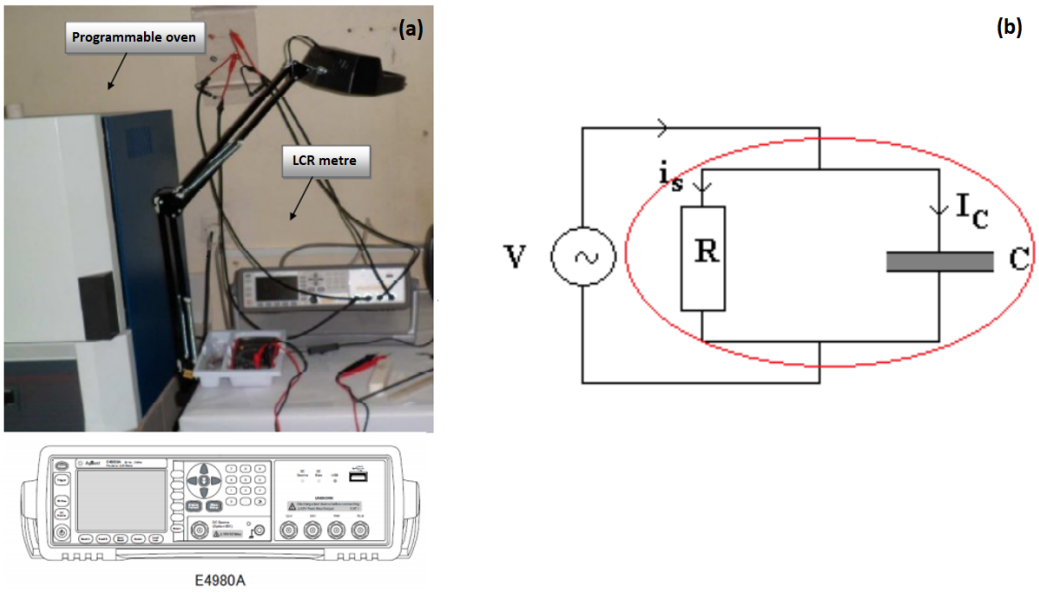


Fig. 2.13 (a) Equivalent diagram of the material studied reproducing a parallel ohmic conductor with a perfect capacitor, (b) Experimental device used for the dielectric study.

2.3 Conclusion

We have presented in this chapter the organic materials studied in this thesis with a brief description of some synthetic methods. Next, we covered the basic concepts of the theory behind computational calculations using Density Functional Theory (DFT). Subsequently, we explained the different characterization techniques used in this work as well as the associated experimental devices, recalling the basic principle of each technique and the corresponding measuring instrument. In each case, the experimental conditions and the factors related to the samples will be specified in chapter four where the analysis results will be provided.

Chapter 3

Theoretical Study of Organic Materials

This chapter will present a detailed computational study compared to experimental results of different organic materials used for various applications. The study is based on Density Functional Theory to extract the structural, electronic, and optoelectronic properties.

3.1 Alkyl-Substituted Oligopyrroles

3.1.1 Computational Details

The structures of the molecules 3,3'-dioctylterpyrrole (DOTP), 3,3'- dihexylquaterpyrrole (DH4P) and 3-3,7– dimethyldienyloctyl-3'dodecylquaterpyrrole (ddoD4P) were investigated at the density functional theory (DFT) methods under B3LYP [Becke 3-Parameter (Exchange), Lee, Yang and Parr] level of theory that known for being the best hybrid functional used for a wide range of organic molecules and have proven to be superior to many functional defined so far [154, 155]. All calculations were performed using DFT/B3LYP and $6-31G(d)$ basis set for neutral forms and unrestricted (UB3LYP) for the doped. We have studied the absorption by the Time Dependent Density Functional Theory TD-DFT which generates the transition energies and oscillator strength. The process was done using the gaussian09 [156] and the results were analyzed by using Gabedit [157] and Gauss view programs [158].

3.1.2 Geometric Parameters

Optimization allows to consider the most stable geometries especially that a conjugated molecule appears in several resonant forms, to examine the effect of the monomer length on the geometric parameters such as inter-ring distances, dihedral angles. Optimized structures of DOTP and DH4P and geometric parameters are given in Fig. 3.1 and Table 3.1 respectively. Since the length of the distances di (Å) and the dihedral angles θ_i provide information on the geometry of the carbon skeleton, we determined these two parameters from the optimized structures. The inter-ring distances of the DOTP is about $d_1 = 1.446$Å and $d_2 = 1.446$Å while in DH4P the distances are $d_1 = 1.445$Å, $d_2 = 1.444$Å and $d_3 = 1.445$Å. For the doped forms the distances are $d_1 = 1.412$ and d_2=1.412 in DOTP whereas in DH4P is about $d_1 = 1.420$Å, $d_2 = 1.412$Å and $d_3 = 1.420$Å, these decrease observed in doped form can be due to the quinoid form. A brief look at the values obtained we notice that the distances do not change significantly with the oligomer size, which can inform us about the geometry of the molecule of the parent polymer.

A calculation of the dihedral angles associated respectively with the DOTP and DH4P groups was carried out. The results show that the dihedral angles along the main chain are not modified and stabilized between 156° and 158° for the neutral forms and 179° for the doped, makes the last one better for the electrons delocalization.

Table 3.1 Inter-ring distances d_i(Å) and dihedral angles θ_i(deg) of DOTP, DH4P and ddoD4P obtained at B3LYP/6-31G(d) level of theory

Compounds	Form	θ_1	θ_2	θ_3	d_1	d_2	d_3
ddoD4P	Neutral	155.88	160.17	156.15	1.446	1.444	1.446
	Polaronic	178.14	-176.85	177.55	1.420	1.412	1.419
	Bipolaronic	178.50	-179.24	177.24	1.399	1.393	1.400
DH4P	Neutral	-157.76	-158.55	156.62	1.445	1.444	1.44
	Polaronic	179.99	-179.99	179.99	1.420	1.41	1.420
	Bipolaronic	179.32	-179.99	-179.34	1.394	1.387	1.394
DOTP	Neutral	157.98	155.61	–	1.446	1.446	–
	Polaronic	-179.92	-179.90	–	1.412	1.412	–
	Bipolaronic	178.48	-178.49	–	1.383	1.383	–

The investigation of the effect of the substituted alkyl in the DH4P and ddoD4P on the inter-ring distance of the ddoD4P is around 1.39Å to 1.44Å for the neutral and doped forms, compared with DH4P. It's clear that the alkyl group has no effect on the inter-cyclic distance. Whereas the effect appears on the dihedral angles, represented in

the enhancement of the planarity of the oligomers leading to improve the conductivity, it is more obvious in the doped form.

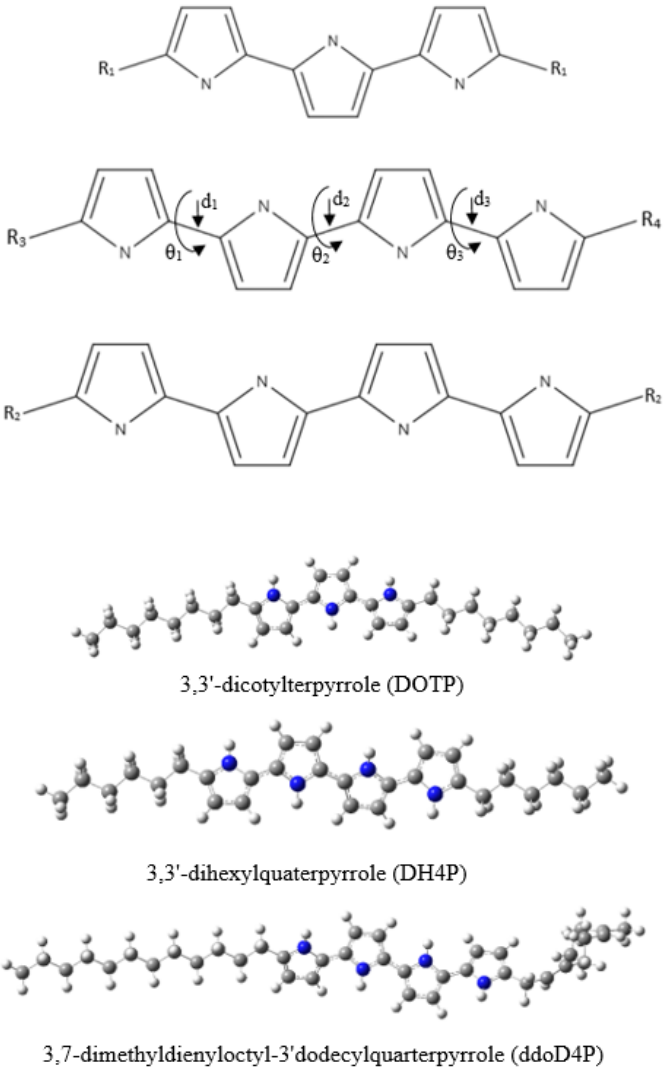


Fig. 3.1 Structures of the studied compounds and their optimization R1 = C_8H_{17}R2 = C_6H_{13}R3 = $C_{12}H_{25}$R4 = $C_{10}H_{17}$.

3.1.3 Electronic Proprieties

Theoretically, the energies of highest occupied molecular orbital HOMO and lowest unoccupied molecular orbital LUMO can be obtained by the DFT method. The gap between the two levels of HOMO and LUMO is used to estimate the gap energy. Table 3.2 summarizes the values of electronic parameters obtained for the studied

compounds. From the table the electronic parameters of ddoD4P and DH4P are not close, so it is noticeable that alkyl group R has an effect on the band gap especially in the doped forms. A change is observed for the HOMO and LUMO energies due to the substituent alkyl character. The comparison of the alkyl substitutions Suggests that the *pi* bond in R4 group leads to a change of the HOMO and LUMO levels and reduces the energy gap specially in the doped form (bipolaronic). The ionization potential (IP) and electron affinity (EA) of the molecules are also important in determining device performance in applications. As we know, the IP and EA are relevant to the ability of the electron injecting into the electrodes from HOMOs and the electron injecting into empty LUMOs from the electrode, respectively. The IP and EA values can be calculated by employing DFT and is estimated to be the negative of the HOMO and LUMO energies respectively (Koopmans theorem) [159], which are listed in table 3.2. The EAs of DH4P and ddoD4P are positive value, which suggests that they can act as an electron acceptor in the systems. Compared with DH4P, the low EA value of ddoD4P make it less suitable as electron accepting materials. A larger EA value indicates the electrons can be easily injected into the emitting materials from the electron transporting layer; and a smaller IP value suggests the holes can be easily injected into the emitting materials from the hole transporting layer [160]. The transition from DOTP to DH4P in the neutral and doped forms decrease the IP and Eg due to the increase in the extent of conjugation. This decrease can be illustrated by increasing the oligomer stability and improving conduction. Herein, the DH4P is more suitable for organic semiconductor than DOTP and ddoD4P.

Table 3.2 HOMO (eV), LUMO (eV) and E_{gap}(eV) values of the studied compounds.

Compounds	Form	LUMO	HOMO	Eg	IP	EA
ddoD4P	Neutral	-0.178	-4.108	3.930	4.108	0.178
	Polaronic	-4.013	-7.385	3.372	7.385	4.013
	Bipolaronic	-9.193	-9.642	0.448	9.642	9.193
DH4P	Neutral	-0.202	-4.095	3.893	4.095	0.202
	Polaronic	-4.065	-7.448	3.383	7.448	4.065
	Bipolaronic	-9.559	-11.192	1.632	11.192	9.559
DOTP	Neutral	0.046	-4.215	4.262	4.215	-0.046
	Polaronic	-4.306	-8.046	3.740	8.046	4.306
	Bipolaronic	-10.287	-11.333	1.045	11.333	10.287

3.1.4 Absorption Parameters

To refine the study, we used the time dependent density function theory (TD/DFT) to calculate the transition energies and oscillator strength. It is reported in the literature that TD/DFT provides the most credible results compared to other methods [161]. The obtained results showed that it is DH4P has the most important absorption wavelength, with a planar geometry compared with DOTP due to the increase in conjugation. It is obvious in Fig. 3.2 that the peak wavelength of DH4P tend to be shifted toward the long wavelength region (red-shift). On the other hand, the excitation energy, the wavelength and the oscillator strength of the studied compounds are determined and summarized in Table 3.3.

Table 3.3 Absorption data λ_{max}(nm), oscillator strength (f), Excitation energy (eV) obtained by TD-DFT method for the studied compounds.

Compounds	λ_{max}	f	E
ddoD4P	347.15	1.59	3.57
DH4P	349.22	1.49	3.55
DOTP	314.25	1.20	3.94

In order to study the impact of substitution on the absorption of the compounds ddoD4P and DH4P, the wavelength of maximum absorption (λ_{max}) and the oscillator strength (f) are shown in Table 3.3. These values were calculated from the optimized geometries using the Time Dependent DFT method. Absorption is represented by a vertically excited transition in an ascending sense from the ground state of the optimized structure to the excited one (S0 $\rightarrow$ S1) so that the electron jumps from the low energy orbital to the higher energy orbital. The maximum absorption is not significantly affected when passing from ddoD4P to DH4P which also can be noticed from the values in the table (ddoD4P = 347.15nm and DH4P = 349.22nm) with higher probability of absorption for ddoD4P [162]. In conclusion, care must be taken when designing a molecule using alkyl side chains because certain drawbacks of their use may be noticeable, in particular on the maximum absorption.

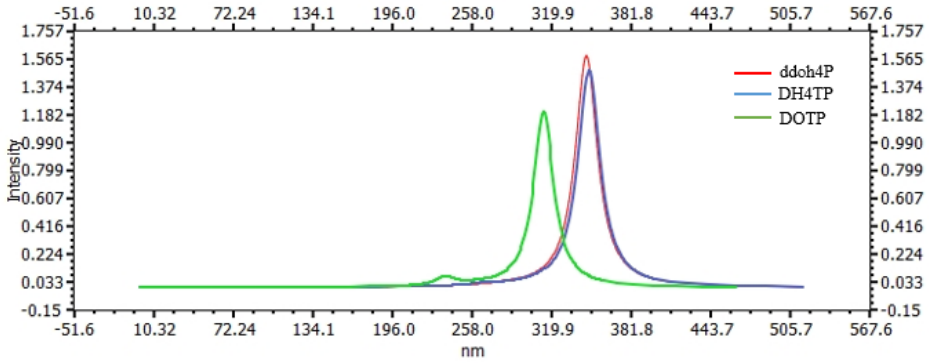


Fig. 3.2 Simulated UV-visible absorption spectra of studied compounds at theTD-DFT/CAM-B3LYP/6-31G (d) level.

3.2 Organic Dyes Based On Selenophene For Efficient Dye-sensitized Solar Cell

3.2.1 Parameter Estimation Equations

The power conversion efficiency (η) values of DSSCs is determined by the fraction of the open circuit potential (V_{oc}), short-circuit photocurrent density (J_{sc}) and the fill factor (FF) with the incident solar power (P_{inc})[163]:

$$\eta = \frac{FFV_{oc}J_{sc}}{P_{inc}} \tag{3.1}$$

For the short-circuit current density J_{sc} in DSSCs, can be determined following Eq. 3.2:

$$J_{sc} = \int LHE(\lambda)\Phi_{\text{inject}}\eta_{\text{collect}}\, d\lambda \tag{3.2}$$

Where $LHE(\lambda)$ is the light harvesting efficiency at a given wavelength, Φ_{inject} the electron injection efficiency, η_{collect} is the charge collection efficiency.

The light harvesting efficiency (LHE) is an important factor that affect the efficiency of DSSCs. Generally, maximum photocurrent can be achieved with large LHE. The following expression is used to calculate the LHE [164] :

$$\mathrm{LHE} = 1 - 10^{-f} \tag{3.3}$$

Where (f) represents the oscillator strength associated with the wavelength of maximum absorption of the molecule. Oscillator strength affects the LHE directly, the higher the value of (f), the greater the value of LHE. The injection driving force into the conduction band of the semiconductor surface (TiO_2) can be obtained using Eq. 3.4 [165]:

$$\Delta \mathrm{G}^{\mathrm{inject}} = \mathrm{E}^{\mathrm{dye}^*} - \mathrm{E}_{\mathrm{CB}} \tag{3.4}$$

Where $\mathrm{E}^{\mathrm{dye}^*}$ is the oxidation potential energy of the dye in the excited state and E_{CB} is the reduction potential of the con duction band of TiO_2. The value of E_{CB} is used in several previous works as -4.0eV [166, 167] and we adopted it in this thesis as well, while the $\mathrm{E}^{\mathrm{dye}\ ^*}$ can be expressed as [168–170] :

$$\mathrm{E}^{\mathrm{d}ye^*} = \mathrm{E}^{\mathrm{d}ye} - \mathrm{E}_{00} \tag{3.5}$$

where $\mathrm{E}^{\mathrm{dye}}$ is the oxidation potential energy of the dye in ground state, while E_{00} represents the absorption energy that corresponds to $\lambda_{\max}$. The V_{oc} can be approximately estimated by the analytical relationship [171]:

$$\mathrm{V}_{\mathrm{oc}} = \mathrm{E}_{\mathrm{LUMO}} - \mathrm{E}_{\mathrm{CB}} \tag{3.6}$$

Here, we evaluate the internal reorganization energy cost of the molecular geometry modifications when we go from the neutral to the ionized state and vice versa, including the hole and electron reorganization energy. The smaller the total value obtained, the faster charge-carrier transport rates will be [172]. The reorganization energy for the electron λ_e and hole λ_h of the materials have been predicted from the single point energy based on the optimized neutral, cationic, and anionic geometries. So, the reorganization energies for λ_e and λ_h transfer can be calculated following the equations :

$$\lambda_e = \left(E_0^- - E_-^-\right) + \left(E_-^0 - E_0^0\right) \tag{3.7}$$

$$\lambda_h = \left(E_0^+ - E_+^+\right) + \left(E_+^0 - E_0^0\right) \tag{3.8}$$

where $E_0^+\left(E_0^-\right)$ is the energy of the cation (anion) calculated with the optimized structure of the neutral molecule. Similarly, $E_+^+\left(E_-^-\right)$ is the energy of the cation (anion) calculated with the optimized cation (anion) structure, $E_+^0\left(E_-^0\right)$ is the energy of the neutral molecule calculated at the cationic (anionic) state. Finally, E_0^0 is the energy of the neutral molecule at the ground state.

The ionization potential(IP) and electron affinity (EA) are used to describe the energy barrier for hole and electron injection, which can be estimated by the following expression:

$$IP = E_{cation} - E_{neutral} \tag{3.9}$$

$$EA = E_{neutral} - E_{anion} \tag{3.10}$$

where $E_{neutral}, E_{cation}$, and E_{anion} are the total energies of the neutral, cationic, and anionic forms of the molecules at the B3LYP/6-311G(d,p) level, respectively.

3.2.2 Computational Details

Density functional theory method combined with B3LYP exchange-correlation function and 6-311G (d,p) basis set have been performed to fully optimized geometries of all compounds, and frequency calculation was done to ensure that the obtained confirmation is an energetic minimum of the simulated compounds without imaginary frequencies. This method is chosen because it gives reliable results in predicting molecular structures, very close to experimental values, and is commonly used for organic dyes by many previous researchers for the DSSC devices [173]. Frontier molecular orbitals (HOMO-LUMO) were estimated at the B3LYP/6-311G(d, p) level of theory. Photovoltaic properties were also calculated using the same combination.

Literature suggests that TD-DFT is efficient in estimating the excited state properties (such as oscillator strengths, vertical excitation energies, and maximum absorption

wavelengths) [174–177]. It is also believed that in the case of extended conjugated systems and charge transfer excitations, TDDFT generally shows significant effects. Hence, in order to have accurate descriptions of the UV–visible absorption spectra of the investigated compounds, four exchange-correlation (XC) functionals (W97XD, PBEPBE, CAM-B3LYP, and B3PW91) along with the 6-311G(d,p) basis set were adopted to calculate absorption spectra of reference dye D1. To simulate the environment of THF solvent, all calculations were done with the Integral Equation Formalism-Polarized Continuum Model (IEF-PCM) method to consist of experimentally reported in reference [101]. All calculations were performed using the Gaussian09 program package and Gaussview to visualize the obtained results.

3.2.3 The Choice of The XC Functional

To have reliable results, a series of primary computations were performed using different functionals to test the XC functionals and compare them with the available experimental data [101]. In particular, B3PW91, PBEPBE, CAM-B3LYP, and W97XD have been used in this regard. Table 3.4 shows the results of the four functional employed for the reference compound D1.

The PBEPBE has been reported in many articles to be the right choice for organic materials calculations [178–180]. However, As shown in Table 3.4, the performance of PBEPBE does not seem adequate for this dye compared with CAM-B3LYP and W97XD. CAM-B3LYP worked perfectly well for the studied compound and gave a fair value of the maximum absorption. The theoretical data were calculated with the solvation IEFPCM model imposed, where IEFPCM means that correction was included in the TD-DFT calculations but not in the geometry optimizations.

The functional CAM-B3LYP gives an absorption maximum of 452.5 nm, which is in good agreement with the experimental value, while B3PW91, W97XD gives poor results by predicting the maximum absorption, PBEPBE is much worse than all the functional employed. The performance of B3PW91, PBEPBE, B3LYP, and MPW1PW9 in predicting absorption and energies for the compound is not easy to explain. As it is known, both DFT and TD-DFT are theoretically regarded as methods based on “the first principle.” However, the energy functionals they employ do not have exact forms. Nearly all the XC functionals in practical use are some approximate expressions given by experimental data fitting. Thus, DFT and TD-DFT themselves must have a particular limitation in applications, somewhat like the semi-empirical quantum chemical methods. Generally, the theoretically predicted molecular properties results, except the equilibrium geometry, depend sensitively upon the chosen functional.

Overall, the CAM-B3LYP functional works efficiently, giving good results close to the experimental values, unlike the other functionals. For these reasons, all the calculations for all the systems considered in this study were calculated based on this functional.

Table 3.4 Absorption parameters λ_{max}(nm), Excitation energy (eV) and oscillator strength (f) of $MK-49$.

	λ_{max}	λ_{max} Exp.[101]	Exc. energy	f
Methods	solvent	Solvent	Solvent	Solvent
B3PW91	575.44	490	2.15	0.94
Cam-B3LYP	452.50	–	2.74	1.39
PBEPBE	767.41	–	1.61	0.49
W97XD	437.13	–	2.83	1.42

3.2.4 Geometry Structures

The optimized structures of the proposed organic dyes used in this work are shown in Fig. 3.3. All the molecular geometries have been calculated with the B3LYP/6-31G (d,p) level. The coplanarity conformation of dyes is an important factor that enhances electron transfer from donor fragments to acceptor moieties via the π-spacer unit. Table 3.5 presents the calculated critical bond length (d_1, d_2,and d_3) dihedral angels ($\Phi1$ and $\Phi2$, and $\Phi3$) in the ground state. We define $\Phi1$ as the dihedral angles between the donor and π-spacer, $\Phi2$ as the dihedral angle between π-spacer and the acceptor moiety (A), and d_3 and $\Phi3$ as the distance and dihedral angle between the selenophene cycles, respectively (Fig. 3.3).

As shown in table 3.5 the distance d_3 of all dyes is constant, meaning that changing the donor unit in the molecule chain has no effect on the linkage between the selenophene cycles. The distances d_1 of all dyes are in the range of 1.43–1.46 Å. The distance values in D1 and D6 between the donor and π-spacer are different from those of other structures. This could be due to phenyl rings in the donor group. Furthermore, all the distances are equal or less than 1.46 Å, showing a C-C character that favors the intramolecular charge transfer (ICT) between the donor and π-conjugated spacer. Oppositely the values of the distances d_2 between the π-spacer and acceptor of all dyes are equal to 1.45 Å. These values are lower than single C–C bonds (1.530 Å), which confirm the strong resonance structures between π-spacer and acceptor for all dyes.

The differences in dihedral angles between the units in dyes can affect the ICT. Therefore, it is advantageous to maintain the dihedral angle to the maximum to impart coplanarity of the dye. Since the studied dyes possess the same π-conjugated linker,

this suggests that the acceptor moieties and conjugated chain have the same dihedral angles Φ2 values. The dihedral angles between the acceptor moieties and π-spacer are equal to approximately 179° for all dyes. On the other hand, the angle between the donor and π-spacer is changing from 149° to 179°. The distortion of angles in D1 and D6 might not be beneficial for charge transfer between the donor and acceptor via the π-spacer. High dihedral angle results in a more planner backbone. When the 9-Vinylcarbazole unit is replaced by different donor types like compound D3, D4, D5, and D7, the dihedral values increased to 179°. Thus, the design of those dyes using these donors enhances the ICT from the electron-donor to the electron acceptor group.

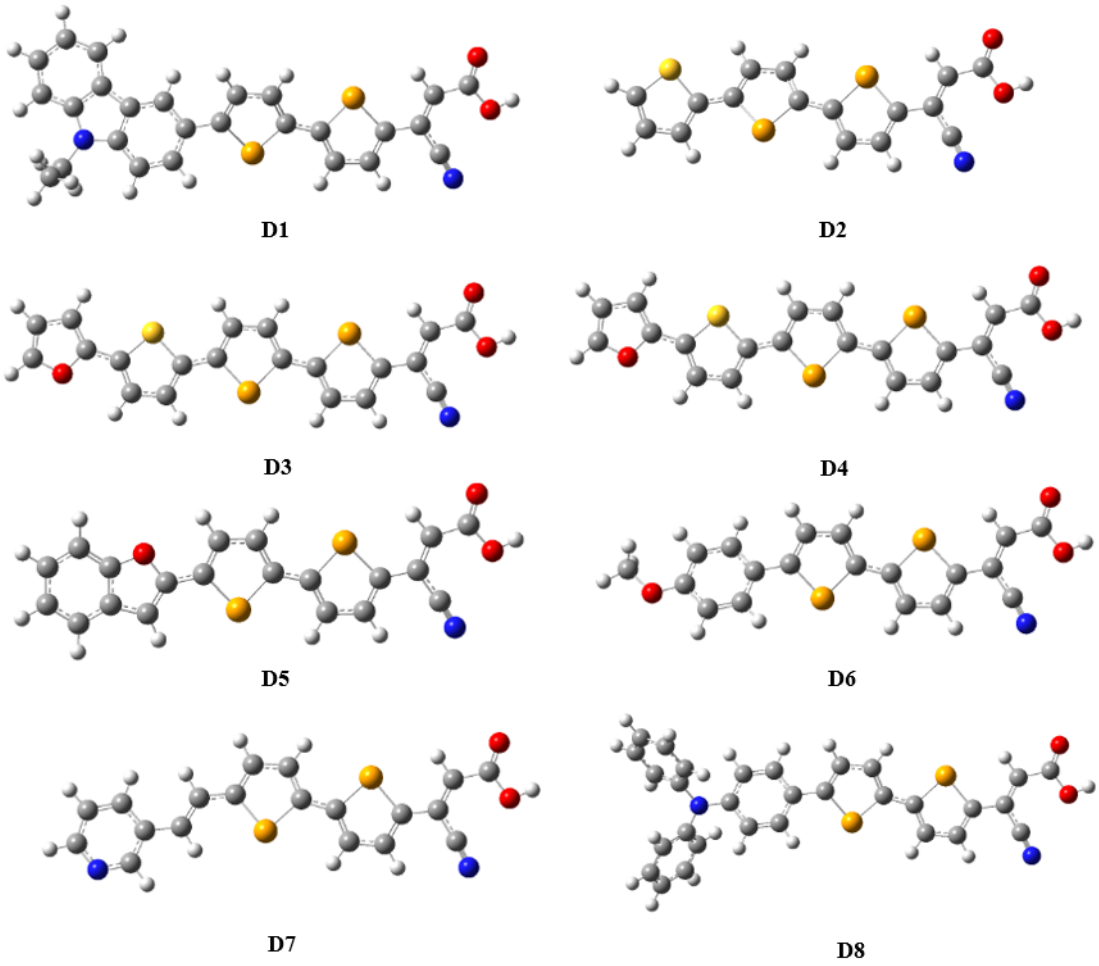


Fig. 3.3 Optimized structures of the studied compounds.

Table 3.5 Bond lengths (Å) Dihedral angles (Φ) Parameters of all dyes in the ground states.

	d_1	d_2	d_3	Φ1	Φ2	Φ3
D1	1.463	1.452	1.435	149.49	179.01	164.88
D2	1.444	1.454	1.435	156.76	178.27	163.41
D3	1.437	1.453	1.433	179.97	179.99	179.99
D4	1.441	1.454	1.434	179.98	179.99	179.97
D5	1.435	1.454	1.434	179.99	179.99	179.92
D6	1.462	1.453	1.435	149.12	178.30	163.36
D7	1.438	1.454	1.434	179.40	179.14	167.56
D8	1.459	1.452	1.435	152.60	178.60	164.20

3.2.5 Molecular Orbitals

The analysis of the energy levels of HOMO and LUMO with the related energy gap can give valuable information about the electronic proprieties of the dye structure. Donor fragments can influence electronic parameters. Therefore, a high HOMO presents a good electron-donating character of the donor moieties compared with a low HOMO. The studied compounds with different donor fragments have been investigated to see the effect of the electron-donating group on the electronic parameters.

Herein, we plotted the electron spatial distribution of HOMO and LUMO orbitals of all dyes in Fig. 3.5. In general, the plots of the HOMO and LUMO demonstrated the typical p-type molecular orbital characteristics. Moreover, the HOMO displays an antibonding character between two adjacent fragments and a bonding character within each unit. The LUMO exhibit the bonding character between the two adjacent fragments, so the lowest-lying singlet states correspond to the electronic transition of π-π^* type. As observed in Fig. 3.5, the pattern of the HOMOs and LUMOs are qualitatively similar to each other, respectively. The figure shows that the HOMO has strong contributions over the whole molecule and less on the electron acceptor (2-cyanoacrylic acid) fragments. While the LUMOs are essentially localized on conjugation spacer moiety and the acceptor fragments.

When HOMO-LUMO excitation is stimulated with light radiation, this stimulation caused the electron distribution to shift from the donor side to the left side of the molecule through the conjugated bridge. It may be noted that the photo-induced charge transfer from the anchoring group (-COOH) to the TiO_2 electrode could happen effectively by the HOMO-LUMO transition and thus improve the electron injection efficiency and subsequently enhance the short-circuit current density J_{sc}.

The values of the HOMO and LUMO and the energy gap are provided in Fig. 3.4. As we can notice the HOMO of these dyes are in order: D8 > D3 > D1 > D6 > D5 > D5 > D4 > D2 > D7 . The dye D3 and D8 with furylthiole and triphenylamine donor fragments possess the highest HOMO within the other compounds. While the donors in the D2 and D7 considered being weak donating due to the lowest HOMO values -5.834 eV and -5.855 eV, respectively. Regarding the LUMO of all dyes, as shown in Fig. 3.4, and despite the change in the dyes structures, it is obvious that the obtained values are quite identical. This is due to the acceptor group (2cyanoacrylic acid) present in all studied dyes. The LUMO energy levels obtained for all dyes are much higher than that of TiO_2 conduction band edge (4.0eV), which favors the injection of electrons into TiO_2 electrodes in the excited state. The HOMO energy levels are below the I^-/I_3^- electrolyte (4.8eV) Fig. 3.4. Thus, it permitted the dyes to restore electrons from the electrolyte, allowing the oxidized species to regenerate.

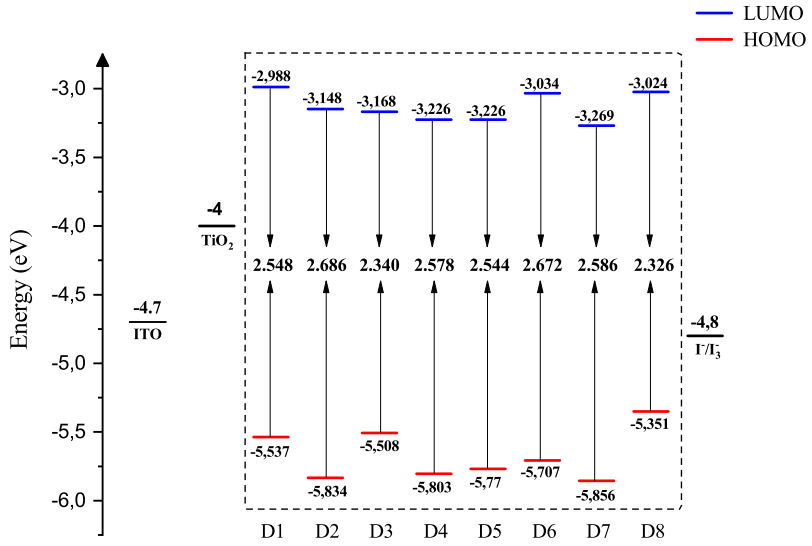


Fig. 3.4 Schematic energy diagram, TiO_2 and electrolyte $\left(I^-/I_3^-\right)$.

The energy gap can be calculated by the differences of HOMO and LUMO energy levels, and the results are shown in Fig. 3.4. The energy gap of all dyes is decreasing in the order: D8 < D3 < D5 < D1 < D4 < D7 < D6 < D2. The calculated E_g of all dyes is in the range of 2.32-2.68 eV, make these dyes suitable candidates for the DSSC application. It is found that using the furylthiole and triphenylamine as donor units in D3 and D8 gives the lowest energy gap, 2.32 eV and 2.33 eV, respectively. On the other hand, the E_g of D2 was found high at 2.68 eV than other dyes making the thiophene less effective in electron-donating ability in this set of structures.

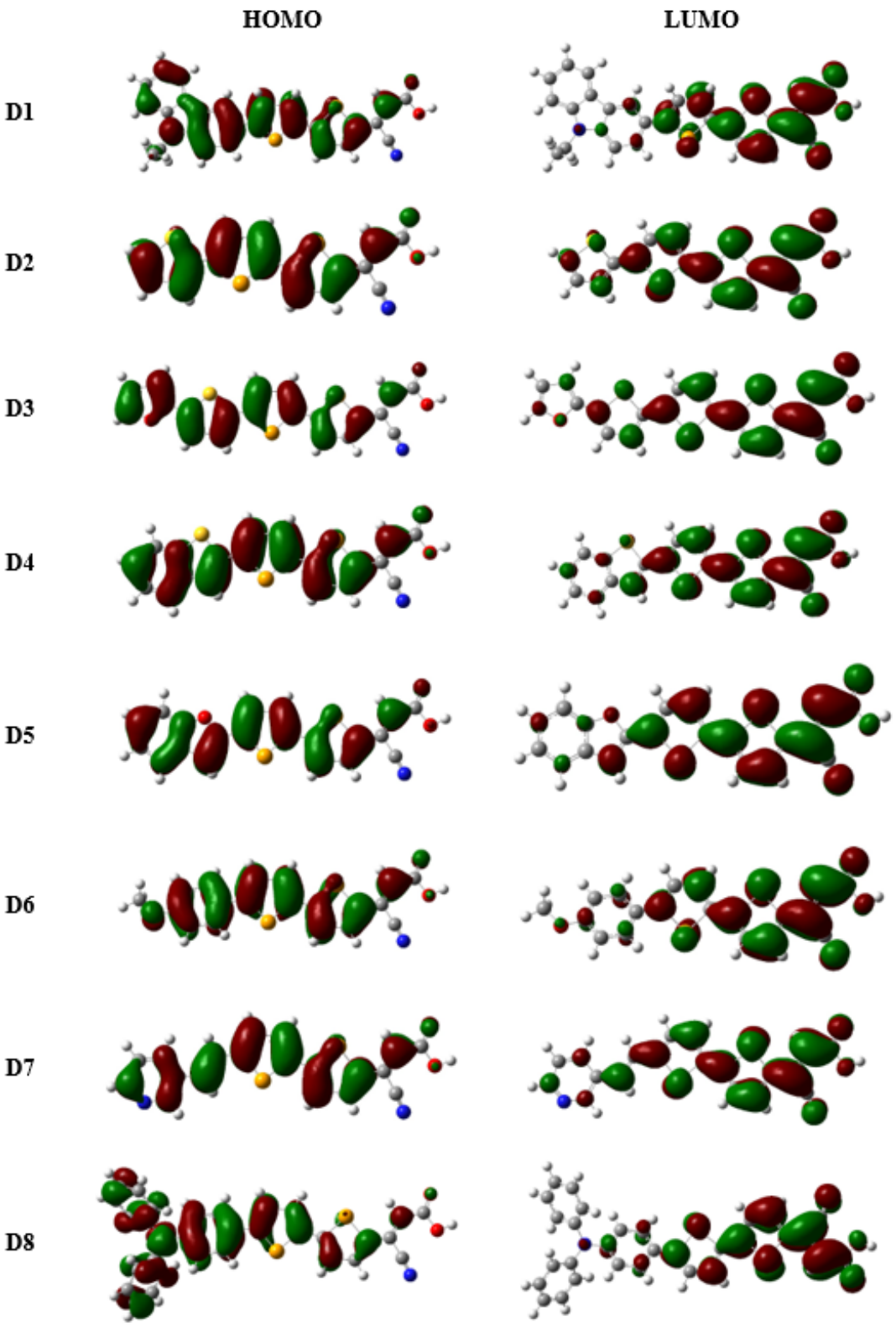


Fig. 3.5 Contour plots of the frontier orbitals of all dyes.

3.2.6 Photovoltaic Properties

In order to find the impact of the acceptor and different donor units on the efficiency of dyes, different photovoltaic parameters like light-harvesting efficiency (LHE), electronic injection driving force (ΔG^{inject}), and open-circuit voltage (V_{oc}), are calculated and presented in table 3.6. As discussed above and shown in Eq. 3.2, LHE and ΔG^{inject} are the essential factors that affect J_{sc}. The dye must possess a higher LHE value to absorb more photons in the UV-Visible region and inject a photoexcited electron into the conduction band. The dye must possess a higher LHE value to absorb more photons in the UV-Visible region and inject a photoexcited electron into the conduction band. LHE of investigated compounds are calculated using Eq. 3.3, and results are presented in Table 3.6 and (Fig 3.6 (a)). All dyes exhibit high LHE values and increase in the order D3 < D2 < D5 < D6 < D1 < D4 < D7 < D8. Among these dyes, dye with triphenylamine as a donor, namely D8 is having a higher LHE value of 0.965 and while dye D3 being the smallest LHE 0.925 (Fig 3.6 (a)). The LHE values for D4 < D7 < D8 are 0.952, 0.959, and 0.965, respectively, which implies that with the replacement of donors with triphenylamine fragment, the LHE value is increased. This could guarantee a better photocurrent response. Thus, it is confirmed that structural modeling by donor units affects the LHE values and would be an important strategy to enhance the LHE, hence DSSCs efficiency. The electronic injection driving force ΔG^{inject} calculated from Eq. Eq. 3.4 and results are tabulated in Table 3.6. For smooth injection of an electron from the LUMO of the dye compounds into the conduction band (TiO_2), the ΔG^{inject} value must be negative. The more negative value of ΔG^{inject} helps to increase J_{sc}. All the designed dyes show negative ΔG^{inject} values, showing a spontaneous electron injection from the dye to the TiO_2 conduction band. In all dyes, the molecule (D8) with triphenylamine as a donor has the most negative values of -1.33 while D7 exhibits the smallest value, which means that this dye D8 conducted to a faster and subsequently a higher J_{sc} value compared to other dyes. The open-circuit voltage (V_{oc}) delivers an idea about mobility and the number of charge carriers across the interface; high-value (V_{oc}) results in small loss due to charge recombination, and hence higher will be the efficiency of the cell. From the results recorded in Table 3.6, the calculated values of (V_{oc}) for the dyes are in the range of 0.73-1.01 eV. It is evident from Eq. 3.6, the higher energy of the LUMO level results in a higher Voc value. The decreasing order of the obtained V_{oc} of dyes is D1>D8>D6>D2>D3>D5>D4>D7. The dye D1 is with the highest V_{oc}, resulting in a higher J_{sc} value [181]. The dye with 9-Vinylcarbazole as a donor group shows a higher Voc value of 1.01 eV than other studied dyes with different donor groups. Changing the donor moieties in the

dye has a noticeable impact on the electrochemical parameters. Based on the results above, Dye D8 possesses large LHE, ΔG^{inject}, and V_{oc}, which could be beneficial for the performance of DSSCs.

Table 3.6 Calculated Electrochemical Parameters for all dyes.

	$\mathbf{V}_{\text{oc}}$	E^{dye}	$E^{\text{dye}*}$	ΔG^{inject}	LHE	λ_e	λ_h	λ_{tot}
D1	1.01	5.53	2.79	-1.20	0.94	0.32	0.31	0.64
D2	0.85	5.83	3.05	-0.94	0.92	0.33	0.34	0.68
D3	0.83	5.50	2.98	-1.01	0.95	0.27	0.25	0.53
D4	0.77	5.80	3.11	-0.88	0.95	0.29	0.26	0.55
D5	0.77	5.76	3.08	-0.91	0.92	0.29	0.25	0.55
D6	0.96	5.70	2.91	-1.08	0.95	0.42	0.38	0.81
D7	0.73	5.85	3.18	-0.81	0.96	0.31	0.27	0.59
D8	0.97	5.35	2.66	-1.33	0.92	0.41	0.24	0.66

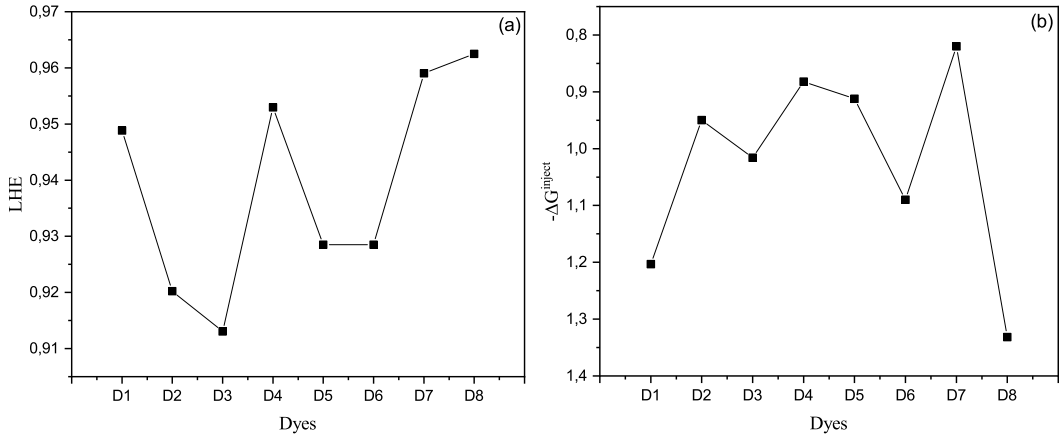


Fig. 3.6 Critical parameters influenced J_{sc} along of investigated sensitizers: (a) the light-harvesting efficiency, (b) the electronic injection free energy

3.2.7 Ionization Potential and Electron Affinity

Ionization potentials (IP) and electron affinities (EA) are two important parameters of dye molecules in determining charge injection and charge transport properties. For outstanding performance of dyes, a better charge transfer and injection capability are required. Therefore, they need a high EA value for electron injection/transportation and a low IP value for hole injection/transportation. The calculated IP and EA values are presented in table 3.7. Among the studied molecules dye, D8 possesses the lowest IP value, which means better hole injection capability. For instance, the IP of D8 is

6.28, while for D1, it is 6.48 eV. This suggests that D8, where the triphenylamine unit as a donor, has better hole injection capability. On the other hand, dye D7 possesses the highest EA value indicating easy transport of electrons from the electrode to this compound.

Table 3.7 Ionization potential (IP), electron affinity (EA) and chemical reactivity (in eV) of investigated dyes.

	IP	EA
D1	6.48146	1.88054
D2	6.9262	2.02915
D3	6.55025	2.11762
D4	6.86478	2.15057
D5	6.85387	2.13522
D6	6.73117	1.82387
D7	6.92848	2.22148
D8	6.28853	1.99857

3.2.8 Reorganization Energies

The reorganization energy λ_{tot} is considered as a significant factor that could influence the kinetics of electron injection Fig. 3.7. The calculated λ_{tot} is also important to analyze the relationship between the electronic structure and the J_{sc}. Generally, The smaller λ_{tot} means that the transfer charge could be favorable from the donor to the acceptor units of molecules. The calculated values of λ_e and λ_h of the compounds are reported in table 3.6. Vigilant observation of the table reflects that λ_h values are smaller than the λ_e values except for the dye D2. The difference in their values is also quite significant. This indicates that the studied compounds are an ideal material for hole transportation. It is also observed that the electron reorganization energy of D3, D5, D4, and D7 dyes are lower than the corresponding reference dye D1. Hence, D3 and D4 dyes will exhibit larger J_{sc}. For example, λ_e for D3 and D5 are 0.27 and 0.29 eV, respectively. This observation indicates that replacing the 9-Vinylcarbazole in the reference dye with 2-(2-Thienyl)furan or Benzofuran donor unit improves the value of λ_e. Similarly, λ_h for D3 is 0.25, which is lower than D1 dye. The λ_h of all dyes is smaller than λ_e this implies that the hole transfer rates in these compounds might be higher, except the D2 dye, which might possess a higher electron transfer due to the smaller λ_e compared with λ_h. Furthermore, the small values of reorganization energies indicate higher rigidity in these compounds, which is essential for efficient

charge transport. The difference between the hole and electron of all the studied dyes is less than 0.04 eV, indicating that they have better equilibrium properties for hole-electron-transport.

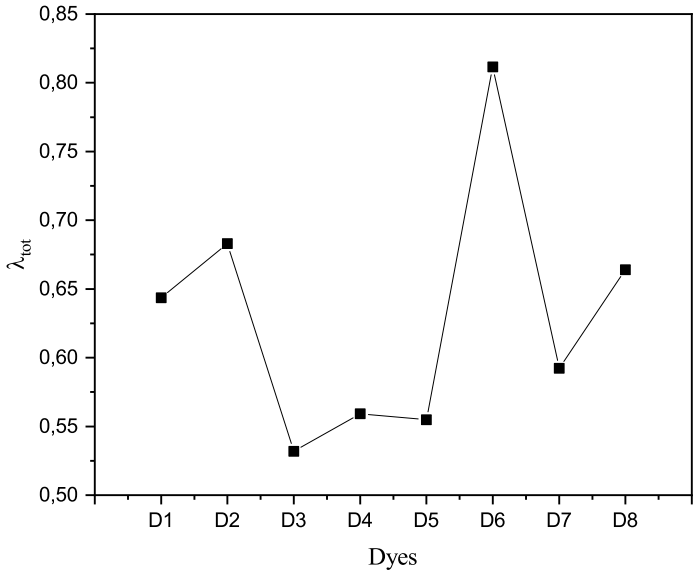


Fig. 3.7 The reorganization energy λ_{tot}.

3.2.9 Absorption

The excitation energy and UV/Vis absorption spectra for the singlet-singlet transition of all sensitized dyes were simulated using TDDFT with CAM-B3LYP functional in vacuo and chloroform solution based on the optimized ground-state structure to gain insight into the optical property and electronic transition. Based on the experimental work results [101], the THF solution was used as a solvent in the UV-Vis absorption spectra on the molecule D1 for comparison and the other molecules. Tabl 3.8 shows the values of the computed vertical excited singlet states, transitions energies, and oscillator strength in vacuo and in chloroform. The corresponding simulated UV-Vis absorption spectra of the studied compounds obtained at the IEF-PCM/TD- CAM-B3LYP/6-311G(d.p) level, presented as oscillator strength against wavelength, is shown in Fig. 3.8. A similar profile of the spectra has been noticed for all dyes. All compounds exhibit a strong absorption band in the visible region around 377 — 511nm. The calculated wavelength $\lambda_{\max}$ of the studied compounds decreases in the following order D3 > D7 > D8 > D5 > D4 < D1 < D2 < D6 showing that there is a bathochromic shift when passing from D6 to D3. This bathochromic effect from D6 (443.37nm) to D3 (491.28nm) can be attributed to the change in the donor moieties (the extent of

the conjugation), which causes a shift of the absorption toward the red for this dye D3 compared with D6. This can be attributed to the presence of electron-rich heteroatoms such as oxygen and sulfur in the donor unit. Also, in the D8 molecule containing triphenylamine, a change in the maximum absorption was observed compared with the D1.

Table 3.8 Absorption data λ_{max}(nm), oscillator strength (f), Excitation energy (eV) obtained by TD-DFT methods for the studied compounds.

Dye	solvent			vacuo		
	λ_{max}	E	f	λ_{max}	E	f
D1	452.50	2.74	1.39	429.02	2.88	1.29
D2	445.30	2.78	1.22	421.96	2.93	1.09
D3	491.28	2.52	1.60	439.55	2.18	1.32
D4	461.69	2.68	1.46	440.29	2.82	1.33
D5	462.28	2.68	1.46	420.17	2.81	1.14
D6	443.37	2.79	1.26	438.97	2.95	1.38
D7	463.35	2.67	1.51	439.97	2.82	1.42
D8	462.28	2.68	1.52	421.96	2.81	1.09

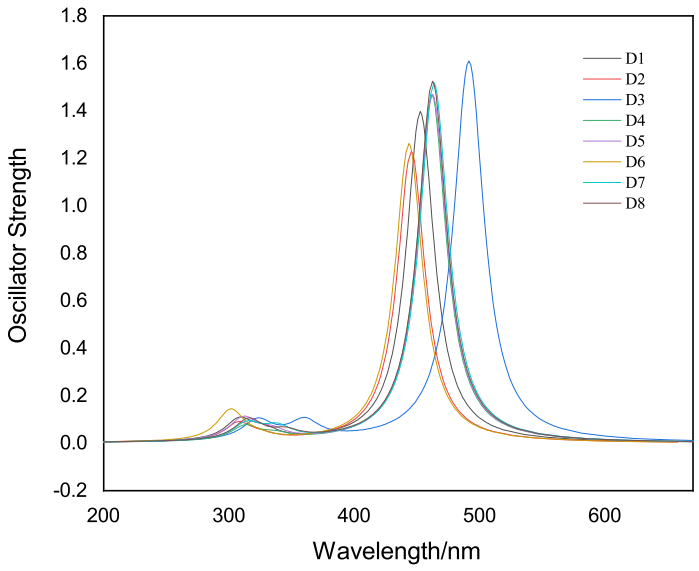


Fig. 3.8 Absorption spectrum of the studied dyes in THF solution.

3.3 Electronic and Optical Properties of Ethylcarbazole Based Materials

3.3.1 Computational Details

For the PEcbz-Ter, PEcbz-Ter, and PEcbz-Fur copolymers, we adopted the same procedure discussed in the previous colleagues' works. The calculations were carried out using the Gaussian 09 program. The structures have been optimized based on the density functional theory (DFT) and using the hybrid exchange-correlation functional B3LYP (Becke three-parameter Lee - Yang- Parr). The extended atomic orbital basis set 6-31G(d) has been used for all atoms. Frequency calculation was done to ensure that the obtained conformation is an energetic minimum. We also examined the HOMO and LUMO levels; the energy gap was evaluated as the difference between the energies of the frontier orbitals HOMO and LUMO. The absorption spectra were simulated from the optimized geometries, based on the Time-Dependent Density Functional Theory TD-DFT at the B3LYP/ $6-31$G (d) level. The vertical transition energies, the maximum absorption wavelengths, and their intensities have been determined.

The reorganization energy could be an important factor that governs the mobility of charge carriers in OFET applications. The reorganization energies for λ_e and λ_h, the ionization potential (IP), and the electron affinity (EA) of the molecules were also calculated, and the reader may be referred to the previous study the "Parameter Estimation Equations" for their equations.

To predict the stability of our copolymers from a viewpoint of molecular orbital theory, the absolute hardness, η, was calculated using operational definitions (Cornard and Lapouge, 2006) given by equations below [182, 183]

$$\eta = \frac{1}{2}\left(\frac{\partial \mu}{\partial N}\right) = \frac{1}{2}\left(\frac{\partial^2 E}{\partial N^2}\right) = \frac{IP - EA}{2} \tag{3.11}$$

Here, μ represents the chemical potential, N is the total electron number, ionization potential (IP), and adiabatic electron affinity (EA) of the molecules.

3.3.2 Optimized Geometries

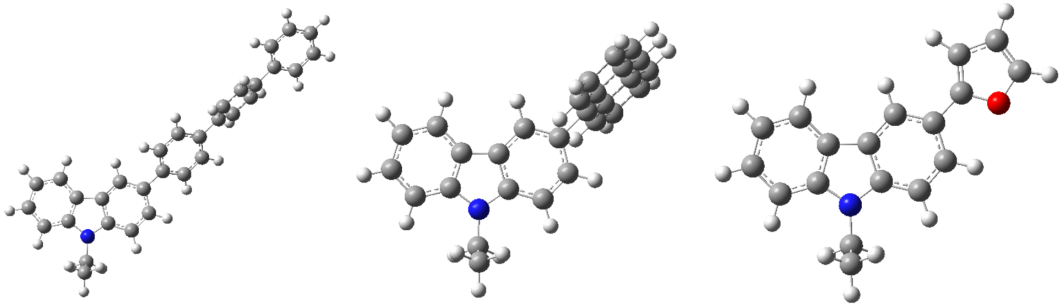
The structural properties of a material that can be used in an OFET device are fundamental. The more this material adopts a planar geometry, the more the charge exchange with the system is favored. It has also been shown that the rigid and planar

conformation of the conjugated skeleton of several semiconductor polymers, allows a stacking and efficient crystallization. The optimized structures are shown in Figure and the geometric parameters (bond distances and dihedral angles) are shown in Table 3.9.

Table 3.9 Inter-ring distances di Å and dihedral angles θ (deg) of PEcbz-Ter, PEcbz-Ant, and PEcbz-Fur.

Compounds	Form	θ	d_1	d_2	d_3
PEcbz-Ter	Neutral	142.48	1.48	1.48	1.48
	Cation	155.51	1.45	1.46	1.47
	Anion	156.76	1.46	1.44	1.45
PEcbz-Ant	Neutral	104.39	1.49	–	–
	Cation	127.21	1.46	–	–
	Anion	120.65	1.48	–	–
PEcbz-Fur	Neutral	178.71	1.45	–	–
	Cation	179.90	1.42	–	–
	Anion	177.57	1.45	–	–

The optimized structure is presented in a rounded configuration with different dihedral angles (θ). This can be explained by the existence of the steric hindrance effect between the fragments. The results of the optimized structures show that PEcbz-Ter and PEcbz-Fur materials have almost planar structures, while PEcbz-Ter has a crisscrossed structure. We found that the three copolymers have different dihedral angles 142.48, 104.39, and 178.71 for PEcbz-Ter, PEcbzFur, and REcbz-Ter, respectively. The inter-cyclic distances between the Ethylcarbazol and the building block units vary from 1.45 to 1.49 Å depending on the molecule (Terphenyl, Anthracene, and Furan) table 3.9. The distances and the dihedral angles were also extracted from the anionic and cationic forms. It is interesting to understand how the doped π-conjugate molecule becomes responsible for the transport of charges. During the doping process of the optimized structure obtained at the neutral state, the parameters have significantly changed. The single bonds become shorter for all the studied compounds, while the double bonds become longer. Likewise, intercyclic bonds are longer than standard double bonds (Table 3.9), Focusing on PEcbz-Ter, the inter-cyclic distance between Ethylcarbazal and Terphenyl has changed from 1.48 Å to 1.46 Å. It seems that even distances between the terphenyl cycles have effectively changed from the neutral to the anionic form. The coplanarity of the whole material has improved as well. The incorporation of different polymers with Ethylcarbazol modifies the whole structural parameters.



(a) (b) (c)

Fig. 3.9 Optimized geometry of a) PEcbz-Ter, b) PEcbz-Ant, and c) PEcbz-Fur

3.3.3 Frontier Molecular Orbital

The electronic properties of π-conjugated semiconductor polymers mainly depend on the energy levels of the HOMO and LUMO frontier orbitals and the mobility of electrons and holes. As we mentioned in our previous studies, the energy gap is an important parameter that determines the photoabsorption of the molecule. By analyzing the results reported for the different copolymer, we notice a change in the calculated energy gap of the oligomers when changing the polymer block. These results tell us that the type of polymer link to the Ethylcarbazol unit has a significant effect on electronic transitions. To fully understand the properties of the studied oligomers, it is crucial to examine the electron density distributions at the HOMO and LUMO frontier orbitals since the relative order of occupied and virtual orbitals provide a reasonable qualitative indication of the excitation properties and the capacity of electron-hole transport.

Table 3.10 summarizes the HOMO, LUMO, and energy gap of the three copolymers. From the table, it can be noted that all the studied compounds (PEcbz-Ter, PEcbz-Ter, and REcbzFur) exhibit a change in frontier orbitals. The HOMO and LUMO energies of PEcbz-Ter, PEcbzTer, and PEcbz -Fur change significantly, (-5.16eV, -5.02eV and -4.94 eV for HOMO and -1.05 eV, -1.52 eV and -0.70 eV for LUMO, respectively). This implies that the nature of the substituents and the structure's nature affect the electronic properties. Besides, the Eg energies are 3.50eV, 4.10eV, and 4.24eV depending on the different structures, and they are in the following order PEcbz-Fur $<$ PEcbz-Ter $<$ PEcbz-Ant. Both PEcbz-Ter and PEcbz-Ant compounds exhibit lower HOMO, LUMO energies with a smaller gap compared to PEcbz-Ant. This difference due to the presence of Terphenyl and Anthracene that possess more conjugation bonds in their structure.

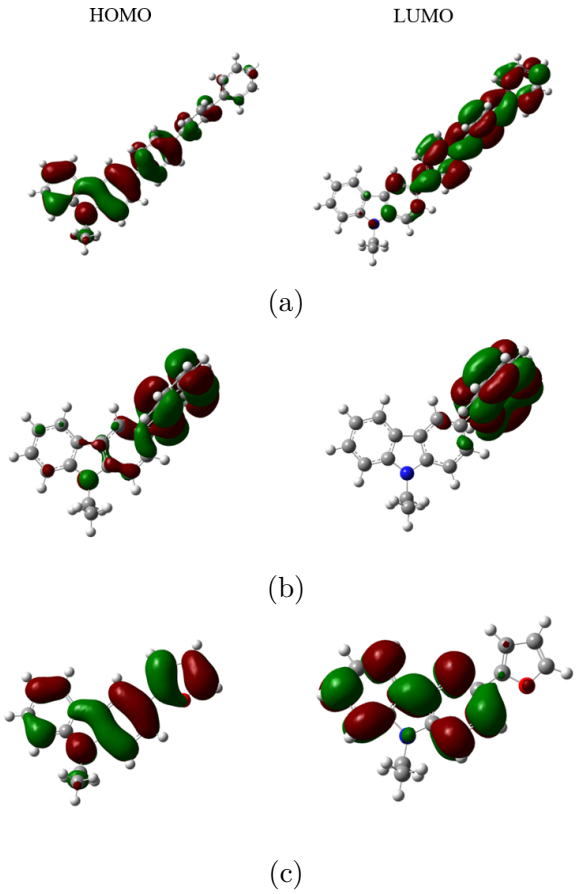


Fig. 3.10 HOMO and LUMO of a) PEcbz-Ter, b) PEcbz-Ant, and c) PEcbz-Fur.

We have presented in Table 3.10, the values of the gap energies of the studied molecules in their neutral and polaronic forms with neutral state values for comparison. We note that the gap energy decreases when passing from the neutral to the doped form for all the compounds studied, especially for PEcbz-Ter.

Frontier orbitals of PEcbz-Ter, PEcbz-Ant, and PEcbz-Fur are shown in Fig. 3.10 It is essential to examine the distribution of HOMO and LUMO of these compounds because the relative order of occupied and virtual orbitals provides a reasonable qualitative indication of the excitation properties. Electronic distribution of HOMO is distributed over the entire structure backbone, while the LUMO concentrated on Terphenyl and Anthracene for PEcbz-Ter, PEcbz-Ant, the opposite for PEcbz -Fur. HOMO has a binding character between units, while LUMO shows an anti-binding character between sites.

Table 3.10 HOMO (eV), LUMO (eV) and Egap (eV) values of the studied compounds.

Compounds	Form	HOMO	LUMO	Eg
PEcbz-Ter	Neutral	-5.16	-1.05	4.10
	Cation	-8.15	-4.38	3.77
	Anion	0.82	1.54	0.71
PEcbz-Ant	Neutral	-5.02	-1.52	3.50
	Cation	-8.39	-5.34	3.04
	Anion	1.06	1.82	0.75
PEcbz-Fur	Neutral	-4.94	-0.70	4.24
	Cation	-9.09	-4.88	4.20
	Anion	2.04	3.13	1.09

3.3.4 Reorganization Energies and Stability

Reorganization energy is considered one of the important parameters that affect the charge mobilities in organic semiconductors. The calculated reorganization energies for hole and electron are listed in Table 3.11. It is well-known that the lower the reorganization energy values, the higher the charge transfer rate [184]. The reorganization energies calculated for hole λ_h of PEcbz-Ter, PEcbz-Ant, and PEcbz-Fur are 0.25 eV, 0.30 eV and 0.33 eV, respectively. The λ_h of PEcbz-Ter is smaller than both PEcbz-Ant, and PEcbz-Fur this implies that the hole transfer rates of PEcbz-Ter might be higher than that of PEcbz-Ant and PEcbz-Fur. Thus, PEcbz-Ter could be hole transport material from the standpoint of the smaller reorganization energy. The λ_e value of PEcbz-Ant is smaller compared to PEcbz-Ter and PEcbz-Fur. This indicates that its electron transfer rate might be higher. Besides, The λ_e value of PEcbz-Ant is smaller than its λ_h value, suggesting that the carrier mobility of the hole is larger than that of the electron. Hence, PEcbz-Ant can be used as promising electron transport materials in the OFETs from the standpoint of the smaller reorganization energy. Also, the difference between the hole and electron of PEcbz-Ant is 0.07 eV, indicating that it has better equilibrium properties for hole-electron-transport. Furthermore, the small values of reorganization energies indicate higher rigidity in these compounds, which is important for efficient charge transport.

As we mentioned in the previous study, the achievement of high electron affinity (n-type)conjugated polymers for improving electron injection/transport and low ionization potential (p-type) conjugated polymers for better hole injection/transport is a general challenge for the application of polymers in optoelectronic devices. Therefore, the ionization potential (IP) and electron affinity (EA) are well-defined properties that can be calculated by DFT to estimate the energy barrier for the injection of both holes and

electrons into the polymer. The ionization potentials (IPs) and electron affinities (EAs) of the three copolymers are presented in Table 3.11. The energies needed to create a hole in the polymers for the PEcbz-Fur material are all greater than those of the PEcbz-Ter and PEcbz-Ant. Thus, the hole injection and transportation of PEcbz-Fur are expected to show that the charge carrier balance is better in the devices constructed from these copolymers. The extraction of an electron from the anion requires 0.32 eV for PEcbz-Fur, which is larger than those in the PEcbz-Ter and PEcbz-Ant. This indicates that the combination with charge carriers moiety or extending the conjugated backbone will improve the electron-accepting/transporting properties. From these findings, it is evident that the optoelectronic properties of a conjugated polymer are primarily governed by the chemical structure of the polymer backbone. This should be useful to enhance the electron-transport in organic-field-effect Transistors.

Table 3.11 Calculated molecular λ_e, λ_h, η, Ionization potential (IP) and Electron affinity (EA) (all in eV) of the copolymers

Compounds	λ_e	λ_h	IP	EA	η
PEcbz-Ter	0.44	0.25	6.20	0.11	3.04
PEcbz-Ant	0.23	0.30	6.14	0.20	2.97
PEcbz-Fur	0.24	0.33	6.28	0.32	2.98

As stability is a useful criterion to evaluate the nature of devices for charge transport. The η values of investigated molecules were calculated and presented in Table 3.11. The η is the resistance of the chemical potential to change in the number of electrons. Examination of Table 3.11 exposes clearly that the η values of the three copolymers are almost identical, indicating improved stability.

3.3.5 Absorption Properties

Based on the optimized structures with the B3LYP/ 6-31G (d) method, we obtained the ultraviolet-visible (UV-VIS) spectrum of the studied compounds PEcbz-Ter, PEcbz-Ant, and PEcbz-Fur using the TD-DFT method. Table 3.12 presents the absorption wavelengths ($\lambda_{\max}$), the oscillator strength (f), and excitation energies (E) of the three copolymers.

The absorption wavelengths arising from the S0 $\rightarrow$ S1 electronic transition are $333.78nm, 393.13nm$, and 338.01 nm for PEcbz-Ter, PEcbz-Ant, and PEcbz-Fur, respectively. The obtained values are in good agreement with the experimental results in parentheses Table 3.12. This is reasonable since the HOMO $\rightarrow$ LUMO transition is predominant in the S0 $\rightarrow$ S1 electronic transition. Therefore, the DFT method gives a good

description of the studied compound's absorption properties and can be used to predict the electronic characteristics for other materials. Note that the difference between theoretical and experimental values can be explained by the fact that the calculations assume that the molecules are in the vapor state. The PEcbz-Ter copolymer has the minimum wavelength with higher oscillator strength of 1.00 compared with PEcbz-Ant, and PEcbz-Fur. The oscillator strength for an electronic transition is proportional to the transition moment. In general, larger oscillator strength corresponds to a larger experimental absorption coefficient or stronger fluorescence intensity.

Table 3.12 Calculated maximum absorption wavelengths $\lambda_{\max}$ (nm), the oscillator strength (f), and excitation energies E (eV).

Compounds	$\lambda_{\max}$	$\lambda_{\exp}$	E	**f**
PEcbz-Ter	333.78	312	3.71	1.00
PEcbz-Ant	393.13	384	3.15	0.14
PEcbz-Fur	338.01	359	3.66	0.02

3.3.6 Summary

We've put all the properties together in one table for a clear view for comparison. from the table it is clear that all three copolymers have good electronic properties. However, it can be deduced therefrom that terphenyl and anthracene may be more advantageous concerning these properties which makes them suitable as semiconductor materials, in particular for organic field-effect transistors. in the next chapter, we will study more experimentally the use of these materials in organic electronics.

Table 3.13 All the properties calculated by DFT.

	PEcbz-Ter	PEcbz-Ant	PEcbz-Fur
HOMO	-5.16	-5.02	-4.94
LUMO	-1.05	-1.52	-0.70
gap	4.10	3.50	4.24
λ_e	0.44	0.23	0.24
λ_h	0.25	0.30	0.33
IP	6.20	6.14	6.28
EA	0.11	0.20	0.32
η	3.04	2.97	2.98

3.4 Conclusion

In this chapter, we have studied, by the DFT method, the structural and electronic properties of new organic systems. The first set of material was based on polypyrole, the comparison of the results makes it possible to discover the effect of the transition from the DOTP to DH4P as well as of the doping on the structure and on the properties. The quinoid contribution appears strongly in the doped structures, and the increase in size is accompanied by a decrease in the gap and high stability. Investigation of substituted alkyl groups at sites 3 of the pyrrole cycle suggests that R3 $=C_{12}H_{25}$ and R4 substitution leads to the HOMO and LUMO stabilization and reduces gap energy. The absorption was also influenced by substitution, then a redshift is observed from ddoD4P to DH4P. The second series of materials was based on selenophene molecule. Different functionals were employed to choose the convenient functional correlated with the experimental results, and CAM-B3LYP functional was the best choice. We have examined the role of different electron-donor groups in tuning the geometries, electronic structures, and optical properties. We also discussed the dependency of the photovoltaic parameters (open-circuit voltage (V_{oc}), oxidation potential energy, and electron injection force) with electron-donor group changing. These organic materials show promising electronic and photovoltaic properties with respect to other dyes, therefore it can be suggested as a good photosensitizer for use in DSSC. The last sets of materials were three copolymers Ethylcarbazole based, the copolymers have good electronic properties. However, two specific ones exhibit more advantageous properties which make them suitable as semiconductor materials, in particular for organic field-effect transistors. In the next chapter, these last three materials will be studied more experimentally to make a correlation between what we found theoretically and experimentally.

Chapter 4

Experimental Study of Ethylcarbazole Based Materials

Characterization measurements are potent tools to obtain an insight into the structure of materials. Also, dielectric properties can provide valuable information on the electrical properties of ions, atoms, molecules, and, most importantly, their behavior within materials. Therefore, in this chapter, we will present the synthesis procedure of the organic materials used in this work and the verification of their crystallinity and absorption properties by X-ray diffraction, scanning electron microscopy, and UV-vis techniques. Afterward, we will provide a detailed study of dielectric properties such as (dielectric constant, dielectric loss, and ac conductivity) as a function of temperature and frequency.

4.1 Synthesis of The Studied Materials

The three co-polymers are synthesized in the Laboratory of Chemistry-Biology Applied to the Environment by the Professor Bennani team at the Faculty of Sciences, Moulay Ismail University [185, 186]. Poly(9-Ethylcarbazole) (PEcbz) powder (97%), p-Terphenyl (Ter) (99%), Anthracene (Ant) (99%) and Furan (Fur) (99%), fercichloride ($FeCl_3$), chloroform $CHCl_3$, (99%), methanol CH_3OH (99%), used for the synthesis of the studied compounds were purchased from Sigma Aldrich.

The Poly(Ethylcarbazale-Terphenyl) (PEcbz-Ter) copolymer was synthesized by an oxidative chemical reaction using $FeCl_3$ as the oxidizing agent. Firstly, 120mg of Poly (Ethylcarbazale) was dissolved and stirred in 25ml of chloroform $CHCl_3$, and 1g of $FeCl_3$ dispersed in 40ml of $CHCl_3$ before adding to this mixture another chloroform solution (25ml again) containing 120mg of P-Terphenyl and kept in a flask. The

color of the solution changed rapidly from orange to red dark, then to black, and the reaction was kept under stirring and heating at a temperature of 70°C for 72h. Then, to eliminate the residues of $FeCl_3$, an excess of ethanol was added, and the resulting solution was filtered several times. As expected with such experimental conditions and as evidenced by the color-changing, we should obtain the oxidized material: this is why in order to obtain the polymer in the neutral state, we mixed then the crude solid into 40ml of ethanol for 24h. Once again, we can follow the success of the development by a color modification, the solution tuning from dark black to beige. Finally, the precipitate was filtered under pressure, then washed several times with ethanol, and dried under vacuum overnight. We obtained the Poly(Ethylcarbazole-Terphenyl) copolymer in the neutral state. To characterize the synthesized copolymer, two samples of copolymer are tested several times to ensure the stability and reproducibility of results. Poly(Ethylcarbazole-Anthracene) (PEcbz-Ant) and Poly(Ethylcarbazale-Furan) (PEcbz-Fur) have been prepared the same way as the previous copolymer.

During my stay in Italy, I was involved in the FIRE project at the national institute of nuclear physics, Rome. The project aims to build an organic field-effect transistor to detect different radiation (the reader may refer to the future work at the end of the thesis for more information). Therefore we purchased new reagents to make a new synthesis to use the new synthesis materials in the OFET application. In the new synthesis, we employed the same procedure, but we add the monohydrate hydrazine as a reducing agent where we mixed the crude solid obtained of the copolymers adding $5-10$ml monohydrate hydrazine for 12 h. The synthesized samples without hydrazine can be abbreviated by PEcbz-Ter, PEcbz -Ant, and PEcbz-Fur, while PEcbz-Ter(H), PEcbzAnt (H), and PEcbz-Fur(H) were prepared using hydrazine.

4.2 X-ray Diffraction Analysis

X-ray diffraction was made on the materials that were prepared as a powder by $FeCl_3$ coupling reaction and the scanning conditions were the same for all of the materials.

4.2.1 Poly(Ethylcarbazole-Terphenyl)

The X-ray Diffraction (XRD) spectra of the synthesized of PEcbz-Ter with and without H compared with the starting materials (ECb and Ter) is shown in Fig. 4.1, the diffractogram of the studied copolymer PEcbz-Ter without H green line has

characteristic peaks of both the monomers ethylcarbazole (Ecbz) and terphenyl (Ter) with peaks located at $2\theta = 6.48°, 13.1°$ $20.35°, 28°, 37.58°$ with terphenyl peaks are dominant [185]. While PEcbz-Ter(H) copolymer black line, most of the peaks are intensified markedly, reflecting a new morphology of the copolymer. The existence of fine and intense peaks reflects a structural order in the copolymer and, therefore, the existence of crystalline regions. The disappearance of the PEcbz-Ter(H) copolymer of the peaks of ethylcarbazole (Ecbz) and terphenyl explains the new structure of the copolymer obtained, which does not necessarily correspond to the presence of the two phases (Ethylcarbazole and Terphenyl). These results indicated that the PEcbz-Ter using the H in the synthesis, the crystalline structure is improved.

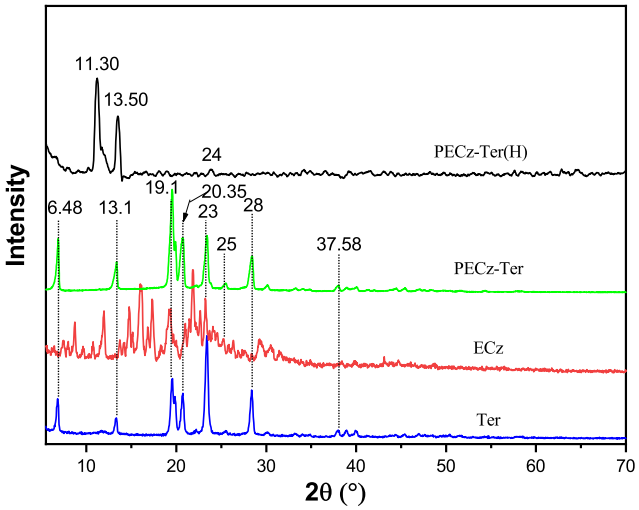


Fig. 4.1 XRD pattern spectra of PEcbz-Ter, PEcbz-Ter(H) and the starting materials (ECz and Ter)

4.2.2 Poly(Ethylcarbazole-Anthracene)

The XRD pattern spectra of PEcbz-Ant with and without hydrazine in comparison with the starting materials (Ebcs and Ant) is sighted in Fig. 4.2. for the PEcbz-Ant specter green line six major peaks are observed at 2θ equal to 9.6°, 19.5°, 21°, 25°, 26°, 29° these peaks are intensified a marked way, and the dominant peaks are of (Ecz). The reflection of low intensity is observed in the high angle region (35°-70°), which reflects a new morphology of the copolymer. The existence of fine and intense peaks at $9.5\circ$ and $35\circ$ reflects a structural order in the copolymer (crystalline regions) [186]. For the copolymer using hydrazine PEcbz-Ant(H) black line, we noticed the same diffractometer appear with an increase in the number of the peaks.

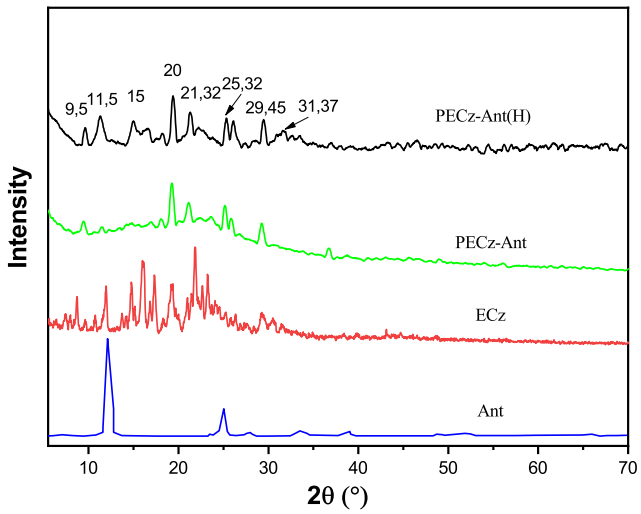


Fig. 4.2 XRD pattern spectra of PEcbz-Ant, PEcbz-Ant(H) and the starting materials (ECz and Ant)

4.2.3 Poly(Ethylcarbazole-Furan)

In contrast with the other two copolymers PEcbz-Ter and PEcbz-Ant that clearly showed a sharp maxima in their XDR pattern, PEcbz-Fur copolymer presents a very weak and broad diffraction peak appear around 2θ equal to 5° and 12°, as can be noticed in Fig. 4.3 green line. This may be attributed to a partially ordered structure for this copolymer. Besides, We noticed that the diffractometer was totally different and improved for the copolymer with hydrazine PEcb-Fur(H) black line around 2θ between 25° and 65°.

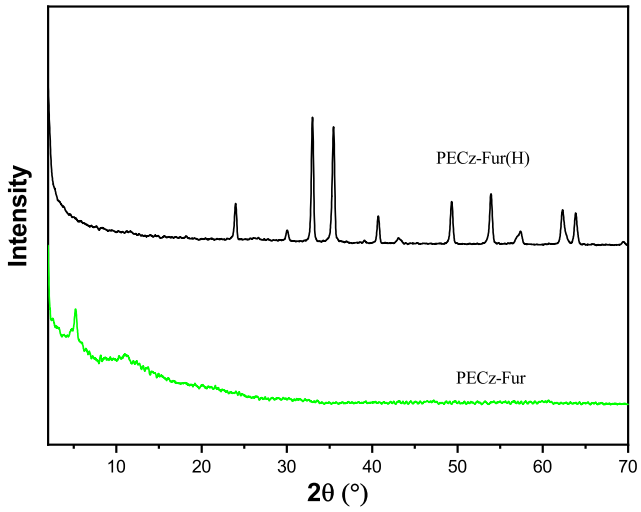


Fig. 4.3 XRD pattern spectra of PEcbz-Fur and PEcbz-Fur(H)

4.3 UV-VIS Analysis

In this section, a detailed analysis of the results obtained from the absorption spectrum of the studied co-polymers recorded at ambient temperature in the solid state.

4.3.1 Poly(Ethylcarbazole-Terphenyl)

According to Fig. 4.4 the synthesized copolymer PEcbz-Ter absorbs both in the visible and UV-Vis region. In the UV region, part of the electromagnetic spectrum with absorption bands centered at (227 and 312 nm). While in the visible part an absorption band centered at around (500, 616, 682 and 815 nm). The one located at 312 nm is arising from delocalized $\pi - \pi^{\star}$ transition in the polymer and the other occurring at 500 nm should originate from a charge transfer state [25]. The effect of the oxidation of the synthesized copolymer is seen in the optical absorption spectrum, characterized by polaronic/bipolaronic bands located at 815 nm (1.36 eV). These spectral features are characteristic for organic conducting polymers [26-30]. A wide absorption bands at 815 nm is observed resulting from the coexistence of polaronic and bipolaronic charge carriers, proving the formation of new backbone resulting from the grafting of Poly (Terphenyl) into the skeleton of the crosslinked PEcbz. PEcbz absorbs entirely in the UV region ($\lambda \max < 350\text{nm}$). So the UV–Vis absorption spectra showed maximum absorption wavelengths of 312 nm. This can be interpreted as $\pi - \pi^{\star}$ transition, due to the presence of PEcbz in the two copolymer.

The extension of the optical absorption in the case of a copolymer (from 400 nm to 800 nm) shows an increase in the conjugation length. The deduction of the optical gap is judged for the copolymer is $E_g = 2.64\text{eV}$, which can be identified by extrapolating the linear portion of the wavelength band of the highest (maximum absorption). Moreover, the energy corresponding to the $\pi - \pi^{\star}$ transition depends on the delocalization of the π-electrons system. This delocalization is determined by the effective conjugation length, which depends on the amount of structural and conformational defects in the polymer backbone and the interaction between polymer backbones [185]. When adding the hydrazine to PEcbz-Ter, the optical band changes especially for the maximum absorption, which shifted from 312nm (PEcbz-Ter) to 390 nm. A difference in the bandgap was also noticed when extrapolating the linear portion of the wavelength band and gives a value of E_g =2.79 eV.

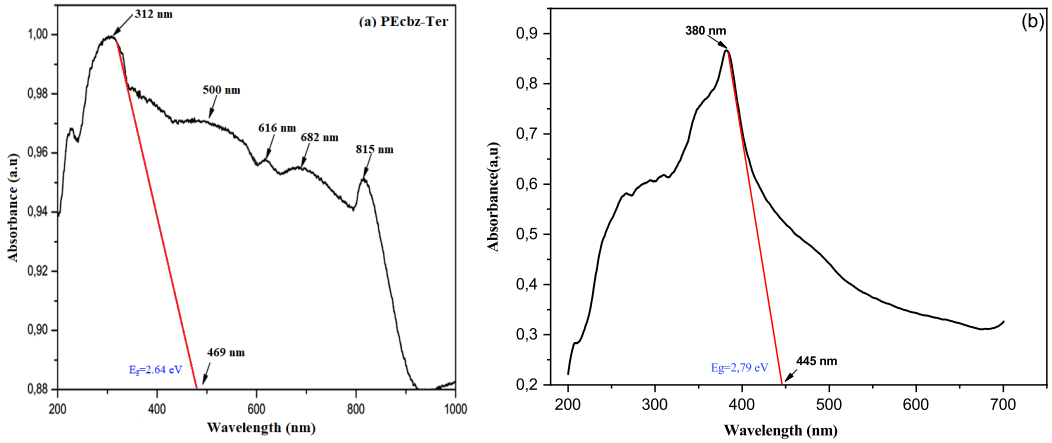


Fig. 4.4 UV-VIS spectrum of (a) PEcbz-Ter, (b) PEcbz-Ter(H)

4.3.2 Poly(Ethylcarbazole-Anthracene)

Refer to Fig. 4.5 PEcbz-Ant absorbs both in the visible and UV-Vis region. In the UV region, part of the electromagnetic spectrum with absorption bands centered at $(261, 302, 352$, and 384nm). While in the visible part an absorption band centered at around $(410, 603$ and 891nm). The one located at 261nm are arising from delocalized $\pi - \pi^{\star}$ transition in the polymer and the other occurring at 410 nm should originate from a charge transfer state [25]. The effect of the oxidation of the synthesized copolymer is seen in the optical absorption spectrum, characterized by polaronic/bipolaronic bands located at (891(1.39eV)−. These spectral features are characteristic for organic conducting polymers [26-30]. A wide absorption bands at 891 nm is observed resulting from the coexistence of polaronic and bipolaronic charge carriers, proving the formation of new backbone resulting from the grafting of Poly (Anthracene) into the skeleton of the crosslinked PEcbz. PEcbz absorbs entirely in the UV region ($\lambda \max < 350$nm). So the UV-Vis absorption spectra showed maximum absorption wavelengths of about 261 nm and 302 nm This can be interpreted as $\pi - \pi^{\star}$ transition, due to the presence of PEcbz in the copolymer.

The extension of the optical absorption in the case of a copolymer (from 400nm to 800 nm) shows an increase in the conjugation length. The optical gap is $E_g =$ 3.54eV. Moreover, the energy corresponding to the $\pi - \pi^{\star}$ transition depends on the delocalization of the π -electrons system. This delocalization is determined by the effective conjugation length, which depends on the amount of structural and conformational defects in the polymer backbone and the interaction between polymer backbones[186]. In the case of PEcbz-Ant (H), we observed the maximum absorption

transition at 420 nm, and the peak was broadened compared to PEcbz-Ant without hydrazine. Besides, the optical bandgap was different and had a value of E_g =2.40 eV.

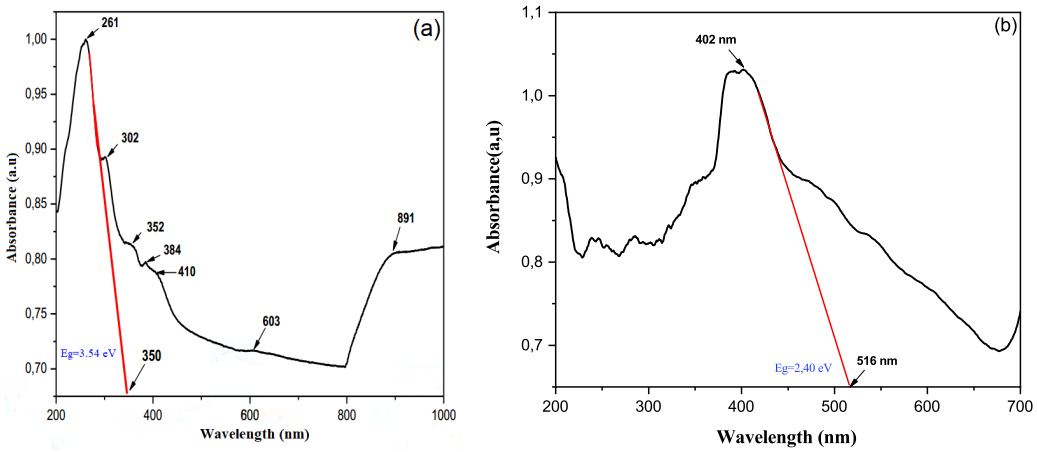


Fig. 4.5 UV-VIS spectrum of (a) PEcbz-Ant, (b) PEcbz-Ant(H)

4.3.3 Poly(Ethylcarbazole-Furan)

Similary to the previous materials, in the UV region, the absorption bands located at 247nm, 278nm, 359nm . It is known that PEtCbz absorbs in the UV at λ_{max} <350 nm, so the bands located at 247nm correspond to the $\pi - \pi^{\star}$ transition delocalized in the copolymer. The absorption bands are centered at 421nm, 668nm in the Visible part. The presence of absorption bands around 421 nm for the copolymers shows that there was a charge transfer in the D-A segment, that is to say, between EtCbz and Ant. The presence of absorption bands towards long wavelengths (861 nm and 894nm), shows a bathochromic effect due to an increase in conjugation along the polymer chain. This can be explained by the greater value of the oxidation potential of $FeCl_3$, which produces a greater reactivity with the oxidant $FeCl_3$. The broadband absorbance results from the coexistence of polaronic and bipolaronque charge carriers, thus proving the formation of the copolymer. The optical gap calculated gives the values of 3.54 eV on the wavelength axis. This energy, corresponding to the $\pi - \pi^{\star}$ transition, depends on the delocalization of the π electron system. Therefore, this delocalization varies according to the type of copolymer since it is determined by the effective conjugation length and the quantity of structural and conformational defects in the polymer chain.

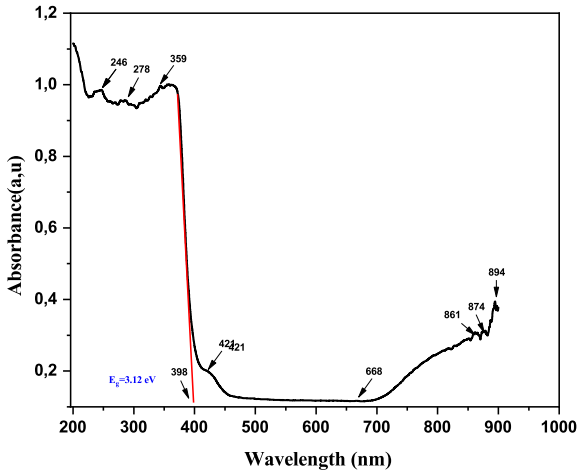


Fig. 4.6 UV-VIS spectra of PEcbz-Fur

4.4 Scanning Electron Microscopy Analysis

The analysis of the copolymer structure requires a large resolution [187]. To make high-resolution images from the sample structure, scanning electron microscopy (SEM) can be used. The SEM of PEcbz-Ter, PEcbz-Ant, and PEcbz-Fur copolymers pellets pressed at 50MPa is shown in Fig.4.7. The morphology of the PEcbz-Ter sample is relatively heterogeneous, contained mostly large aggregates. The large grains are interspersed with small grains with an average of 488 nm, surrounded by clear boundaries, with some holes with a dark black color (Fig.4.7(a)). For the PEcbz-Ant copolymer pellet, a dense microstructure consists of large grains and small grains with an average size of 844 nm (Fig.4.7(b)). In contrast, the PEcbz-fur copolymer consists of small homogeneous grains and a very small amount of large grains Fig.4.7(c). The large grain regions may be related to mainly crystalline domains, and the small grains related to the amorphous regions in the materials. These results agree with the X-ray data obtained in section 4.2, which suggests that PEcbz-Ter is more structured than the other two copolymers. These results are also appropriate with substances of the same nature (PDOT: PSS and Polyaniline) that have been studied in previous literature [188, 189].

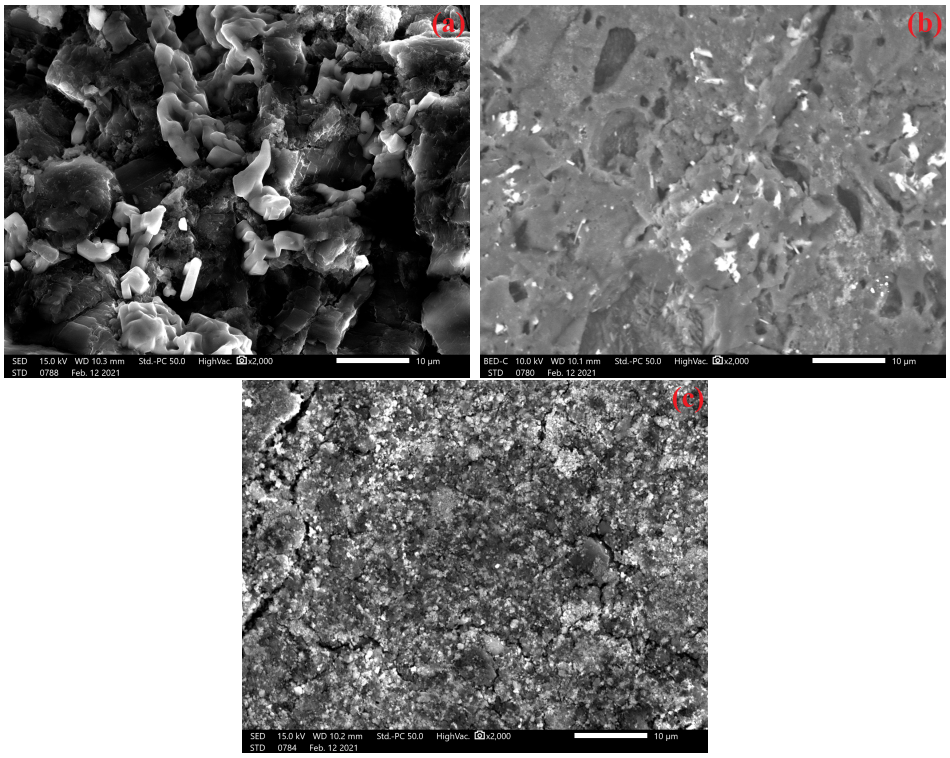


Fig. 4.7 SEM images of the studied co-polymers pellets: (a) PEcbz-Ter, (b) PEcbz-Ant and (c) PEcbz-Fur

4.5 Dielectric Properties and Conduction Mechanism

4.5.1 Preparation of The Materials

Dielectric characterization was carried out on a grounded powder of ethylcarbazole-based materials which were pressed by a hydraulic press under ~ 50 MPa at room temperature to form a pellet with a disk shape. The surface of the pellet is well polished to dryness and metallized by a thin layer of silver paste in order to obtain two parallel plates; the pellet had the same radius as the electrodes, which are 12 mm in a circular disk shape, and the thickness were between 1.75-1.80 mm. The real (ε'_r) and imaginary (ε''_r) parts of the permittivity of this compound are measured in the frequency $1\text{kHz} - 2\text{MHz}$ and temperature range from R.T to 120°C by using the complex impedance spectroscopic technique. The real part (ε'_r) of the dielectric constant of the material was calculated by using the formula (2.39) defined in chapter two:

$$\varepsilon' = \mathrm{Cd}/\mathrm{A}\varepsilon_0$$

where C is the capacitance of the sample, d is the thickness of the disk, A is the surface area of the electrode, $\varepsilon_0 = 8.85 \times 10^{-12}$F/m the permittivity of free space. The capacitance C and loss factor ($\tan(\delta)$ or D) can be obtained directly from the measurements. The amplitude of the ac electric signal applied to the samples was 1V.

4.5.2 Dielectric Constant

The results of dielectric constant (ε'_r) for the PEcbz-Ter, PEcbz-Ant and PEcbz-Fur against frequency at select few temperatures are plotted in Fig. 4.8 For all samples, at low frequency, dielectric constant rapidly decreases then exhibit a step at higher frequencies. The same behavior is observed by El-Nahass et al. [190] for p-N,N dimethylaminabenzylidenemalononitrile (DBM) organic dye. This decrease may be due to the incapability of the dipoles to rotate fastly enough so they oscillate behind the field and it's called dielectric relaxation. A phenomenon that tells that the charge carrier localization is not stable and affected by the frequency disturbances [191]. At low frequencies, charge carriers respond faster with the externally applied electric field, resulting in the higher value of $\varepsilon'_{\mathrm{r}}$. At higher frequencies, charge carriers are unable to follow the rapid changes in the applied electric field, resulting in low values of $\varepsilon'_{\mathrm{r}}$. The decrease of dielectric constant with the applied field frequency can be explained based on several types of polarization (ionic, orientation, and electronic).

The ionic polarization due to the application of an electric field on a material induces a displacement of the positive ions relative to the negative ions. This polarization intervenes for frequencies lower than terahertz. The orientation polarization occurs up to frequencies between 1 kHz and 1MHz and is related to the structure of the material. Under an applied field, the permanent dipoles of the molecules are oriented in the direction of the field. The electronic polarization is due to the displacement of the electron cloud of the atom with respect to its nucleus. The last one, electron polarization is due to a relative displacement of the nucleus of the atom relative to all the electrons that surround it. This type of polarization is established in a very short time and remains sensitive up to frequencies exceeding those of visible light (1015 Hz). The orientation polarization is prevalent because it required a longer time compared to other polarizations. Therefore, the value of dielectric constant $\varepsilon'_{\mathrm{r}}$ decreases reaching a constant value at higher frequency corresponding to interfacial polarization. This

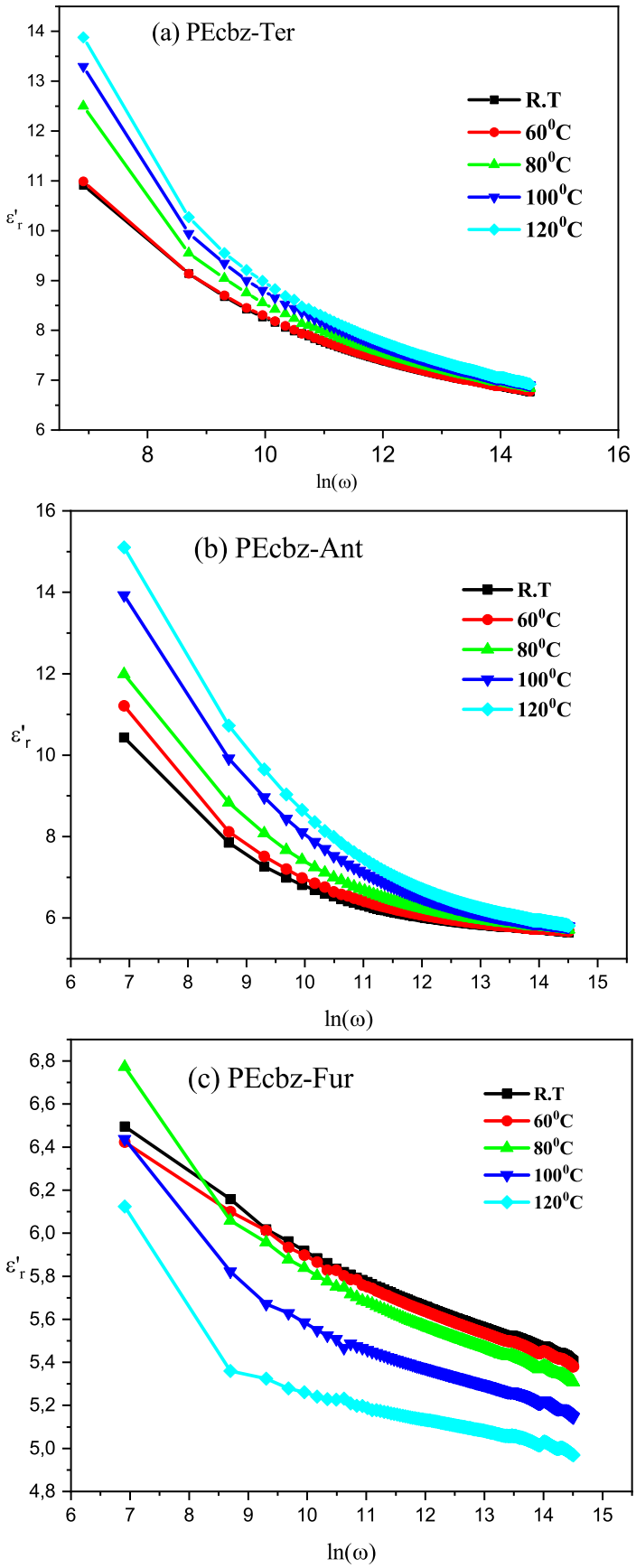


Fig. 4.8 Dielectric constant of a) PEcbz-Ter, b) PEcbz-Ant and c) PEcbz-Fur as a function of frequency at different temperatures

decrease may be due to the incapability of the dipoles to rotate fastly enough so they oscillate behind the field and it's called dielectric relaxation. A phenomenon that tells that the charge carrier localization is not stable and affected by the frequency disturbances.

Table 4.1 Dielectric Constant $\varepsilon'_{\mathrm{r}}$ and Dielectric Loss $\tan\delta$ at selected frequency.

Compounds	Frequency (kHz)	AT R.T		AT 120°C	
		$\varepsilon'_{\mathrm{r}}$	$\tan\delta$	$\varepsilon'_{\mathrm{r}}$	$\tan\delta$
PEcbz-Ter	11	8.67	0.15	9.54	0.23
	600	7.03	0.05	7.26	0.07
	2000	6.76	0.04	6.91	0.05
PEcbz-Ant	11	7.26	0.24	9.65	5.59
	600	6.33	0.04	6.12	0.10
	2000	5.65	0.02	5.81	0.06
PEcbz-Fur	11	6.01	0.05	5.32	0.03
	600	5.53	0.02	5.06	0.06
	2000	5.40	0.02	4.97	0.09

As it observed from the Fig. 4.8, the dielectric constant increases with increasing temperature for the PEcbzTer, PEcbz-Ant samples (Fig. 4.8 3a and b), while the $\varepsilon'_{\mathrm{r}}$ values of PEcbz-Fur decrease with temperature (Fig. 4.8 3c). The increase observed in $\varepsilon'_{\mathrm{r}}$ values with temperature can be explained on the basis that the contribution of the charge carriers to the polarization is weak if they are not in the direction of the field and this affects the change of $\varepsilon'_{\mathrm{r}}$ with temperature. Thus, the increase in temperature results in sufficient thermal excitation energy obtained by the bound charge carriers, which enhance the polarization leading to the increase in the dielectric constant [192].

In order to compare the behavior of the dielectric constant for the three materials at R.T = 30°C and 120°C at various frequencies we presented them in table 4.1. From the table it is observed that the dielectric constant of REcbz-Ter has higher values when compared with PEcbz-Fur and PEcbzAnt. These results showed that changing the substitute lead to a variation in dielectric constant, whereas replace the Furan part with Terphenyl, brought the dielectric constant up to 11, which is similar to the value for pure p(DAthsub). These values can be considered high compared with many other organic compounds [193]. Table 4.2 shows the values of dielectric constant of our copolymer PEcbz-Ter compared with other values in the literature. The dielectric constant is higher than that of many other aromatic organic polymers, making it a good semiconductor material. At the same time, these values are low compared

to the results recorded in [194]. This helps to solve a major limitation of organic semiconductors which is their limited exciton (hole-electron pair) lifetime of 1 ns and exciton diffusion length of 10 nm. The Photo-generated holes and electrons experience a strong Coulombic interaction due to low values of relative permittivity in organic semiconductors ($\varepsilon'_{\mathrm{r}} =$ 3-4), resulting in significant recombination losses. In our case, this drawback could be overcome with the dielectric primitivity obtained which reaches 8.67 for PEcbz-Ter, resulting in a reduction in the response time in the material.

4.5.3 Dielectric Loss

The imaginary part of the permittivity as a function of frequency at different temperatures calculated by using Eq. 4.1 is shown in Fig. 4.9. The behavior of dielectric loss is similar to the real part of the permittivity, with an anomaly exception at room temperature, which does not have a presently understood origin. The dielectric loss obtained increases with increasing temperature and has a rapid decrease at low frequencies while being almost independent at high frequencies and less sensitive to temperature.

In Fig. 4.9 the factor loss behavior as a function of frequency can be explained by the fact that ions migrate within the materials at low frequencies. The values of dielectric loss at moderate frequencies are due to the contribution of ion jump and conduction loss of ion migration, as well the ion polarization loss. At high frequency, ion vibrations may be the only source of the dielectric loss, so $\varepsilon''_{\mathrm{r}}$ is frequency-independent. Differently, the loss factor decreases with increasing frequency and expressed as follows according to the CBH model:

$$\varepsilon''_r = A'\omega^m \tag{4.1}$$

where A′ is a constant and m is the frequency power factor. From the plot of $\ln(\varepsilon''_r)$ vs. $\ln(\omega)$, Fig. 4.10 we can calculate the factor m and it is the negative slope of the lines. The losses that are attributed to the conduction presumably involve the migration of ions over large distances. This motion is the same as that occurring under DC conditions. The ions jump over the highest barriers in the network. As the ions move, they give some of their energy to the lattice as heat, which accounts for the dissipation of electrical energy as heat.

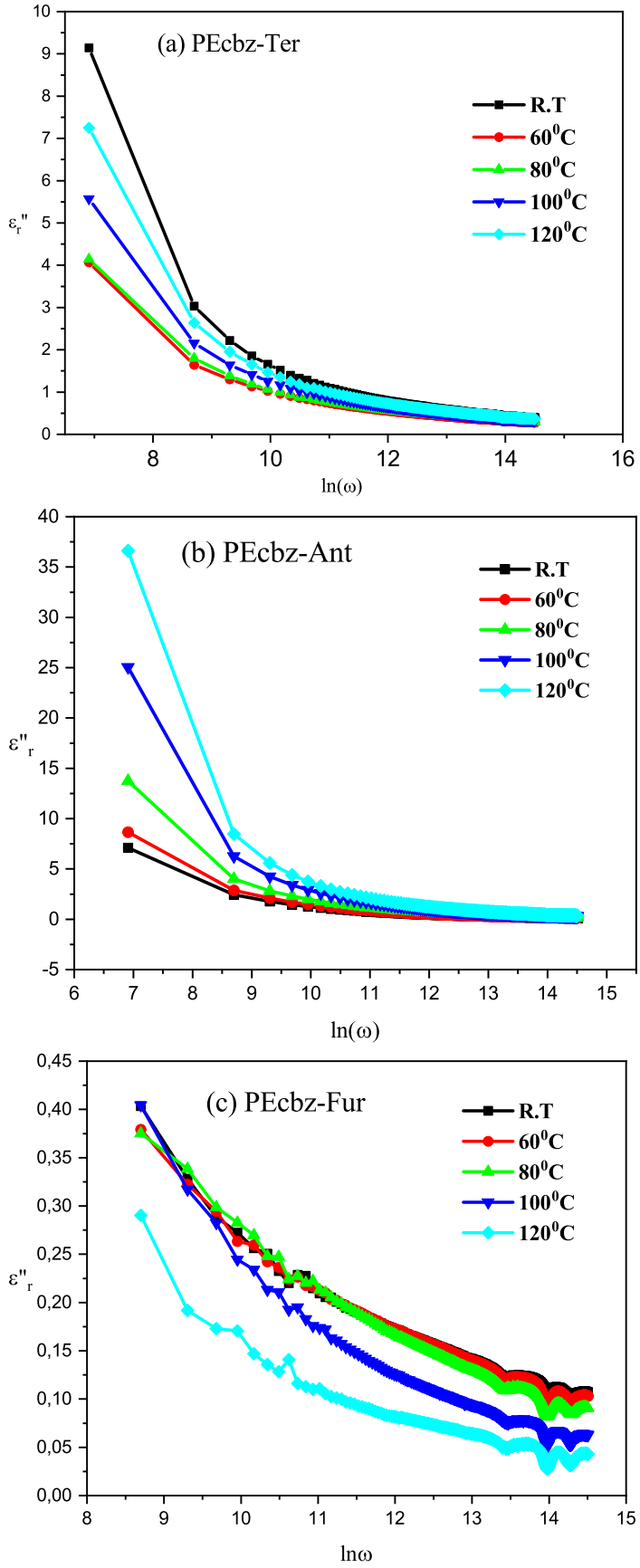


Fig. 4.9 Dielectric loss vs. frequency of a) PEcbz-Ter, b) PEcbz-Ant and c) PEcbz-Fur at different temperatures.

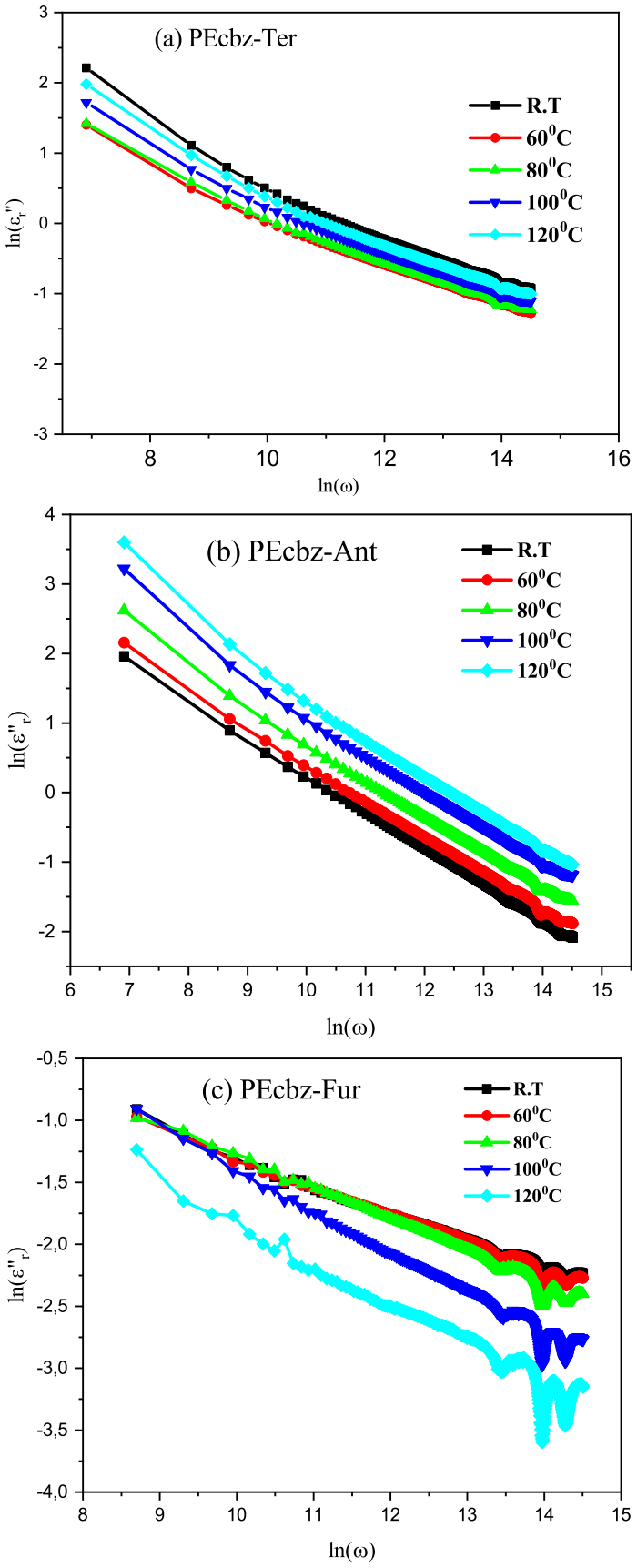


Fig. 4.10 $\ln(\varepsilon_r'')$ vs. frequency of a) PEcbz-Ter, b) PEcbz-Ant and c) PEcbz-Fur at different temperatures.

Furthermore, loss factor results for PEcbz-Ter, PEcbz-Ant and PEcbz-Fur at 11 kHz, 600 kHz and 2000 kHz are listed in Table 4.1 at R.T and 120°C. It is clear from the data presented in the table that as far as frequency increasing, the dipolar polarization effect will tend to zero, then the dielectric loss factor tends to be very low, as shown in Table 4.1. Through the values of the dispersion factors and real dielectric constant we found that the loss factor of all compounds are below 1% which make them useful and acceptable for many energy storage applications.

4.5.4 AC Conductivity

The frequency dependence of the AC conductivity is obtained by the equation :

$$\sigma_{ac} = \varepsilon_0 \varepsilon_r'' \omega. \tag{4.2}$$

The plot of conductivity as a function of frequency in the range of 1 kHz to 2 MHz at different temperatures is shown in Fig. 4.11. It is found for all compounds that σ_{ac} at the studied temperatures slowly increases with an increase in the frequency, especially in the range up to 105 Hz. After that a small slope is observed at higher frequencies, which reveals that the σ_{ac} is proportional to mobility and carrier concentrations. The low value of electrical conductivity is the effect of decrease in mobility of the charge carriers due to ionic size, which leads to the change in electronic band structure.

The increase in the AC conductivity at high frequencies could be due to the hopping mechanism. A model that was originally proposed by Pike [151] in order to calculate the frequency dependent conductivity in scandium oxide films, and then extended by Elliott [195] in the study of chalcogenide glasses. This model suggests a random distribution of the localized states and the motion of electronic charge carriers through a rigorous relaxation time between a pair consisting of two localized states. After changing the furan with the terphenyl and anthracene the conductivity was found to change from 10^{-6} to 10^{-5} S/cm, at high frequencies. Since the conductivity seems to depend upon the linkage in the backbone bonding and since phenyl-phenyl bond exhibits greater orbital overlap between phenyl groups, this linkage may well be the structural parameter responsible for the slight differences in conductivity.

The effect of temperature on the AC conductivity at several frequencies for all copolymers were studied. Fig.4.12 represents the results of PEcbz-Ter sample as an example. The figure shows the conductivity plot as function of 1000 K/T in the temperature range from R.T to 120°C at 1 kHz, 10 kHz 50 kHz and 100 kHz 300 kHz,

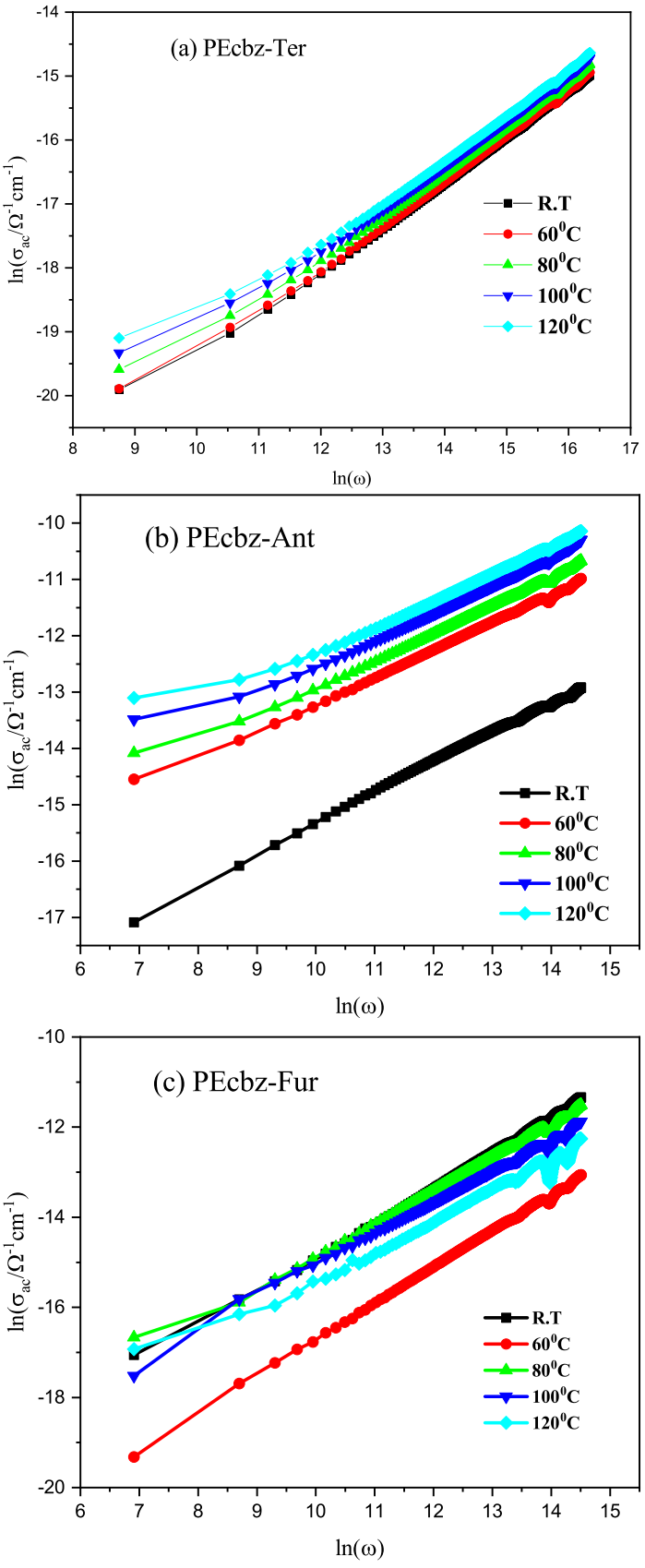


Fig. 4.11 AC conductivity vs. frequency of a) PEcbz-Ter, b) PEcbz-Ant and c) PEcbz-Fur at different temperatures.

Table 4.2 Dielectric constant ε'_r, and conductivity σ_{ac}, $\left(\Omega^{-1} \cdot \text{cm}^{-1}\right)$ for PEcbz -Ter, $\text{Ph}-\text{PHQ}$, and P -terphenyl..

Coump	Freq (kHz)	ε'_r at R.T	ε'_r at 120°C	σ_{ac} at R.T	σ_{ac} at 120°C
PEcbz-Ter	11	8.67	9.54	7.93×10^{-7}	1.35×10^{-6}
	600	7.03	7.26	1.28×10^{-5}	1.80×10^{-5}
	2000	6.76	6.91	3.09×10^{-5}	4.39×10^{-5}
Ph-PHQ [196]	0.5	3.92	–		–
	10	2.2	–	2.2×10^{-10}	–
	5000	2	–	1.4×10^{-8}	–
P-Terphenyl [197]	0.15	6670	–	5.5×10^{-5}	–
	600	4412	–	–	–
	1000	4412	–	–	–

800 kHz, and 1000 kHz. From the figure it can be observed that the conductivity slightly changes till 50°C then increases with increase in temperature. This increase at high temperature could be elucidated on the basis that temperature affects the hydrogen bond strength in the molecules, high temperatures lead to the movements of thermally excited carriers from energy levels within the band gap. While the slight changes observed at low temperatures are dominated by the hopping of carriers between localized states. As it observed from the figure that the conductivity has a strong dependence on the frequency where it is increase with increasing frequency. The value of σ_{ac} versus temperature can be affected by the substitute in our copolymers, as shown in Fig. 4.12 (b) at 10 kHz where PEcbz -Ter has the higher value compared with PEcbz-Fur which has the lowest. We report in table 4.2 the values of AC conductivity at several temperatures and frequencies for comparison with other values reported in the literature. We defined a new parameter as a figure of merit (F) which combined the AC conductivity and dielectric constant Eq. 4.3 related to the response time, which represents the relationship between the dielectric permittivity and the AC conductivity [198]. The higher its value, the more suitable the material for solar cell applications (Table 4.3).

$$F = \frac{\sigma_{\text{ac}}}{\varepsilon'_r} \tag{4.3}$$

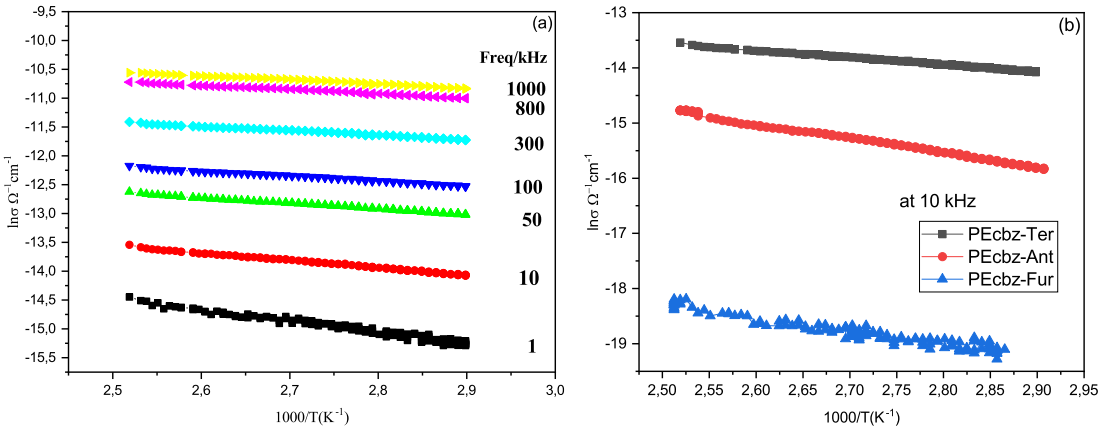


Fig. 4.12 Ac conductivity as a function of temperature for: a) PEcbz-Ter at different frequencies and b) the PEcbz-Ter, PEcbz-Ant and PEcbz-Fur at 10 kHz.

Table 4.3 The ratio F at R.T and 120°C for PEcbz-Ter, Ph-PHQ, and P-terphenyl.

Coumpound	$F\left(\Omega^{-1}\cdot\mathrm{cm}^{-1}\right)$ at R.T	$F\left(\Omega^{-1}\cdot\mathrm{cm}^{-1}\right)$ at 120°C
PEcbz-Ter	9.15×10^{-8}	1.42×10^{-7}
	1.82×10^{-6}	2.48×10^{-6}
	4.57×10^{-6}	6.36×10^{-6}
Ph-PHQ [196]	–	–
	1×10^{-10}	–
	7×10^{-9}	–
P-Terphenyl [197]	8.38×10^{-9}	–
	–	–
	–	–

4.5.5 Exponent "s"

A quick reminder of the power-low exponent "s" which is already mentioned in the theoretical background, the correlated barrier-hopping CBH model anticipated as being both temperature-and frequency-dependent and "s" should decrease with increasing temperature. The behavior of "s" as a function of temperature can provide a clear idea of which model the material follows. In order to confirm what has been said in the AC conductivity section about the behavior that follows our materials, we plotted the exponent "s" as a function of temperature. Values of "s" are calculated from the slope of the linear $\ln(\sigma_{\mathrm{ac}})$ vs. $\ln(\omega)$, as depicted in Fig. 4.13. For PEcbz-Ter and PEcbz-Ant the exponent decreases with increasing temperature; therefore, among all the models discussed in the theoretical background, CBH is the appropriate model for the conduction in our material. The exponent "s" of PEcbz-Fur has a different behavior.

At low temperature, the CBH is the dominant model, subsequently "s" is predicted to increase as temperature increases which is the polaron tunneling model (SPT).

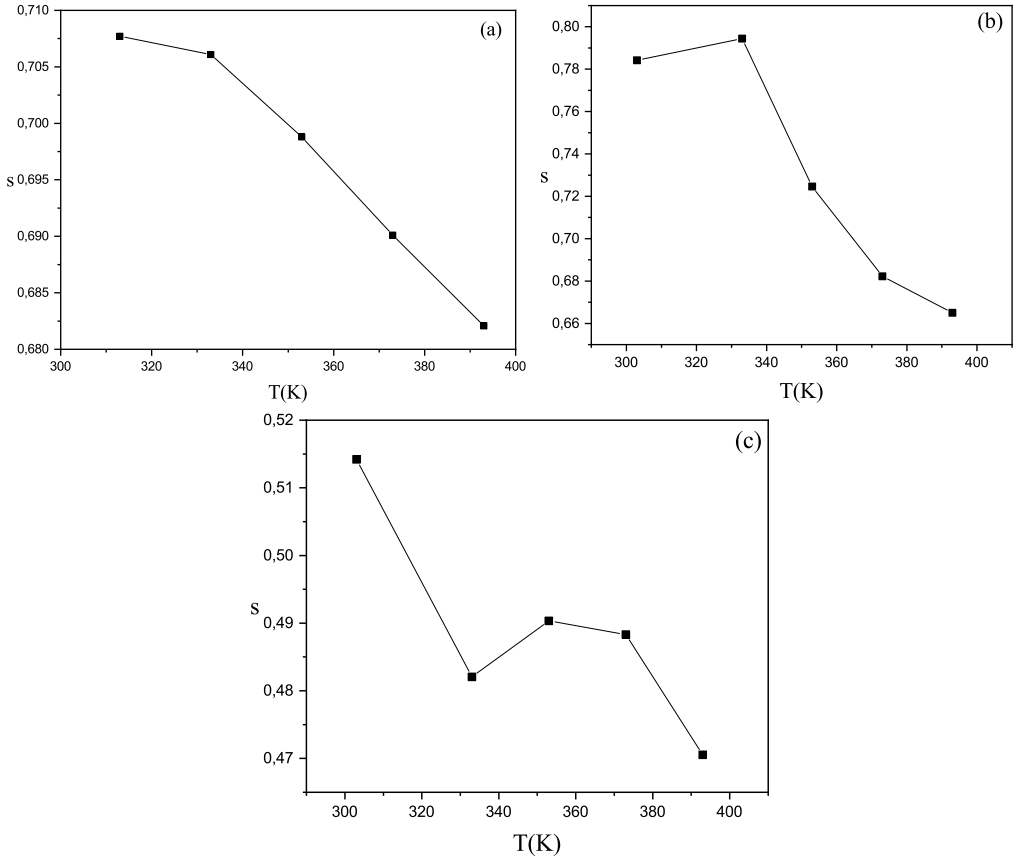


Fig. 4.13 Exponent "s" as a function of temperature of a) PEcbz-Ter, b) PEcbz-Ant and c) PEcbz-Fur.

4.5.6 Activation Energy

Fig. 4.14 shows the values of activation energy as function of ln(w). The values of activation energy of our samples calculated as a function of frequency from the slope of the straight lines in Fig. 4.12. Activation energy E_a decreases with increasing frequency; this could be due to the applied field frequency that enhances the electronic jumps between the localized states.

Moreover, in this study, the activation energies were determined from the slope of the AC conductivity at 10 kHz, (0.043 eV, 0.099 eV and 0.07 eV) for PEcbz-Ter, PEcbz-Ant and PEcbz-Fur respectively. The low values of active energy are in agreement with the hopping model in our copolymers. This behavior is similar to the conduction mechanism in plasma polymerized aniline thin films [199]. The results of the PEcbz-Ter

sample show favorable values more than PEcbz-Ant and PEcbz-Fur. This variation could be due to the difference in the composition according to the results shown in X-ray diffraction and scanning electron microscopy.

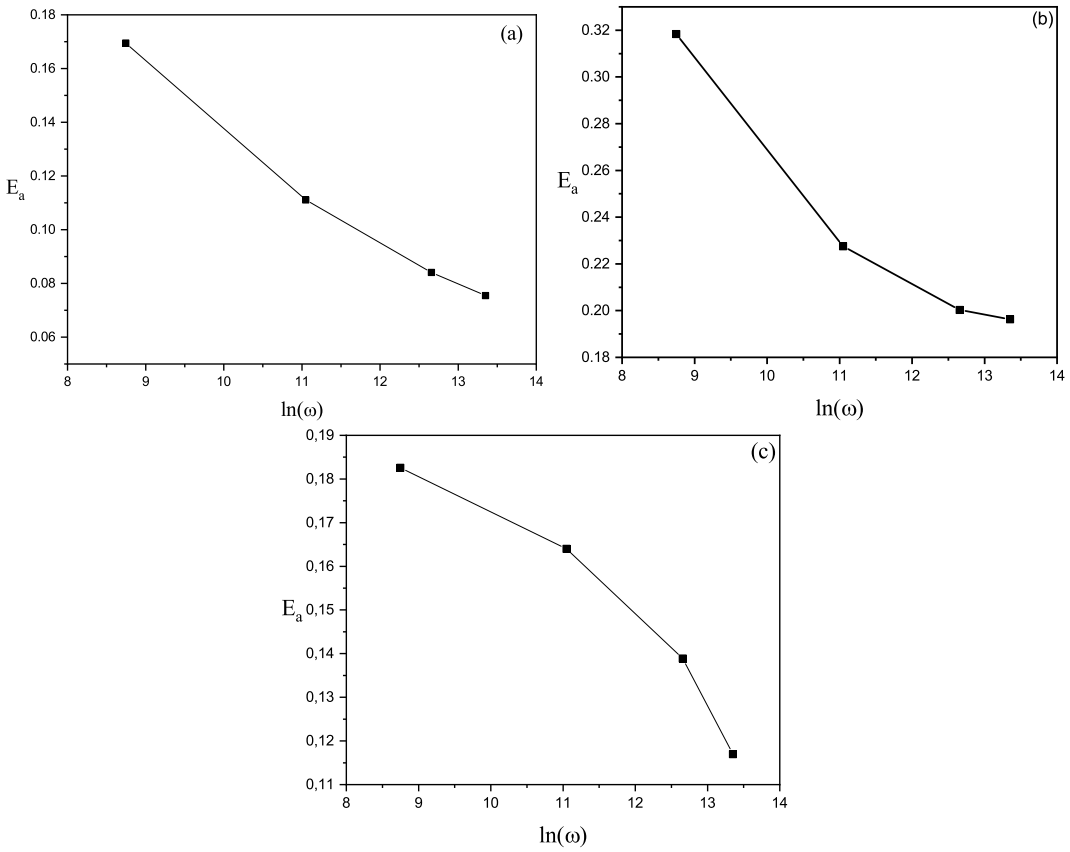


Fig. 4.14 Activation energy vs. frequency of a) PEcbz-Ter, b) PEcbz-Ant and c) PEcbz-Fur.

4.6 Conclusion

We performed an X-ray diffraction and scanning electron microscopy analysis, which allowed us to visualize the morphology and to confirm the crystallinity of each compound. The absorption technique has confirmed that our copolymers absorb both in the visible and UV-Vis region. The dielectric and electrical properties of our copolymers have been obtained by impedance spectroscopy. The dielectric constant values for all compounds are high, which solves a major problem in organic materials related to their limited exciton lifetime (hole-electron pair) of about 1 ns and diffusion length of exciton of

about 10 nm. According to the power law exponent values obtained in this study, the hopping mechanism controls the conductivity behavior of our materials.

Summary and Future Work

The research fields that have developed around conjugated polymers represent many exciting new frontiers. Polymers offer a broad range of attractive properties that have gained the interest of many companies and fueled the rapid progress of conjugated polymer research. Applications of conjugated polymers in low-cost electronics have become a reality, and the commercial development of polymer-based solar cells is on the brink of occurring. This thesis has used a computational modeling approach alongside experimental techniques to investigate organic materials. First, we carried out a study on Alkyl-substituted Oligopyrrole (DOTP), (DH4P), and (ddoD4P) integrating Density-functional Theory. The optoelectronic properties are improved for large or doped oligomeric chains. Comparing the results obtained for the various compounds makes it possible to discover the effect of the transition from the DOTP to DH4P and the doping on the structure and the electronic properties. The quinoid contribution appears strongly in the doped structures, and the increase in size is accompanied by a decrease in the gap and high stability. Investigation of substituted alkyl groups at sites 3 of the pyrrole cycle suggests that R3 = $C_{12}H_{25}$ and R4 substitution leads to the HOMO and LUMO stabilization and reduces gap energy. The absorption was also influenced by substitution, then a redshift is observed from ddoD4P to DH4P.

Then, the geometric and optoelectronic properties of eight dyes Di (i=1,8) were investigated. Different functionals were employed to choose the convenient functional correlated with the experimental results. Thus, CAM-B3LYP functional was in good agreement with the experimental results. We examined the role of different electron-donor groups in tuning the geometries, electronic structures, and optical properties based on the obtained results. We also discussed the dependency of the photovoltaic parameters (open-circuit voltage (V_{oc}), oxidation potential energy, and electron injection force) with electron-donor group changing. Overall, the selenophene-based dyes show good optoelectronic properties, with an energy gap of less than 2.68 eV for all the studied compounds. The calculated values of the V_{oc} of our dyes are sufficient for possible efficient electron injection from the donor to the acceptor. In particular, D8

possessing triphenylamine as a donor group shows promising electronic and photovoltaic properties with respect to other dyes. Therefore it can be suggested as a good photosensitizer for use in DSSC. This theoretical approach may be useful in designing efficient new molecules for dye-sensitized solar cells and has also been a practical confirmation of the use of DFT for our proposed new materials. The last sets of materials that were theoretically studied in this thesis were the three proposed new materials based on ethylcarbazole. All the copolymers showed good electronic properties. However, two specific ones (PEcbz-Ter and PEcbz-Ant) exhibit more advantageous properties, making them suitable as semiconductor materials, particularly for organic field-effect transistors.

Further, the experimental part using characterization techniques and impedance spectroscopy was employed. We carried out The dielectric proprieties and AC conductivity of carbazole-based materials. PEcbz-Ter, PEcbz-Fur, and PEcbz-Ant were studied as a function of frequency (from 1 kHz to 2 MHz) and temperature (from RT to 120°C). X-ray has been done and shows crystalline regions in our polymer. UV-vis absorption provided us valuable insights and showed a broad absorption with a low bandgap. It was found that the dielectric constant decreases with increasing frequency for all samples but increases with increasing temperature for PEcbz-Ter and PEcbzAnt. The dielectric loss values were found to be 0.05, 0.14, and 0.24 for the PEcbz-Fur, PEcbz-Ter, and PEcbzAnt, respectively, at 11 kHz, which are below 1 percent and make them acceptable for many energy storage applications. The AC conductivity appears to increase with increasing frequency and a decrease with rising temperature, a different behavior recorded for PEcbz-Ter related to temperature. The appropriate model for PEcbz-Ter and PEcbzAnt was the correlated barrier-hopping (CBH) model for PEcbz-Ter and PEcbzAnt, although PEcbz-Fur behaves according to the (CBH) model at low temperature and polaron tunneling model (SPT) at high temperature. Activation energy decreases with increasing frequency. Those results are promising compared with others in the literature; this could be exploited to investigate more in dielectric and electric properties of organic materials.

In light of the promising results of this work, we first intend to study new organic materials both theoretically and experimentally using different approaches and techniques. Second, we are involved in the project FIRE at the Surface Laboratory in the National Institute of Nuclear Physics, Rome. In this project, we will develop innovative radiation detectors based on Organic Thin-Film Transistors (OTFTs) in both direct and indirect configurations using the organic materials studied in this thesis PEcbz-Ter, PEcbzAnt, and PEcbz-Fur. We aim at detecting different radiation fields (X and

gamma-rays, charged particles, and neutrons) by tuning the optical and electrical properties of organic materials through their molecular structure. As a final result, FIRE will develop, implement and validate in relevant environment flexible, low-power 2D pixel detector matrices (up to 3x3 pixels) equipped with read-out electronics. We propose to develop: 1) indirect detectors based on Organic Photo Transistors (OPTs) coupled with plastic scintillators. 2) direct X-ray detectors based on semiconducting organic thin films OTFTs. The proof of concept of such detectors was recently demonstrated. We will develop novel X- and gamma-ray OTFT detectors by appropriately selecting novel and more efficient organic molecules.

References

[1] Biswanath Mukherjee. Flexible organic n-channel phototransistor and integrated logic devices. *Optik*, 139:48–55, 2017.

[2] Huikang Luo, Junqi Lai, Cheng Wang, and Qi Chen. Understanding the effects of the energy band alignment at the donor/acceptor interface on the open circuit voltage of organic photovoltaic devices. *Chemical Physics Letters*, 711:113–117, 2018.

[3] Hugo Bronstein, Zhuoying Chen, Raja Shahid Ashraf, Weimin Zhang, Junping Du, James R Durrant, Pabitra Shakya Tuladhar, Kigook Song, Scott E Watkins, Yves Geerts, et al. Thieno thiophene-diketopyrrolopyrrole-containing polymers for high-performance organic field-effect transistors and organic photovoltaic devices. *Journal of the American Chemical Society*, 133(10):3272–3275, 2011.

[4] Tomotsugu Takaya, Melaku Dereje Mamo, Makoto Karakawa, and Yong-Young Noh. Donor unit effect on dpp based organic field-effect transistor performance. *Dyes and Pigments*, 158:306–311, 2018.

[5] Diana K Sagdullina, Iliya E Kuznetsov, Alexander V Akkuratov, Lidiya I Kuznetsova, Sergey I Troyanov, and Pavel A Troshin. New alternating thiophene-benzothiadiazole electron donor material for small-molecule organic solar cells and field-effect transistors. *Synthetic Metals*, 250:7–11, 2019.

[6] Gen-Wen Hsieh, Zong-Rong Lin, Chun-Yi Hung, Sheng-Yu Lin, and Chii-Rong Yang. Graphene-induced enhancement of charge carrier mobility and air stability in organic polythiophene field effect transistors. *Organic Electronics*, 54:27–33, 2018.

[7] Irma Slowik, Hartmut Fischer, Axel, Simone Lenk, Sebastian Reineke, and Karl Leo. Novel organic light-emitting diode design for future lasing applications. *Organic Electronics*, 48:132–137, 2017.

[8] Chuan Zhang, Xianfeng Qiao, Zhenlin Yang, Hongmei Zhang, and Dongge Ma. Highly efficient inverted organic light-emitting diodes with organic pn junction as electron injection layer. *Organic Electronics*, 58:185–190, 2018.

[9] Jos Carlos Germino, Jilian Nei de Freitas, Raquel Aparecida Domingues, Fernando Junior Quites, Marcelo Meira Faleiros, and Teresa Dib Zambon Atvars. Organic light-emitting diodes based on pvk and zn (ii) salicylidene composites. *Synthetic Metals*, 241:7–16, 2018.

[10] Amr M Obeidat, Mohammad A Gharaibeh, and Mazin Obaidat. Solid-state supercapacitors with ionic liquid gel polymer electrolyte and polypyrrole electrodes for electrical energy storage. *Journal of Energy Storage*, 13:123–128, 2017.

[11] Dimberu G Atinafu, Wenjun Dong, Xiubing Huang, Hongyi Gao, and Ge Wang. Introduction of organic-organic eutectic pcm in mesoporous n-doped carbons for enhanced thermal conductivity and energy storage capacity. *Applied energy*, 211: 1203–1215, 2018.

[12] Tyler B Schon, Bryony T McAllister, Peng-Fei Li, and Dwight S Seferos. The rise of organic electrode materials for energy storage. *Chemical Society Reviews*, 45(22):6345–6404, 2016.

[13] N Bouzayen, H Sadki, M Mbarek, M Bouachrine, J Bennani, MN, and K Alimi. Synthesis, characterization, dft and td-dft studies of novel carbazole-based copolymer used in high efficient dye-sensitized solar cells. *Polymer Testing*, 66: 78–86, 2018.

[14] Yunhao Cai, Xiaonan Xue, Guangchao Han, Zhaozhao Bi, Bingbing Fan, Tao Liu, Dongjun Xie, Lijun Huo, Wei Ma, Yuanping Yi, et al. Novel π-conjugated polymer based on an extended thienoquinoid. *Chemistry of Materials*, 30(2): 319–323, 2018.

[15] Duygu Keles, Mert Can Erer, Eda Bolayir, Sevki Can Cevher, Gonul Hizalan, Levent Toppare, and Ali Cirpan. Conjugated polymers with benzothiadiazole and benzotriazole moieties for polymer solar cells. *Renewable Energy*, 139:1184–1193, 2019.

[16] Zakaria Mohyi Eddine Fahim, Si Mohamed Bouzzine, Youssef Ait Aicha, Mohammed Bouachrine, and Mohamed Hamidi. The bridged effect on the geometric, optoelectronic and charge transfer properties of the triphenylamine–bithiophene-based dyes: a dft study. *Research on Chemical Intermediates*, 44(3):2009–2023, 2018.

[17] Samuel I Stupp and Liam C Palmer. Supramolecular chemistry and self-assembly in organic materials design. *Chemistry of Materials*, 26(1):507–518, 2014.

[18] Zaisha Mao and Chao Yang. Computational chemical engineering–towards thorough understanding and precise application. *Chinese journal of chemical engineering*, 24(8):945–951, 2016.

[19] Yafei Dai, Sugata Chowdhury, and Estela Blaisten-Barojas. Density functional theory study of the structure and energetics of negatively charged oligopyrroles. *International Journal of Quantum Chemistry*, 111(10):2295–2305, 2011.

[20] AH El-Shazly and AA Wazzan. Using polypyrrole coating for improving the corrosion resistance of steel buried in corrosive mediums. *Int. J. Electrochem. Sci*, 7:1946–1957, 2012.

[21] Sachetan M Tuladhar, Marc Sims, James Kirkpatrick, Robert C Maher, Amanda J Chatten, Donal DC Bradley, Jenny Nelson, Pablo G Etchegoin, Christian B Nielsen, Philippe Massiot, et al. Influence of alkyl chain length on charge transport in symmetrically substituted poly (2, 5-dialkoxy-p-phenylenevinylene) polymers. *Physical Review B*, 79(3):035201, 2009.

[22] T Mestiri, M Chemek, J Rouabeh, and K Alimi. Dft and td-dft modeling of new carbazole-based oligomers for optoelectronic devices. *Computational Condensed Matter*, 4:23–31, 2015.

[23] Lili Liu, Zhongjie Ren, Chengyi Xiao, Huanli Dong, Shouke Yan, Wenping Hu, and Zhaohui Wang. Surface-induced highly oriented perylo selenophene thin films for high performance organic field-effect transistors. *Organic Electronics*, 35:186–192, 2016.

[24] Vellaiappillai Tamilavan, Jong Baek Park, In-Nam Kang, Do-Hoon Hwang, and Myung Ho Hyun. Benzodithiophene-based polymers containing novel electron accepting selenophene-incorporated pyrrolo pyrrole-1, 3-dione units for highly efficient thin film transistors and polymer solar cells. *Synthetic metals*, 198: 230–238, 2014.

[25] Xiaochen Wang, Jianming Huang, Keisuke Tajima, Bo Xiao, and Erjun Zhou. An amorphous n-type polymer based on perylenediimide and selenophene for all-polymer solar cells application. *Materials Today Communications*, 4:16–21, 2015.

[26] Vellaiappillai Tamilavan, Jong Baek Park, In-Nam Kang, Do-Hoon Hwang, and Myung Ho Hyun. Benzodithiophene-based polymers containing novel electron accepting selenophene-incorporated pyrrolo pyrrole-1, 3-dione units for highly efficient thin film transistors and polymer solar cells. *Synthetic metals*, 198: 230–238, 2014.

[27] Ji Hyung Lee, Gi Eun Park, Suna Choi, Dae Hee Lee, Hyun Ah Um, Jicheol Shin, Min Ju Cho, and Dong Hoon Choi. Effect of the thiophene and selenophene moiety in regular terpolymers on the performance of thin film transistors and polymer solar cells. *Polymer*, 94:43–52, 2016.

[28] Xiaowei Zhang, Qi Wang, Ziqi Liang, Miaomiao Li, and Yanhou Geng. Low-bandgap non-fullerene acceptors based on selenophene π spacer and alkylated indaceno dithiophene for organic solar cells. *Organic Electronics*, 69:200–207, 2019.

[29] Shunsuke Tamba, Ryosuke Fujii, Atsunori Mori, Kohjiro Hara, and Nagatoshi Koumura. Synthesis and properties of seleno-analog mk-organic dye for photovoltaic cells prepared by c–h functionalization reactions of selenophene derivatives. *Chemistry letters*, 40(9):922–924, 2011.

[30] Shu-Zhen Tan, Yan-Jun Hu, Fu-Chun Gong, Zhong Cao, Jiao-Yun Xia, and Ling Zhang. A novel fluorescence sensor based on covalent immobilization of 3-amino-9-ethylcarbazole by using silver nanoparticles as bridges and carriers. *Analytica chimica acta*, 636(2):205–209, 2009.

[31] Selma Bal and Joseph Donald Connolly. Synthesis, characterization, thermal and catalytic properties of a novel carbazole derived azo ligand and its metal complexes. *Arabian Journal of Chemistry*, 10(6):761–768, 2017.

[32] Soon Ok Jeon, Kyoung Soo Yook, Hyo Suk Son, and Jun Yeob Lee. An ethylcarbazole based phosphine oxide derivative as a host for deep blue phosphorescent organic light-emitting diode. *Journal of luminescence*, 130(11):2238–2241, 2010.

[33] Ahmed Iraqi and Isao Wataru. Preparation and properties of 2, 7-linked n-alkyl-9 h-carbazole main-chain polymers. *Chemistry of materials*, 16(3):442–448, 2004.

[34] Milind Arbatti, Xiaobing Shan, and Z-Y Cheng. Ceramic–polymer composites with high dielectric constant. *Advanced Materials*, 19(10):1369–1372, 2007.

[35] Wei Wan, Junrong Luo, Chun-e Huang, Jian Yang, Yongbao Feng, Wen-Xiang Yuan, Yuejun Ouyang, Dizhao Chen, and Tai Qiu. Calcium copper titanate/polyurethane composite films with high dielectric constant, low dielectric loss and super flexibility. *Ceramics International*, 44(5):5086–5092, 2018.

[36] Paul Brochu and Qibing Pei. Dielectric elastomers for actuators and artificial muscles. In *Electroactivity in Polymeric Materials*, pages 1–56. Springer, 2012.

[37] Yuping Shi, Limin Huang, Ai Kah Soh, George J Weng, Shuangyi Liu, and Simon AT Redfern. A scaling law for distinct electrocaloric cooling performance in low-dimensional organic, relaxor and anti-ferroelectrics. *Scientific reports*, 7 (1):1–9, 2017.

[38] Erik W Thulstrup, Jens Spanget-Larsen, and R Gleiter. The electronic structure of p-terphenyl, 3, 6-diphenyl-pyridazine and 3, 6-diphenyl-s-tetrazine: Photoelectron and polarized absorption spectra. *Molecular Physics*, 37(5):1381–1395, 1979.

[39] Eizi Morikawa, Yasuo Isono, and Masahiro Kotani. Generation and recombination of charge carriers in p-terphenyl crystal. photoionization of singlet exciton. *The Journal of chemical physics*, 78(5):2691–2695, 1983.

[40] S Selvakumar, R Murugaraj, E Viswanathan, S Sankar, and K Sivaji. Dielectric properties and relaxation mechanism of organic trans-stilbene and p-terphenyl molecular crystals using impedance spectroscopy. *Journal of Molecular Structure*, 1056:152–156, 2014.

[41] CS Mishra and G Palai. Optical nonlinearity in germanium and silicon semiconductor vis-a-vis temperature and wavelengths for sensing application. *Optik*, 137: 37–44, 2017.

[42] Yang Yang, Ngoc Duy Pham, Disheng Yao, Huaiyong Zhu, Prasad Yarlagadda, and Hongxia Wang. Inorganic p-type semiconductors and carbon materials based hole transport materials for perovskite solar cells. *Chinese Chemical Letters*, 29 (8):1242–1250, 2018.

[43] Norani Ab Manaf and Abdul Manaf Hashim. Properties of rapid thermal oxidized p-type germanium and its metal-oxide-semiconductor capacitor structure. *Materials Today: Proceedings*, 7:744–753, 2019.

[44] Onkar Mangla and Savita Roy. Synthesis of gallium arsenide nanostructures for solar cell applications. *Materials Letters*, page 128036, 2020.

[45] Yuchen Ma and Michael Rohlfing. Optical excitation of deep defect levels in insulators within many-body perturbation theory: the f center in calcium fluoride. *Physical Review B*, 77(11):115118, 2008.

[46] Yaqi Wang, Jiakun Wu, Yu Yan, Lu Li, Ping Lu, Jiunian Guan, Nan Lu, and Xing Yuan. Black phosphorus-based semiconductor multi-heterojunction tio2-bivo4-bp/rp film with an in situ junction and z-scheme system for enhanced photoelectrocatalytic activity. *Chemical Engineering Journal*, page 126313, 2020.

[47] Guowu Tang, Qi Qian, Xin Wen, Guanxiang Zhou, Xiaodong Chen, Min Sun, Dongdan Chen, and Zhongmin Yang. Phosphate glass-clad tellurium semiconductor core optical fibers. *Journal of Alloys and Compounds*, 633:1–4, 2015.

[48] Yunyu Cai, Yixing Ye, Pengfei Li, Yonghui Zhou, Jun Liu, Zhenfei Tian, Zhaorong Yang, and Changhao Liang. Pressure induced semiconductor-metallic transition of selenium nanoribbons generated by laser ablation in liquids. *Applied Surface Science*, 473:564–570, 2019.

[49] YU Peter and Manuel Cardona. *Fundamentals of semiconductors: physics and materials properties*. Springer Science & Business Media, 2010.

[50] JS Blakemore. Materials requirements for gaas for optoelectronic applications. In *Processing of Guided Wave Optoelectronic Materials I*, volume 460, pages 14–21. International Society for Optics and Photonics, 1984.

[51] Oksana Ostroverkhova. *Handbook of Organic Materials for Electronic and Photonic Devices*. Woodhead Publishing, 2018.

[52] Ajeet Kaushik. Advances in nanosensors for biological and environmental analysis: Book review. akash deep, sandeep kumar (eds.); elsevier 2019; isbn: 978-0-12-817456-2, 2019.

[53] Thomas Stegmann, John A Franco-Villafane, Yenni P Ortiz, Ulrich Kuhl, Fabrice Mortessagne, and Thomas H Seligman. Microwave emulations and tight-binding calculations of transport in polyacetylene. *Physics Letters A*, 381(1):24–29, 2017.

[54] Brenden McDearmon, Zachariah A Page, Michael L Chabinyc, and Craig J Hawker. Organic electronics by design: the power of minor atomic and structural changes. *Journal of Materials Chemistry C*, 6(14):3564–3572, 2018.

[55] Wolfgang Brütting. Physics of organic semiconductors. *physica status solidi (a)*, 201(6):1031–1031, 2004.

[56] Carme Martínez-Domingo, Silvia Conti, Lluís Terés, Henrique Leonel Gomes, and Eloi Ramon. Novel flexible inkjet-printed metal-insulator-semiconductor organic diode employing silver electrodes. *Organic Electronics*, 62:335–341, 2018.

[57] Yerok Park, Kyu S Han, Byoung H Lee, Sangho Cho, Kwang H Lee, Seongil Im, and Myung M Sung. High performance n-type organic–inorganic nanohybrid semiconductors for flexible electronic devices. *Organic Electronics*, 12(2):348–352, 2011.

[58] Miho Tsuwaki, Takashi Kasahara, Tomohiko Edura, Shigeyuki Matsunami, Juro Oshima, Shuichi Shoji, Chihaya Adachi, and Jun Mizuno. Fabrication and characterization of large-area flexible microfluidic organic light-emitting diode with liquid organic semiconductor. *Sensors and Actuators A: Physical*, 216: 231–236, 2014.

[59] Kakaraparthi Kranthiraja, Veera Murugan Arivunithi, Um Kanta Aryal, Ho-Yeol Park, Woosum Cho, Junyoung Kim, Saripally Sudhaker Reddy, Hyung-Kook Kim, In-Nam Kang, Myungkwan Song, et al. Efficient and hysteresis-less perovskite and organic solar cells by employing donor-acceptor type π-conjugated polymer. *Organic Electronics*, 72:18–24, 2019.

[60] J Tsukamoto. Recent advances in highly conductive polyacetylene. *Advances in Physics*, 41(6):509–546, 1992.

[61] Richard D McCullough. The chemistry of conducting polythiophenes. *Advanced Materials*, 10(2):93–116, 1998.

[62] Art F Diaz and Juan I Castillo. A polymer electrode with variable conductivity: polypyrrole. *Journal of the Chemical Society, Chemical Communications*, 9: 397–398, 1980.

[63] Akheel A Syed and Maravattickal K Dinesan. Polyaniline—a novel polymeric material. *Talanta*, 38(8):815–837, 1991.

[64] Jessica M Torres, Chengqing Wang, E Bryan Coughlin, John P Bishop, Richard A Register, Robert A Riggleman, Christopher M Stafford, and Bryan D Vogt. Influence of chain stiffness on thermal and mechanical properties of polymer thin films. *Macromolecules*, 44(22):9040–9045, 2011.

[65] Ming Hui Chua, Qiang Zhu, Tao Tang, Kwok Wei Shah, and Jianwei Xu. Diversity of electron acceptor groups in donor–acceptor type electrochromic conjugated polymers. *Solar Energy Materials and Solar Cells*, 197:32–75, 2019.

[66] GF Musso, G Dellepiane, C Cuniberti, M Rui, and A Borghesi. Electronic structure of mixed quinoid/aromatic thiophene copolymers. *Synthetic metals*, 72 (3):209–215, 1995.

[67] Przemyslaw Ledwon. Recent advances of donor-acceptor type carbazole-based molecules for light emitting applications. *Organic Electronics*, 75:105422, 2019.

[68] Riccardo Farchioni and Giuseppe Grosso. *Organic electronic materials: conjugated polymers and low molecular weight organic solids*, volume 41. Springer Science & Business Media, 2013.

[69] Terje A Skotheim and John Reynolds. *Conjugated polymers: theory, synthesis, properties, and characterization*. CRC press, 2006.

[70] Terje A Skotheim. *Handbook of conducting polymers*. CRC press, 1997.

[71] PJAM Stallinga. Electronic transport in organic materials: Comparison of band theory with percolation/(variable range) hopping theory. *Advanced Materials*, 23 (30):3356–3362, 2011.

[72] Michael M Fogler and Ziqiang Wang. Comment on "analytic structure of one-dimensional localization theory: Reexamining mott's law". *Physical review letters*, 86(20):4715, 2001.

[73] CC Vidyasagar, BM Muñoz Flores, VM Jiménez-Pérez, and PM Gurubasavaraj. Recent advances in boron-based schiff base derivatives for organic light-emitting diodes. *Materials today chemistry*, 11:133–155, 2019.

[74] Jérémy Le Gall, Flavien Mouillard, Trung Ngoc Le, Thi Thu Vu, Giorgio Mattana, Roberta Brayner, Samia Zrig, Vincent Noël, and B Piro. Monitoring photosynthetic microorganism activity with an electrolyte-gated organic field effect transistor. *Biosensors and Bioelectronics*, page 112166, 2020.

[75] Danish Khan, Zahid Ali, Danyal Asif, Manoj Kumar Panjwani, and Idris Khan. Incorporation of carbon nanotubes in photoactive layer of organic solar cells. *Ain Shams Engineering Journal*, 2020.

[76] Jing FangáGuo, Chun MeiáLi, Xiao LiáHu, Cheng ZhiáHuang, and Yuan FangáLi. Metal–organic framework mil-101 enhanced fluorescence anisotropy for sensitive detection of dna. *Rsc Advances*, 4(18):9379–9382, 2014.

[77] Laura G Carrascosa, Silvia Gómez-Montes, Anna Aviñó, Anna Nadal, M Pla, R Eritja, and Laura M Lechuga. Sensitive and label-free biosensing of rna with predicted secondary structures by a triplex affinity capture method. *Nucleic acids research*, 40(8):e56–e56, 2012.

[78] W Helfrich and WG Schneider. Recombination radiation in anthracene crystals. *Physical Review Letters*, 14(7):229, 1965.

[79] Rolf E Hummel. *Electronic properties of materials*. Springer Science & Business Media, 2011.

[80] Ioannis Kymissis. *Organic field effect transistors: theory, fabrication and characterization*. Springer Science & Business Media, 2008.

[81] Alrun A Günther, Michael Sawatzki, Petr Formánek, Daniel Kasemann, and Karl Leo. Contact doping for vertical organic field-effect transistors. *Advanced Functional Materials*, 26(5):768–775, 2016.

[82] Martin Weis. Organic field-effect transistors. *Encyclopedia of Physical Organic Chemistry*, pages 1–39, 2016.

[83] Yoon-Bo Shim and Jin-Hyo Park. Humidity sensor using chemically synthesized poly (1, 5-diaminonaphthalene) doped with carbon. *Journal of the Electrochemical Society*, 147(1):381, 2000.

[84] Joanna Ewa Zachara, Renata Toczyłowska, Rafał Pokrop, Małgorzata Zagórska, Artur Dybko, and Wojciech Wróblewski. Miniaturised all-solid-state potentiometric ion sensors based on pvc-membranes containing conducting polymers. *Sensors and Actuators B: Chemical*, 101(1-2):207–212, 2004.

[85] Eduardo Garcia-Breijo, Berta Gomez-Lor Perez, and Piero Cosseddu. *Organic Sensors: Materials and Applications*. Institution of Engineering and Technology, 2016.

[86] Jeonghun Kim, Jaewoo Lee, Jungmok You, Min-Sik Park, Md Shahriar Al Hossain, Yusuke Yamauchi, and Jung Ho Kim. Conductive polymers for next-generation energy storage systems: recent progress and new functions. *Materials Horizons*, 3(6):517–535, 2016.

[87] Petr Novák, Klaus Müller, KSV Santhanam, and Otto Haas. Electrochemically active polymers for rechargeable batteries. *Chemical Reviews*, 97(1):207–282, 1997.

[88] Yoshinobu Shiokawa, Hajimu Yamana, and Hirotake Moriyama. An application of actinide elements for a redox flow battery. *Journal of nuclear science and technology*, 37(3):253–256, 2000.

[89] Simon Muench, Andreas Wild, Christian Friebe, Bernhard Haupler, Tobias Janoschka, and Ulrich S Schubert. Polymer based organic batteries. *Chemical reviews*, 116(16):9438–9484, 2016.

[90] Oliver Morton. Solar energy: A new day dawning?: Silicon valley sunrise. *Nature*, 443(7107):19–23, 2006.

[91] Adolf Goetzberger, Joachim Luther, and Gerhard Willeke. Solar cells: past, present, future. *Solar energy materials and solar cells*, 74(1-4):1–11, 2002.

[92] C.R. Hebd E. Becquerel. solar cells. *Seances Acad. Sci*, 9:561, 1839.

[93] Charles E Fritts. On a new form of selenium cell, and some electrical discoveries made by its use. *American Journal of Science*, (156):465–472, 1883.

[94] Vincent Barrioz, Hari Reehal, Tim Coutts, Ken Durose, David Lane, Ian Forbes, Tom Markvart, Owain Clark, James Connolly, Stuart Boden, et al. *Materials challenges: inorganic photovoltaic solar energy*. Royal Society of Chemistry, 2014.

[95] Martin A Green, Ewan D Dunlop, Jochen Hohl-Ebinger, Masahiro Yoshita, Nikos Kopidakis, and Anita WY Ho-Baillie. Solar cell efficiency tables (version 55). *Progress in Photovoltaics: Research and Applications*, 28(1):3–15, 2020.

[96] Mariyappan Shanmugam, Chris A Durcan, and Bin Yu. Layered semiconductor molybdenum disulfide nanomembrane based schottky-barrier solar cells. *Nanoscale*, 4(23):7399–7405, 2012.

[97] Tetsuya Taima, Masayuki Chikamatsu, Raghu Nath Bera, Yuji Yoshida, Kazuhiro Saito, and Kiyoshi Yase. Insertion of thin interlayers under the negative electrode of c60 schottky-type photovoltaic cells. *The Journal of Physical Chemistry B*, 108(1):1–3, 2004.

[98] Yuhki Terao, Hiroyuki Sasabe, and Chihaya Adachi. Correlation of hole mobility, exciton diffusion length, and solar cell characteristics in phthalocyanine/fullerene organic solar cells. *Applied Physics Letters*, 90(10):103515, 2007.

[99] Wade A Luhman and Russell J Holmes. Investigation of energy transfer in organic photovoltaic cells and impact on exciton diffusion length measurements. *Advanced Functional Materials*, 21(4):764–771, 2011.

[100] Michael Grätzel. Dye-sensitized solar cells. *Journal of photochemistry and photobiology C: Photochemistry Reviews*, 4(2):145–153, 2003.

[101] Shunsuke Tamba, Ryosuke Fujii, Atsunori Mori, Kohjiro Hara, and Nagatoshi Koumura. Synthesis and properties of seleno-analog mk-organic dye for photovoltaic cells prepared by c–h functionalization reactions of selenophene derivatives. *Chemistry letters*, 40(9):922–924, 2011.

[102] Philip G Jessop and Walter Leitner. *Chemical synthesis using supercritical fluids*. John Wiley & Sons, 2008.

[103] Rui Xiao, Seung Il Cho, Ran Liu, and Sang Bok Lee. Controlled electrochemical synthesis of conductive polymer nanotube structures. *Journal of the American Chemical Society*, 129(14):4483–4489, 2007.

[104] Adalbert Maercker. The wittig reaction. *Organic reactions*, 14:270–490, 2004.

[105] Dieter A Schlüter, Craig Hawker, and Junji Sakamoto. *Synthesis of Polymers: New Structures and Methods*. John Wiley & Sons, 2012.

[106] ABRAM Tayeb. *Matériaux moléculaires à base de systèmes pi-conjugués ou aromatiques pour l'optoélectronique (élaboration, propriétés and modélisation)*. PhD thesis, Moulay Ismail University, 2019.

[107] Yassine SADIKI AMARI. *ouveaux Matériaux Moléculaires pour des Applications en Électronique Organique. Cas des cellules solaires (BHJ et DSSC)*. PhD thesis, Moulay Ismail University, 2017.

[108] Erwin Schrödinger. Über das verhältnis der heisenberg-born-jordanschen quantenmechanik zu der meinem. *Annalen der Physik*, 384(8):734–756, 1926.

[109] Jean-Michel Combes, Pierre Duclos, and Ruedi Seiler. The born-oppenheimer approximation. In *Rigorous atomic and molecular physics*, pages 185–213. Springer, 1981.

[110] Douglas Rayne Hartree. The wave mechanics of an atom with a non-coulomb central field. part ii. some results and discussion. In *Mathematical Proceedings of the Cambridge Philosophical Society*, volume 24, pages 111–132. Cambridge University Press, 1928.

[111] John C Slater. Atomic shielding constants. *Physical Review*, 36(1):57, 1930.

[112] John C Slater. Statistical exchange-correlation in the self-consistent field. In *Advances in quantum chemistry*, volume 6, pages 1–92. Elsevier, 1972.

[113] Alexander V Neimark. The method of indeterminate lagrange multipliers in nonlocal density functional theory. *Langmuir*, 11(10):4183–4184, 1995.

[114] W Daniel Edwards and Michael C Zerner. A generalized restricted open-shell fock operator. *Theoretica chimica acta*, 72(5-6):347–361, 1987.

[115] Robert G Parr. Density functional theory of atoms and molecules. In *Horizons of quantum chemistry*, pages 5–15. Springer, 1980.

[116] Robert O Jones and Olle Gunnarsson. The density functional formalism, its applications and prospects. *Reviews of Modern Physics*, 61(3):689, 1989.

[117] Enrico Fermi. Statistical method to determine some properties of atoms. *Rend. Accad. Naz. Lincei*, 6(602-607):5, 1927.

[118] P Hohenberg and W Kohn. Density functional theory (dft). *Phys. Rev*, 136:B864, 1964.

[119] Walter Kohn and Lu Jeu Sham. Self-consistent equations including exchange and correlation effects. *Physical review*, 140(4A):A1133, 1965.

[120] Seymour H Vosko, Leslie Wilk, and Marwan Nusair. Accurate spin-dependent electron liquid correlation energies for local spin density calculations: a critical analysis. *Canadian Journal of physics*, 58(8):1200–1211, 1980.

[121] Per-Sverre Svendsen and Ulf von Barth. Gradient expansion of the exchange energy from second-order density response theory. *Physical Review B*, 54(24): 17402, 1996.

[122] Axel D Becke. Density-functional exchange-energy approximation with correct asymptotic behavior. *Physical review A*, 38(6):3098, 1988.

[123] John P Perdew and Yue Wang. Accurate and simple analytic representation of the electron-gas correlation energy. *Physical review B*, 45(23):13244, 1992.

[124] John P Perdew, Kieron Burke, and Matthias Ernzerhof. Generalized gradient approximation made simple. *Physical review letters*, 77(18):3865, 1996.

[125] JP Perdew, K Burke, and M Ernzerhof. Perdew, burke, and ernzerhof reply. *Physical Review Letters*, 80(4):891, 1998.

[126] János G Angyán, Iann C Gerber, Andreas Savin, and Julien Toulouse. van der waals forces in density functional theory: Perturbational long-range electron-interaction corrections. *Physical Review A*, 72(1):012510, 2005.

[127] Wolfgang Pauli. The connection between spin and statistics. *Physical Review*, 58 (8):716, 1940.

[128] Becke. Density-functional thermochemistry. iii. the role of exact exchange. *The Journal of Chemical Physics*, 98:5648, 1993.

[129] Frank Jensen. Polarization consistent basis sets. 4: The elements he, li, be, b, ne, na, mg, al, and ar. *The Journal of Physical Chemistry A*, 111(44):11198–11204, 2007.

[130] Errol Lewars. Computational chemistry. *Introduction to the theory and applications of molecular and quantum mechanics*, page 318, 2003.

[131] Cinzia Giannini, Massimo Ladisa, Davide Altamura, Dritan Siliqi, Teresa Sibillano, and Liberato De Caro. X-ray diffraction: a powerful technique for the multiple-length-scale structural analysis of nanomaterials. *Crystals*, 6(8):87, 2016.

[132] Qipeng Guo. *Polymer morphology: principles, characterization, and processing*. John Wiley & Sons, 2016.

[133] Andrei A Bunaciu, Elena Gabriela UdriŞTioiu, and Hassan Y Aboul-Enein. X-ray diffraction: instrumentation and applications. *Critical reviews in analytical chemistry*, 45(4):289–299, 2015.

[134] J Epp. X-ray diffraction (xrd) techniques for materials characterization. In *Materials characterization using nondestructive evaluation (NDE) methods*, pages 81–124. Elsevier, 2016.

[135] Heinz-Helmut Perkampus. *UV-VIS Spectroscopy and its Applications*. Springer Science & Business Media, 2013.

[136] Christopher Burgess. The basis for good spectrophotometric uv–visible measurements. In *UV-Visible Spectrophotometry of Water and Wastewater*, pages 1–35. Elsevier, 2017.

[137] Bhim Prasad. *Chemical Analysis and Material Characterization by Spectrophotometry*. Elsevier, 2019.

[138] Gillian McMahon. *Analytical instrumentation: a guide to laboratory, portable and miniaturized instruments*. John Wiley & Sons, 2008.

[139] AMOL Alyamani and OM Lemine. Fe-sem characterization of some nanomaterial. In *Scanning electron microscopy*. IntechOpen, 2012.

[140] Surender Kumar Sharma, Dalip Singh Verma, Latif Ullah Khan, Shalendra Kumar, and Sher Bahadar Khan. *Handbook of Materials Characterization*. Springer, 2018.

[141] NE Bengtsson and PO Risman. Dielectric properties of foods at 3 ghz as determined by a cavity perturbation technique. *Journal of Microwave Power*, 6 (2):107–123, 1971.

[142] Naoki Matsumoto, Tadasu Hosokura, Takeshi Nagashima, and Masanori Hangyo. Measurement of the dielectric constant of thin films by terahertz time-domain spectroscopic ellipsometry. *Optics letters*, 36(2):265–267, 2011.

[143] TT Grove, MF Masters, and RE Miers. Determining dielectric constants using a parallel plate capacitor. *American journal of physics*, 73(1):52–56, 2005.

[144] Yuriy Poplavko. *Electronic Materials: Principles and Applied Science*. Elsevier, 2018.

[145] A.L. Stanford and J.M. Tanner. 14 - capacitance, current, and resistance. In A.L. Stanford and J.M. Tanner, editors, *Physics for Students of Science and Engineering*, pages 394 – 423. Academic Press, 1985. ISBN 978-0-12-663380-1. doi: https://doi.org/10.1016/B978-0-12-663380-1.50017-3. URL http://www.sciencedirect.com/science/article/pii/B9780126633801500173.

[146] NA El-Ghamaz, AZ El-Sonbati, and O El-Shahat. Conducting polymers ix: Optical properties, dielectric constants and conduction mechanism of poly (n, n-bis-salphinyl 2, 6-diaminipyridine-3, 5-diamini-1, 2, 4-trizole). *Journal of Molecular Liquids*, 261:503–512, 2018.

[147] Mustafa Okutan, Yusuf Yerli, S Eren San, Faruk Yılmaz, Okan Günaydın, and Murat Durak. Dielectric properties of thiophene based conducting polymers. *Synthetic metals*, 157(8-9):368–373, 2007.

[148] V-T Truong, AR Codd, and M Forsyth. Dielectric properties of conducting polymer composites at microwave frequencies. *Journal of materials science*, 29 (16):4331–4338, 1994.

[149] Reza Taherian. 4 application of conducting composite in dielectricsã. *Electrical Conductivity in Polymer-Based Composites: Experiments, Modelling, and Applications*, page 73, 2018.

[150] Andrew K Jonscher. The 'universal'dielectric response. *nature*, 267(5613):673–679, 1977.

[151] GE Pike. Ac conductivity of scandium oxide and a new hopping model for conductivity. *Physical Review B*, 6(4):1572, 1972.

[152] AR Long. Frequency-dependent loss in amorphous semiconductors. *Advances in physics*, 31(5):553–637, 1982.

[153] SR Elliott. Ac conduction in amorphous chalcogenide and pnictide semiconductors. *Advances in physics*, 36(2):135–217, 1987.

[154] Sergio Filipe Sousa, Pedro Alexandrino Fernandes, and Maria Joao Ramos. General performance of density functionals. *The Journal of Physical Chemistry A*, 111(42):10439–10452, 2007.

[155] Axel D Becke. A new mixing of hartree–fock and local density-functional theories. *The Journal of chemical physics*, 98(2):1372–1377, 1993.

[156] MJEA Frisch, GW Trucks, H Bernhard Schlegel, Gustavo E Scuseria, Michael A Robb, James R Cheeseman, Giovanni Scalmani, Vincenzo Barone, Benedetta Mennucci, GAea Petersson, et al. gaussian 09, revision d. 01, gaussian. *Inc., Wallingford CT*, 201, 2009.

[157] Abdul-Rahman Allouche. Gabedit—a graphical user interface for computational chemistry softwares. *Journal of computational chemistry*, 32(1):174–182, 2011.

[158] Roy Dennington, Todd Keith, John Millam, et al. Gaussview, version 5. 2009.

[159] Ali Shokuhi Rad, Peiman Valipour, Atefe Gholizade, and Seyed Ehsan Mousavinezhad. Interaction of so2 and so3 on terthiophene (as a model of polythiophene gas sensor): Dft calculations. *Chemical Physics Letters*, 639:29–35, 2015.

[160] Hui-Ling Wei and Yu-Fang Liu. Theoretical investigation on electron mobility properties of anthracenedicarboximide derivatives based n-type organic semiconductors. *Journal of Physics D: Applied Physics*, 48(1):015104, 2014.

[161] Y Wang, C-Y Yam, Th Frauenheim, GH Chen, and Thomas A Niehaus. An efficient method for quantum transport simulations in the time domain. *Chemical Physics*, 391(1):69–77, 2011.

[162] O Ninis, R Kacimi, H Bouaamlat, M Abarkan, and M Bouachrine. Theoretical studies of photovoltaic properties for design of new azo-pyrrole photo-sensitizer materials as dyes in solar cells. *J. Mater. Environ. Sci*, 8:2572–2578, 2017.

[163] Monishka Rita Narayan. Dye sensitized solar cells based on natural photosensitizers. *Renewable and Sustainable Energy Reviews*, 16(1):208–215, 2012.

[164] Walid Sharmoukh, Zeinab M Hassan, Basant A Ali, Mohamed M Elnagar, Rayhan M Abdo, and Nageh K Allam. Position of the anchoring group determined the sensitization efficiency of metal-free d-π-a dyes: Combined experimental and td–dft insights. *Journal of Photochemistry and Photobiology A: Chemistry*, 367: 128–136, 2018.

[165] Ryuzi Katoh, Akihiro Furube, Toshitada Yoshihara, Kohjiro Hara, Gaku Fujihashi, Shingo Takano, Shigeo Murata, Hironori Arakawa, and M Tachiya. Efficiencies of electron injection from excited n3 dye into nanocrystalline semiconductor (zro2, tio2, zno, nb2o5, sno2, in2o3) films. *The Journal of Physical Chemistry B*, 108(15):4818–4822, 2004.

[166] John B Asbury, Yong-Qiang Wang, Encai Hao, Hirendra N Ghosh, and Tianquan Lian. Evidences of hot excited state electron injection from sensitizer molecules to tio 2 nanocrystalline thin films. *Research on Chemical Intermediates*, 27(4-5): 393–406, 2001.

[167] Ji Zhang, Han-Cheng Zhu, Rong-Lin Zhong, Li Wang, and Zhong-Min Su. Promising heterocyclic anchoring groups with superior adsorption stability and improved ipce for high-efficiency noncarboxyl dye sensitized solar cells: A theoretical study. *Organic Electronics*, 54:104–113, 2018.

[168] Wei-Lu Ding, Dong-Mei Wang, Zhi-Yuan Geng, Xiao-Ling Zhao, and Wei-Bing Xu. Density functional theory characterization and verification of high-performance indoline dyes with d–a–π–a architecture for dye-sensitized solar cells. *Dyes and pigments*, 98(1):125–135, 2013.

[169] Wichien Sang-aroon, Samarn Saekow, and Vittaya Amornkitbamrung. Density functional theory study on the electronic structure of monascus dyes as photosensitizer for dye-sensitized solar cells. *Journal of Photochemistry and Photobiology A: Chemistry*, 236:35–40, 2012.

[170] Samaneh Bagheri Novir and Seyed Majid Hashemianzadeh. Computational investigation of low band gap dyes based on 2-styryl-5-phenylazo-pyrrole for dye-sensitized solar cells. *Current Applied Physics*, 14(10):1401–1410, 2014.

[171] Cai-Rong Zhang, Zi-Jiang Liu, Yu-Hong Chen, Hong-Shan Chen, You-Zhi Wu, WangJun Feng, and Dao-Bin Wang. Dft and td-dft study on structure and properties of organic dye sensitizer ta-st-ca. *Current Applied Physics*, 10(1): 77–83, 2010.

[172] Zi-Long Zhang, Lu-Yi Zou, Ai-Min Ren, Ying-Fang Liu, Ji-Kang Feng, and Chia-Chung Sun. Theoretical studies on the electronic structures and optical properties of star-shaped triazatruxene/heterofluorene co-polymers. *Dyes and Pigments*, 96(2):349–363, 2013.

[173] Shunsuke Tamba, Ryosuke Fujii, Atsunori Mori, Kohjiro Hara, and Nagatoshi Koumura. Synthesis and properties of seleno-analog mk-organic dye for photovoltaic cells prepared by c–h functionalization reactions of selenophene derivatives. *Chemistry letters*, 40(9):922–924, 2011.

[174] Denis Jacquemin, Benedetta Mennucci, and Carlo Adamo. Excited-state calculations with td-dft: from benchmarks to simulations in complex environments. *Physical chemistry chemical physics*, 13(38):16987–16998, 2011.

[175] Dominique Guillaumont and Shinichiro Nakamura. Calculation of the absorption wavelength of dyes using time-dependent density-functional theory (td-dft). *Dyes and Pigments*, 46(2):85–92, 2000.

[176] Mannix P Balanay and Dong Hee Kim. Dft/td-dft molecular design of porphyrin analogues for use in dye-sensitized solar cells. *Physical Chemistry Chemical Physics*, 10(33):5121–5127, 2008.

[177] Tangui Le Bahers, Eric Brémond, Ilaria Ciofini, and Carlo Adamo. The nature of vertical excited states of dyes containing metals for dssc applications: insights from td-dft and density based indexes. *Physical Chemistry Chemical Physics*, 16 (28):14435–14444, 2014.

[178] Saira Sajjad, Muhammad Ali Hashmi, Tariq Mahmood, and Khurshid Ayub. Density functional theory study of structural, electronic and co adsorption properties of anionic scn-(n= 2–13) clusters. *Computational and Theoretical Chemistry*, 1163:112511, 2019.

[179] Chaofan Sun, Yuanzuo Li, Peng Song, and Fengcai Ma. An experimental and theoretical investigation of the electronic structures and photoelectrical properties of ethyl red and carminic acid for dssc application. *Materials*, 9(10):813, 2016.

[180] Ting-Ting Zhang, Jianfeng Jia, and Hai-Shun Wu. Theoretical studies of cooh group effect on the performance of rhenium (i) tricarbonyl complexes with bispyridine sulfur-rich core ligand as dyes in dssc. *Theoretical Chemistry Accounts*, 131(9):1–8, 2012.

[181] Ailing Tang, Bo Xiao, Yuming Wang, Feng Gao, Keisuke Tajima, Haijun Bin, Zhi-Guo Zhang, Yongfang Li, Zhixiang Wei, and Erjun Zhou. Simultaneously achieved high open-circuit voltage and efficient charge generation by fine-tuning charge-transfer driving force in nonfullerene polymer solar cells. *Advanced Functional Materials*, 28(6):1704507, 2018.

[182] Tapan K Ghanty and Swapan K Ghosh. A density functional approach to hardness, polarizability, and valency of molecules in chemical reactions. *The Journal of Physical Chemistry*, 100(30):12295–12298, 1996.

[183] Asit K Chandra, Tadafumi Uchimaru, Masaaki Sugie, and Akira Sekiya. Correlation between hardness and activation energies for reactions of oh radical with halomethanes. *Chemical Physics Letters*, 318(1-3):69–74, 2000.

[184] Xue-Qin Ran, Ji-Kang Feng, Ai-Min Ren, Wen-Chao Li, Lu-Yi Zou, and Chia-Chung Sun. Theoretical study on photophysical properties of ambipolar spirobifluorene derivatives as efficient blue-light-emitting materials. *The Journal of Physical Chemistry A*, 113(27):7933–7939, 2009.

[185] Hayat Sadki, Mohamed Naciri Bennani, Kamel Alimi, and MOHAMMED Bouachrine. Synthesis and characterization of new electroluminescent material based on carbazole, and terphenyle. *Int. J. Innov. Res. Sci. Eng. Tech*, 3(4): 11600–11611, 2014.

[186] N Belghiti, M Naciri Bennani, K Alimi, and MOHAMMED BOUACHRINE. Synthesis and characterization of novel copolymers based on carbazole and anthracene, for optoelectronic applications. *Journal of Advances in Chemistry Vol. 10, No. 3, 2014, ISSN 2321-807X, 2430-2440*, 2014.

[187] Bisma Ayub, Henna Wani, Shabu Shoukat, Parveez Ahmad Para, Subha Ganguly, and Mudasir Ali. Specimen preparation for electron microscopy: an overview. *Journal of Environment and Life Sciences*, 2(3):85–88, 2017.

[188] AJ Heeger. Conducting polymers for carbon electronics themed issue. *Chemical Society Reviews*, 39(7), 2010.

[189] Hua Gong, Jian Xiang, Ligeng Xu, Xuejiao Song, Ziliang Dong, Rui Peng, and Zhuang Liu. Stimulation of immune systems by conjugated polymers and their potential as an alternative vaccine adjuvant. *Nanoscale*, 7(45):19282–19292, 2015.

[190] MM El-Nahass, AA Atta, MA Kamel, and SY Huthaily. Ac conductivity and dielectric characterization of synthesized pn, n dimethylaminobenzylidene-malononitrile (dbm) organic dye. *Vacuum*, 91:14–19, 2013.

[191] Khalil Jumah Tawfiq Hamam. *Organic Solar Cells Based on High Dielectric Constant Materials: An Approach to Increase Efficiency*. PhD thesis, Western Michigan University, 2013.

[192] OE Sherif. Dft calculations, electrical and thermal properties of unsubstituted triphenylformazan. *Int. J. Electrochem. Sci*, 10:9751–9765, 2015.

[193] Gregory M Treich, Shamima Nasreen, Arun Mannodi Kanakkithodi, Rui Ma, Mattewos Tefferi, James Flynn, Yang Cao, Rampi Ramprasad, and Gregory A Sotzing. Optimization of organotin polymers for dielectric applications. *ACS applied materials & interfaces*, 8(33):21270–21277, 2016.

[194] M Pollak and To H Geballe. Low-frequency conductivity due to hopping processes in silicon. *Physical Review*, 122(6):1742, 1961.

[195] SR Elliott. Temperature dependence of ac conductivity of chalcogenide glasses. *Philosophical magazine B*, 37(5):553–560, 1978.

[196] HM Zeyada, FM El-Taweel, MM El-Nahass, and MM El-Shabaan. Effect of substitution group on dielectric properties of 4h-pyrano [3, 2-c] quinoline derivatives thin films. *Chinese Physics B*, 25(7):077701, 2016.

[197] S Selvakumar, R Murugaraj, E Viswanathan, S Sankar, and K Sivaji. Dielectric properties and relaxation mechanism of organic trans-stilbene and p-terphenyl molecular crystals using impedance spectroscopy. *Journal of Molecular Structure*, 1056:152–156, 2014.

[198] Hussam Bouaamlat, Nasr Hadi, Najat Belghiti, Hayat Sadki, Mohammed Naciri Bennani, Farid Abdi, Taj-dine Lamcharfi, Mohammed Bouachrine, and Mustapha Abarkan. Dielectric properties, ac conductivity, and electric modulus analysis of bulk ethylcarbazole-terphenyl. *Advances in Materials Science and Engineering*, 2020, 2020.

[199] C Joseph Mathai, S Saravanan, MR Anantharaman, S Venkitachalam, and S Jayalekshmi. Characterization of low dielectric constant polyaniline thin film synthesized by ac plasma polymerization technique. *Journal of Physics D: Applied Physics*, 35(3):240, 2002.